N O T I C E

THIS DOCUMENT HAS BEEN REPRODUCED FROM MICROFICHE. ALTHOUGH IT IS RECOGNIZED THAT CERTAIN PORTIONS ARE ILLEGIBLE, IT IS BEING RELEASED IN THE INTEREST OF MAKING AVAILABLE AS MUCH INFORMATION AS POSSIBLE

OSU

The Ohio State University

SIMULATION OF THE ENHANCED TRAFFIC ALERT AND COLLISION AVOIDANCE SYSTEM (TCAS II)

Roberto G. Rojas
Walter D. Burnside
Philip Law
Brett Grandchamp

The Ohio State University

ElectroScience Laboratory

Department of Electrical Engineering
Columbus, Ohio   43212

30272-101

REPORT DOCUMENTATION PAGE	1. REPORT NO.	2.	3. Recipient's Accession No.

4. Title and Subtitle
SIMULATION OF THE ENHANCED TRAFFIC
ALERT AND COLLISION AVOIDANCE SYSTEM (TCAS II)

5. Report Date
September 1985

6.

7. Author(s)
Roberto G. Rojas, Walter D. Burnside, Philip Law, Brett Grandchamp

8. Performing Organization Rept. No.
716199-3

9. Performing Organization Name and Address
The Ohio State University
ElectroScience Laboratoyr
1320 Kinnear Road
Columbus, Ohio 43212

10. Project/Task/Work Unit No.

11. Contract(C) or Grant(G) No.
(C) NSG 1498
(G)

12. Sponsoring Organization Name and Address
National Aeronautics and Space Administration
Langley Research Center
Hampton, VA 23665

13. Type of Report & Period Covered

14.

15. Supplementary Notes

16. Abstract (Limit: 200 words)

The OSU aircraft code is used to analyze and simulate the TCAS II circular array which is mounted on the fuselage of a Boeing 737 aircraft. It is shown that the sum and difference patterns radiated by the circular array are distorted by the various structures of the aircraft, i.e., wings, tail, etc. Furthermore, monopulse curves are calculated and plotted for several beam positions and THETA angles. As expected, the worst cases of distortion occur when the beams are pointed toward the tail of the aircraft.

17. Document Analysis   a. Descriptors

b. Identifiers/Open-Ended Terms

c. COSATI Field/Group

18. Availability Statement	19. Security Class (This Report)	21. No. of Pages
	Unclassified	78
	20. Security Class (This Page)	22. Price
	Unclassified	

(See ANSI–Z39.18)　　　　See Instructions on Reverse

OPTIONAL FORM 272 (4–77)
(Formerly NTIS–35)
Department of Commerce

PRECEDING PAGE BLANK NOT FILMED

TABLE OF CONTENTS

LIST OF TABLES

LIST OF FIGURES

FIGURE

SIMULATION OF THE ENHANCED TRAFFIC ALERT
AND COLLISION AVOIDANCE SYSTEM
(TCAS II)

I. INTRODUCTION

The Bendix Communications Division, under contract with the Federal
Aviation Administration, has developed an airborne collision avoidance
system which consists of a top and bottom mounted eight-element,
electronically-scanned circular array [1,2]. This system, which is
referred to as the Enhanced TCAS II, can continually search the space
surrounding the protected aircraft providing a nearly complete spherical
coverage. The array radiates sum and difference beams at 1030 MHz. The
same beams are also used to receive the 1090 MHz replies from
surrounding aircraft. The receiver consists of a monopulse angle
measurement which provides target bearing estimates, and it is required
to have one to two-degree precision [1,2]. The bearing estimates are
combined with altitude and slant range information to generate an
accurate 3-D target position and velocity estimate.

Ideally, the shape of the sum and difference beams would not change
as they are scanned around the aircraft. However, the fuselage, wings
and tail of the aircraft will distort the antenna patterns, and
therefore, they will affect the accuracy of the monopulse reciever.
Thus, it is very important to analyze the effect of the fuselage, wings
and tail on the radiation patterns (sum and difference) of the circular

1

array. The OSU aircraft code [3], which is based on the Uniform Geometrical Theory of Diffraction (UTD) [4,5,6], is ideal to carry out this analysis because it can model various types of aircraft, and it is also capable of calculating both the near and far field patterns of antennas mounted on the fuselage.

II. OSU AIRCRAFT CODE

The OSU aircraft code [3], is a Fortran 77 program based on the UTD which is a high-frequency analysis technique [4,5,6]. This code has been developed at OSU to investigate the radiation patterns of antennas mounted on an aircraft fuselage which is modeled by a composite ellipsoid [3,7]; whereas, the wings, stabilizers, nose, fuel tanks, engines, etc., are simulated as perfectly conducting flat plates that can be attached to the fuselage and/or to each other. Note that the composite ellipsoid fuselage model is necessary to successfully model the wide variety of real world fuselage shapes. The fuselage has a dominant effect on the resulting radiation pattern because the antenna is assumed to be mounted on it; therefore, it must be simulated accurately, especially near the antenna. Up to 25 flat plates may be included in the computer model of the aircraft, and each plate can have up to six corners. The maximum number of antennas it can handle is ten which is simply based on present array dimensions. The program can model narrow slots or monopoles which are less than $\lambda/4$ long and are normal to the fuselage surface. Note that the number of plates and antennas is limited only by the size of the computer memory.

The limitations associated with the computer code are due to the nature of the analysis which is based on the UTD. As stated before, UTD is a high frequency method, and in terms of the scattering from plates this means that each plate should have edges at least a wavelength long. In terms of the composite ellipsoid structure, the length of the major and minor radii should be at least one wavelength. More details about the program and the theory can be found in [3,7].

III. TCAS II SYSTEM

The TCAS II array consists of an eight-element, 10.5 inch diameter, electronically-steerable circular array as shown in Figure 1 (Note: For the convenience of the reader, all figures have been grouped together at the end of the report). Each element is a top loaded monopole with a microstrip matching network located at the base of each monopole [1,2]. A Butler matrix is used to produce the sum and difference beam patterns as shown in Figure 2. The input to the matrix are the mode excitations, while the output are the element excitations. The Butler matrix operates in such a manner that, given the mode excitations (M_ℓ), the element excitations (E_i) are given by [8]

$$E_i = \frac{1}{\sqrt{N}} \sum_{\ell=-N/2+1}^{N/2} (MA_\ell) \exp [j(MP_\ell)+j2\pi i\ell/N] \tag{1}$$

where

E_i = complex excitation of the ith element (volts)

M_ℓ = complex excitation of the ℓth mode (volts)

N = number of elements = number of mode inputs
(in this case N=8)

3

MA_ℓ = amplitude of the ℓth mode input (volts)

MP_ℓ = phase of the ℓth mode input (radians)

The elements are numbered counterclockwise when looking down onto the array as depicted in Figure 3.

To steer the beam radiated by the circular array in the counterclockwise direction by an angle of $\Delta\beta$ radians, a negative phase gradient is applied across the mode inputs. The gradient $\Delta\theta_\ell$ applied to the ℓth mode is given by [8]

$$\Delta\theta_\ell - \ell\Delta\beta \qquad\qquad (2)$$

where ℓ is the mode number. In the TCAS II system, six-bit phase shifters are used which permit beam steering in 5.625 degree steps. In other words, the beams can be steered to any one of 64 equally spaced positions. More details of this matrix feed method can be found in [1,2,8].

Ideally, as mentioned in the introduction, the sum and difference beams will not change as they are electronically steered around the aircraft. An ideal pair of sum and difference beams are depicted in Figure 4 where the effects of the wings and tail of the aircraft are not included. When the wings and tail are added to the computer model of the aircraft, the radiation patterns will be distorted as shown in Figure 5. This distortion will affect the accuracy of the bearing estimate of the target aircraft. Thus, it is crucial to analyze the effect of the aircraft structures on the antenna patterns in order to

4

compensate for this distortion and still obtain bearing estimates within the accuracy requirements.

IV. SIMULATION

The OSU aircraft code was used to analyze the radiation patterns of the circular array (TCAS II) mounted on the fuselage of a Boeing 737 aircraft. The fuselage of the aircraft was modeled by a composite ellipsoid; whereas, the wings and tail were modeled by flat plates. Calculations were made with and without the plates to study the effect of the tail and wings on the radiation patterns.

In order to calculate the sum and difference beams, the following approach was followed: First, the radiation patterns of each of the eight monopoles were calculated and stored. Each monopole was assigned a weight of one, and it was assumed to be radiating in the presence of the other seven unexcited monopoles. From measurements made at Bendix, it was determined that the radiation pattern of a single monopole radiating in the presence of the other elements of the array can be modeled by a pair of monopoles separated by $\lambda/4$ and out of phase by ninety degrees as shown in Figure 6. The phase center of the pair of monopoles corresponding to the radiation direction $\beta=0$ (see Figure 6) is given by

$$x_p = (1-B/A)/(1+B/A) \cdot \lambda/8 \qquad (3)$$

where A and B are the weights of the outer and inner monopoles, respectively. Since this phase center has to coincide with the position of the actual monopole in the circular array, the computer model used to

5

simulate the circular array is depicted in Figure 7. It can be shown
that the front-to-back ratio of the pair of monopoles shown in Figure 6
is given by

$$FB(dB) = 20 \log_{10} [(A+B)/(A-B)] \qquad . \qquad (4)$$

Equation (4) can be rewritten as a function of FB, namely,

$$B/A = (10^{FB/20}-1)/(10^{FB/20}+1) \qquad . \qquad (5)$$

Thus, for a given FB, the ratio of B over A can be obtained from
Equation (5). For the circular array considered in this report, FB was
assumed to be 15 dB. It follows from (5) that

$$B/A = 0.698 \qquad . \qquad (6)$$

The values assigned to A and B in the simulation of the TCAS II system
were the following:

$$A = 1. \qquad ; \qquad B = 0.698 \qquad . \qquad (7)$$

Before the element patterns are shown, it is necessary to briefly
define the coordinate system used to define the pattern coordinates.
The pattern axis of rotation [3] is defined by the spherical angles
(THC,PHC) as illustrated in Figure 8. These angles define a radial
vector direction which points in the direction of the pattern axis of
rotation. These angles actually set-up a new coordinate system in
relation to the reference coordinates. Once this new coordinate system
is defined, the program will then compute any conical pattern cut in

6

which THETA is used as the conical pattern angle about the Z_p-axis. The principal plane patterns are the roll, elevation, and azimuth plane cuts as depicted in Figure 9.

Azimuth radiation patterns (THETA=75°) of each of the eight elements of the circular array are shown in Figures 10 through 17. First, these patterns were calculated by simulating the aircraft by only a fuselage, in which case they represent the ideal radiation patterns. The computer model of the fuselage is shown in Figure 18. Next, the same patterns were calculated, but a more realistic model of the aircraft was used as illustrated in Figure 19. Note that this model includes the wings and tail of the aircraft; however, the horizontal stabilizers were not included. It is known from experience, that for the location of the array being considered here, the horizontal stabilizers will have an insignificant effect on the radiation pattern, and therefore, they are not included in the computer model to save computer time. It is observed (for THETA=75°) that the elements most affected by the different structures of the aircraft are elements three, four, and five. Especially element number four, because its main beam is directed toward the tail. The input data used to calculate the element patterns is shown in Table I. Note that this data includes the plates that model the wings and tail of the aircraft. The input data used to calculate the ideal element patterns does not include any plates. Once the radiation patterns of the eight elements are calculated and stored, they can be combined by weighing each pattern appropriately to obtain the sum and difference beams pointed in any of the 64 equally spaced directions around the aircraft.

7

TABLE I

INPUT DATA FOR TCAS II
AIRCRAFT CODE: ELLIPSOID VERSION

UN:INCHES
3
FQ: 1.06 GHZ
1,1.06,1.
FG: BOEING 737
77.,74.,830.,308.56
T
0.,0.,70.
SG: ELEMENT 1
2.64,66.464
2
1.39,-45.
0.,0.,0.,2.78,3
1.,-45.
1.39,135.
0.,0.,0.,2.78,3
.698,45.
FG: RIGHT WING
4,T
1.,75.,67.952
1.,536.93,316.14
1.,536.93,379.86
1.,75.,240.26
FG: LEFT WING
4,T
1.,-75.,240.26
1.,-536.93,379.86
1.,-536.93,316.14
1.,-75.,67.952
FG: TAIL
4,T
77.,8.25,618.55
284.147,8.25,819.056
284.147,0.,683.696
77.,0.,483.19
FG: TAIL
4,T
77.,0.,483.19
284.147,0.,683.696
284.147,-8.25,819.056
77.,-8.25,618.55

BO:
T
PP: POLAR PLOT IN DB
F
1,1.5,3
PD: AZIMUTH PLANE
90.,0.,90.
0,360,1
T,1000000.
EX:
SG: ELEMENT 2
3.73,70.
2
1.39,0.
0.,0.,0.,2.78,3
1.,-45.
1.39,180.
0.,0.,0.,2.78,3
.698,45.
EX:
SG: ELEMENT 3
2.64,73.536
2
1.39,45.
0.,0.,0.,2.78,3
1.,-45.
1.39,225.
0.,0.,0.,2.78,3
.698,45.
EX:
SG: ELEMENT 4
0.,75.
2
1.39,90.
0.,0.,0.,2.78,3
1.,-45.
1.39,270.
0.,0.,0.,2.78,3
.698,45.

EX:
SG: ELEMENT 5
-2.64,73.536
2
1.39,135.
0.,0.,0.,2.78,3
1.,-45.
1.39,-45.
0.,0.,0.,2.78,3
.698,45.
EX:
SG: ELEMENT 6
-3.73,70.
2
1.39,180.
0.,0.,0.,2.78,3
1.,-45.
1.39,0.
0.,0.,0.,2.78,3
.698,45.
EX:
SG: ELEMENT 7
-2.64,66.464
2
1.39,225.
0.,0.,0.,2.78,3
1.,-45.
1.39,45.
0.,0.,0.,2.78,3
.698,45.
EX:
SG: ELEMENT 8
0.,65.
2
1.39,270.
0.,0.,0.,2.78,3
1.,-45.
1.39,90.
0.,0.,0.,2.78,3
.698,45.

The complex mode excitations (M_ℓ) of the Butler matrix were provided by Bendix, and they are given in Table II. These modes correspond to the case where the beams point in the direction of the nose of the aircraft. Once the modes M_ℓ are given, the element excitations (E_i) are easily calculated as indicated by Equation (1), and the results are shown in Table III. The details of how the modes (M_ℓ) were obtained are given in [8,9], and they will not be discussed here. Using the element excitations obtained in Table III, the sum and difference beams are computed. The azimuth radiation patterns (THETA=90°) of the sum and difference beams are depicted in Figure 20 where the aircraft is modeled by a fuselage only; i.e., an aircraft model without plates. If a more realistic model of the aircraft is used, i.e., an aircraft model with plates, one obtains the patterns shown in Figure 21 where the effect of the wings and tail are clearly illustrated. As expected, the vertical stabilizer produces the greatest distortion on the radiation patterns. The wings also distort the patterns; however, that distortion is less severe than that due to the vertical stabilizer. When the beams are steered ninety degrees, the effect on the radiation patterns due to the wing being illuminated is more apparent as depicted in Figure 22. The worst case occurs when the beams are pointed toward the tail of the aircraft as shown in Figure 23. Recall that the beams are steered by simply adding a phase gradient to the mode excitations as indicated in Equation (2).

9

TABLE II

MODE EXCITATION COEFFICIENTS

Sum Beam

MODE NO.	AMPLITUDE (DB)	PHASE (DEG)	COMPLEX	
-3	-16.3732	-99.94	(-0.0262	, -0.1495)
-2	-13.3899	-19.899	(0.2013	, -0.07285)
-1	-6.51216	46.14	(0.3274	, 0.3407)
0	-3.81708	3	(0.6435	, 0.03372)
1	-6.41237	45.163	(0.3370	, 0.3389)
2	-13.3899	-20.545	(0.2004	, -0.07512)
3	-16.3732	-99.671	(-0.02550	, -0.1497)
4	-59.9001	0	(1.012×10^{-3},	0.0)

Difference Beam

MODE NO.	AMPLITUDE (DB)	PHASE (DEG)	COMPLEX	
-3	-13.5801	76.06	(0.05045	, 0.2032)
-2	-11.8875	151.101	(-0.2228	, 0.1230)
-1	-3.30896	-142.86	(-0.5446	,-0.4125)
0	-19.836	4	(0.1017	, 7.109×10^{-3})
1	-5.40549	39.163	(0.4161	, 0.3389)
2	-9.79482	-24.545	(0.2945	,-0.1345)
3	-15.8675	-105.67	(-0.04347	,-0.1549)
4	-59.9	0	(1.012×10^{-3},	0.0)

TABLE III

ELEMENT EXCITATION COEFFICIENTS

Sum Beam

ELEMENT NO.	AMPLITUDE (DB)	PHASE (DEG)	COMPLEX	
1	-6.34062	32.3742	(0.4070	, 0.2580)
2	-19.22	37.8493	(0.08638	, 0.06712)
3	-12.6118	-78.1094	(0.04824	, -0.2291)
4	-12.6953	-48.9456	(0.1523	, -0.1748)
5	-12.4011	-78.2374	(0.04890	, -0.2348)
6	-19.6004	35.5149	(0.08523	, 0.06083)
7	-6.42343	32.0745	(0.4045	, 0.2535)
8	-4.54845	9.18114	(0.5848	, 0.09451)

Difference Beam

ELEMENT NO.	AMPLITUDE (DB)	PHASE (DEG)	COMPLEX	
1	-8.61776	90.9364	(-6.059×10^{-3}	, 0.3707)
2	-5.39759	135.167	(-0.3809	, 0.3787)
3	-17.2476	150.721	(-0.1197	, 0.06714)
4	-19.6467	4.03708	(0.1039	, 7.332×10^{-3})
5	-11.7454	-.270649	(0.2587	, -1.222×10^{-3})
6	-5.30513	-42.3221	(0.4014	, -0.3656)
7	-7.3956	-88.7265	(9.486×10^{-3}	, -0.4267)
8	-33.6091	-30.3929	(0.01800	, -0.0106)

The next step in the analysis is to process the information given by the sum and difference beams to obtain an estimate of the bearing of the target aircraft. This is done with a Squinted Beam Monopulse Processor [1,2]. The output of the angle processor is a monopulse characteristic curve given by [1,2]

$$M = 20 \log_{10} \left| \frac{\Sigma + j \Delta}{\Sigma - j \Delta} \right| \tag{8}$$

where Σ and Δ are the sum and difference beams, respectively. As indicated in [1,2], this processor is optimum in the sense that the standard deviation of the estimated bearing is minimized for a given transponder reply signal-to-noise ratio. In Figure 24, the monopulse curves corresponding to Figures 20 and 21 are shown. Both curves are similar, except in the regions from -180 to -80 degrees and from 80 to 180 degrees where the effect of the wings can be seen. Since the region of interest is from -25 to 25 degrees, the same monopulse curves are plotted again in Figure 25. As expected, both monopulse curves have the same shape, except that the curve corresponding to the aircraft model with plates is shifted upward about 3 dBs. This shift occurs because the beams are directed toward the nose of the aircraft. In other words, the tail and wings are not strongly illuminated and therefore they have a minor influence on the radiation patterns. On the other hand, when the beams are steered toward the wings and tail, the monopulse curves are distorted as shown in Figures 26 through 29. In Figure 27, in the region from 0 to 25 degrees, the monopulse curve is distorted due to the scattering of the right wing. A more severe distortion of the monopulse curve occurs when the beams are pointed toward the tail as illustrated in Figures 28 and 29.

12

In order to have a better understanding of the effect of the vertical stabilizer, a more detailed analysis was done. In Figure 30, it is shown that for THETA greater than about 70 degrees, the vertical stabilizer will shadow the circular array when the observation point is behind the tail of the aircraft. In other words, for THETA greater than 70 degrees and when the observation point is behind the tail, the direct field radiated by the array will be blocked by the vertical stabilizer. This blockage of the direct field will cause a distortion in the sum and difference beams when they are pointed toward the tail.

Recall that the total field radiated by the circular array is calculated by superposing the source, reflected and diffracted fields plus higher order terms if necessary. For example, consider the case when the beams are pointed in the direction -157 degrees as illustrated in Figure 31 where only the source field is included. Since THETA=60°, the tail will not block the direct field and therefore, this field component is continuous. Note that all the patterns shown up to this point were the E_θ component of the electric field. However, since the array is mounted on a convex surface, i.e., prolate spheroid, the E_ϕ component of the electric field will also be excited due to the presence of surface ray tension [7,10] as shown in Figure 32. Even though the E_ϕ component is excited, it is much smaller than the E_θ, and it can be neglected in the present problem. Because the vertical stabilizer is illuminated by the circular array, it will reflect some energy as shown in Figure 33. Recall that the vertical stabilizer is modeled by two flat plates which form a wedge as shown in Figure 19. Since both

13

faces of the wedge are illuminated, energy is reflected in two directions as shown in Figure 33. When both field components are added (source and reflected), one obtains the patterns shown in Figure 34. These field patterns, which are referred to as the geometrical optics fields (GO), are somewhat distorted due to the presence of the reflected field. Furthermore, they are discontinuous due to the absence of the edge diffracted field. The edge diffracted field is shown in Figure 35, and as expected, its magnitude is comparable to that of the reflected field. When the diffracted field is added to the GO field, the sum and difference beams become continuous as shown in Figure 36. Even though the resulting sum and difference beams are somewhat distorted, they are still fairly similar to the ideal patterns depicted in Figure 31. Next, using Equation (8), one computes the monopulse characteristic curves as shown in Figure 37. The effect of the vertical stabilizer can be seen around the region from -30 to 0 degrees and from 50 to 80 degrees. As mentioned before, the region of interest is from -25 to 25 degrees. Thus, in Figure 38, only this region is plotted where one can see in more detail the effect of the tail. It is clear that the effect of the tail is severe from -25 to -7 degrees. On the other hand, in the region from -5 to 20 degrees, the two monopulse curves are similar except for a shift of about 3 dBs down in the curve corresponding to the aircraft model that includes the vertical stabilizer. Note that in Figure 38, the tail is located around 23 degrees; however, the effect of the tail on the monopulse curve shows up from -25 to -7 degrees. The reason for this apparent discrepancy is that, as stated before, the vertical

14

stabilizer is like a wedge-type structure. Therefore, energy is reflected in two directions. The distortion seen in Figure 38 is due to the left size of the vertical stabilizer when looking at the aircraft from behind. As THETA increases, the effect of the tail becomes more severe as illustrated in Figures 39 through 45.

When THETA is equal to 90°, which corresponds to the azimuth plane, the vertical stabilizer will block the direct field from the array as illustrated in Figure 46 where the source fields corresponding to the sum and difference beams are depicted. When the reflected and edge diffracted fields are added to the source field, one obtains the patterns shown in Figure 47. Using Equation (8), the monopulse characteristic curves are obtained as depicted in Figures 48 and 49. In Figure 49, the severe distortion caused by the vertical stabilizer in the region from 2 to 25 degrees can be seen. One additional example is shown in Figures 50 through 54 where THETA = 95°. For this conical angle (THETA = 95°), the source field depicted in Figure 50 is composed mostly of surface ray fields diffracted from the fuselage of the aircraft which is a convex surface. The monopulse curve for this conical angle is depicted in Figures 53 and 54 where the effect of the vertical stabilizer can be seen around 22 degrees.

As illustrated by the several examples, monopulse curves are a function of the angle THETA, i.e., the monopulse curves change as THETA changes. In order to have some idea of how they are affected by THETA, the following calculations were made. First, for a fix beam position, monopulse curves were calculated for nine different values of THETA: 60°, 65°, 70°, 75°, 80°, 85°, 90°, 95°, and 100°. Once the nine

15

monopulse curves are obtained for each beam position, the average of these nine curves can be calculated for angles of observation within ±25 degrees off boresight. Furthermore, for the same range of angles, the maximum and minimum values attained by the monopulse curves can also be calculated. The average values of the monopulse curves for various beam positions are shown in Figures 55 through 59. For a given value of THETA within the range 60 to 100 degrees, the monopulse curve will lie within the envelope form by the curves labeled maximum and minimum as illustrated in Figures 55 through 59. Note that for the beam positions 0, 90 and 145 degrees, the maximum and minimum curves are close together. On the other hand, for the beam positions 180 and -157, both curves (maximum and minimum) are farther apart. Recall that in an ideal situation, the monopulse curves would not change as the value of THETA changes. However, as shown in Figures 55 through 59, the problem being considered here is not ideal. Therefore, it is important to study to what extent the monopulse curves depart from the ideal situation in order to take appropriate measures and compensate for any distortion.

V. CONCLUSIONS

The OSU aircraft code was used to study the radiation patterns of the TCAS II system. Ideally, the shape of the sum and difference beams radiated by the circular array will not change as they are rotated around the aircraft. However, as shown in this report, due to the blockage by the various structures of the aircraft, i.e., fuselage,

16

wings, vertical stabilizer, the shape of the beams will be distorted.
As expected, the distortion was shown to be worst when the beams are
pointed in the vicinity of the tail of the aircraft. Another aspect
that was studied was the variation of the monopulse curves as a function
of the angle THETA which is the conical angle measured from the
vertical. An example was considered when the beams are pointed toward
the vicinity of the tail of the aircraft. It was shown that due to the
blockage of the vertical stabilizer, the monopulse curves are severely
distorted for THETA greater than 70 degrees and when the observation
point is behind the tail.

As stated several times before, the distortion of the sum and
difference beams will affect the accuracy of the estimated bearing of
the target aircraft. Thus, appropriate measures have to be taken to
compensate for the distortion of the radiation patterns of the TCAS II
circular array. For example, once the monopulse curves are computed for
the 64 beam positions (every 5.625 degrees) following the approach
described in Section IV, a lookup table can be created to compensate for
the differences between the curves. This compensation is necessary in
order to maintain the one to two-degree precision of the monopulse
receiver.

17

REFERENCES

[1] A.I. Sinsky, J.E. Reed and J. Fee, "Enhanced TCAS II Tracking Accuracy", AIAA/IEEE 6th Digital Avionics Systems Conference, Baltimore, Maryland, December 3-6, 1984.

[2] J. Emory Reed, "Enhanced TCAS II Antenna Characteristic Report", Report No. BCD-TR-090, The Bendix Corporation, Communications Divison; prepared under Contract No. DTFA01-82-C-10019 for the U.S. Department of Transportation, FAA, October 25, 1983.

[3] W.D. Burnside, J.J. Kim, B. Grandchamp, R.G. Rojas and P. Law, "Airborne Antenna Radiation Pattern Code User's Manual", Report No. 716199-4, February 1985, The Ohio State University ElectroScience Laboratory, Dept. of Electrical Engineering, Columbus, Ohio 43212; prepared under Contract No. NSG-1498 for the National Aeronautics and Space Administration, Langley Research Center.

[4] J.B. Keller, "A Geometrical Theory of Diffraction", in Calculus of Variations and Its Applications, L.M. Graves, Ed., New York, McGraw-Hill, pp. 27-25, 1958.

[5] R.G. Kouyoumjian, P.H. Pathak, and W.D. Burnside, "A Uniform GTD for the Diffraction by Edges, Vertices, and Convex Surfaces", in Theoretical Methods for Determining the Interaction of Electromagnetic Waves with Structures, J.K. Skwirzynski, ed., Netherlands, Sijthoff and Noordhoff, 1981.

[6] R.G. Kouyoumjian and P.H. Pathak, "A Uniform Geometrical Theory of Diffraction for an Edge in a Perfectly Conducting Surface", Proc. IEEE, Vol. 62, pp. 1448-1461, November 1974.

[7] Jacob J. Kim, "Simulation and Analysis of Airborne Antenna Radiation Patterns", Technical Report 716199-1, The Ohio State University ElectroScience Laboratory, Dept. of Electrical Engineering; prepared under Contract No. N00019-81-C-0424 for the Department of the Navy, Naval Air Systems Command, December 1984.

[8] Allen I. Sinsky, "Circular Array Design Equations", Special Technical Report 119, Advanced Development Group, Bendix Communications Division, January 1985.

[9] B. Sheley, "A Matrix-Fed Circular Array for Continuous Scanning", Proc. of the IEEE, pp. 2016-2027, November 1968.

[10] P. Pathak, N.N. Wang, "An Analysis of the Mutual Coupling Between Antennas on a Smooth Convex Surface," Final Report 784583-7, The Ohio State University ElectroScience Laboratory, Department of Electrical Engineering, Columbus, Ohio 43212; prepared under Contract No. N62269-76-C-0554 for the Naval Air Development Center, Warminster, Pennsylvania, October 1978.
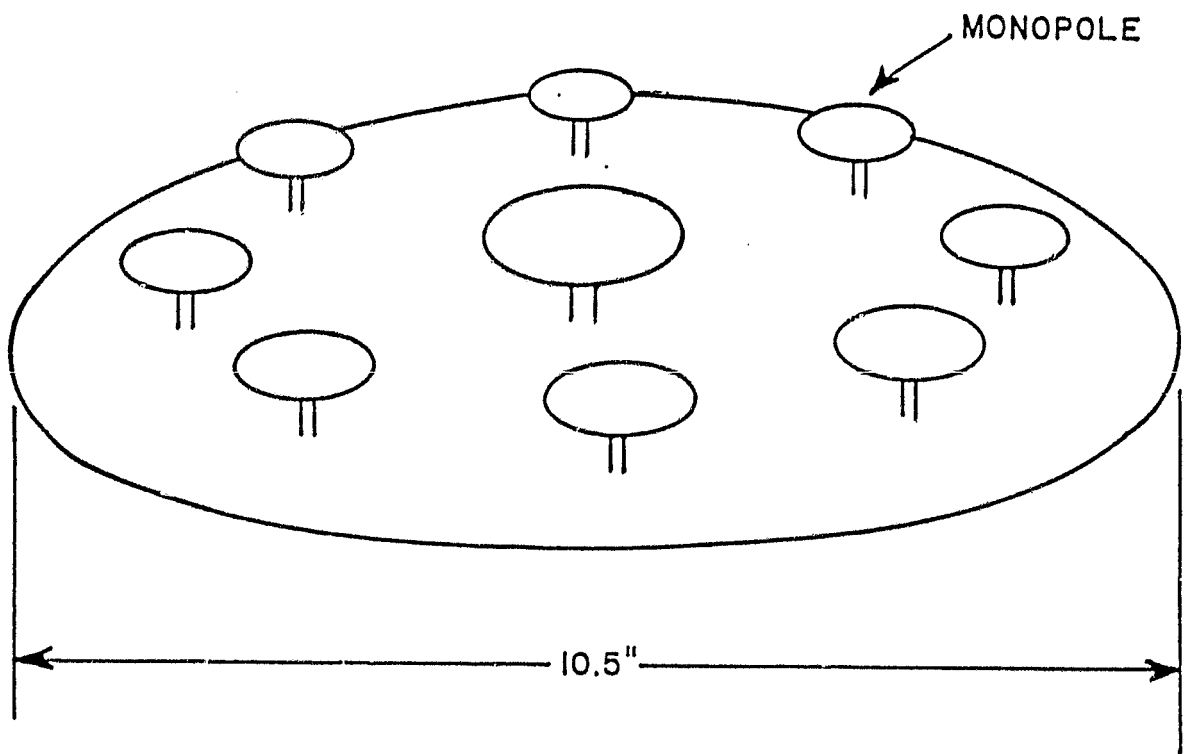
MONOPOLE

— 10.5" —

Figure 1. Eight element, 10.5-inch diameter, electronically-steerable
circular array. The array is covered by a fiberglass radome
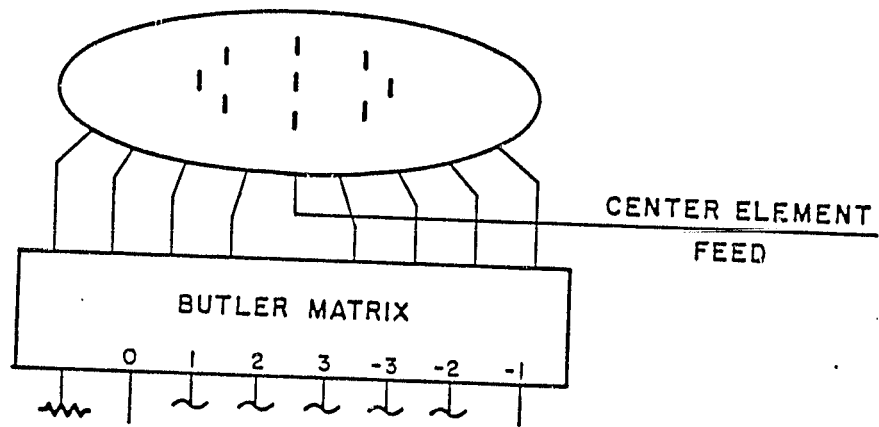and rain erosion coating not shown in this figure.

19

Figure 2. Beam forming network which uses a Butler matrix to determine the element excitations.
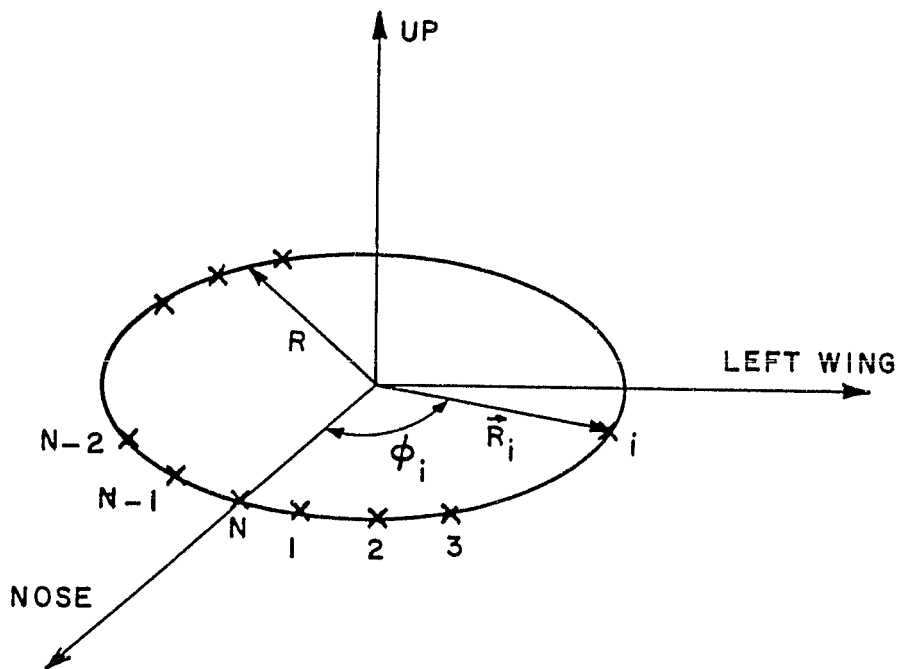
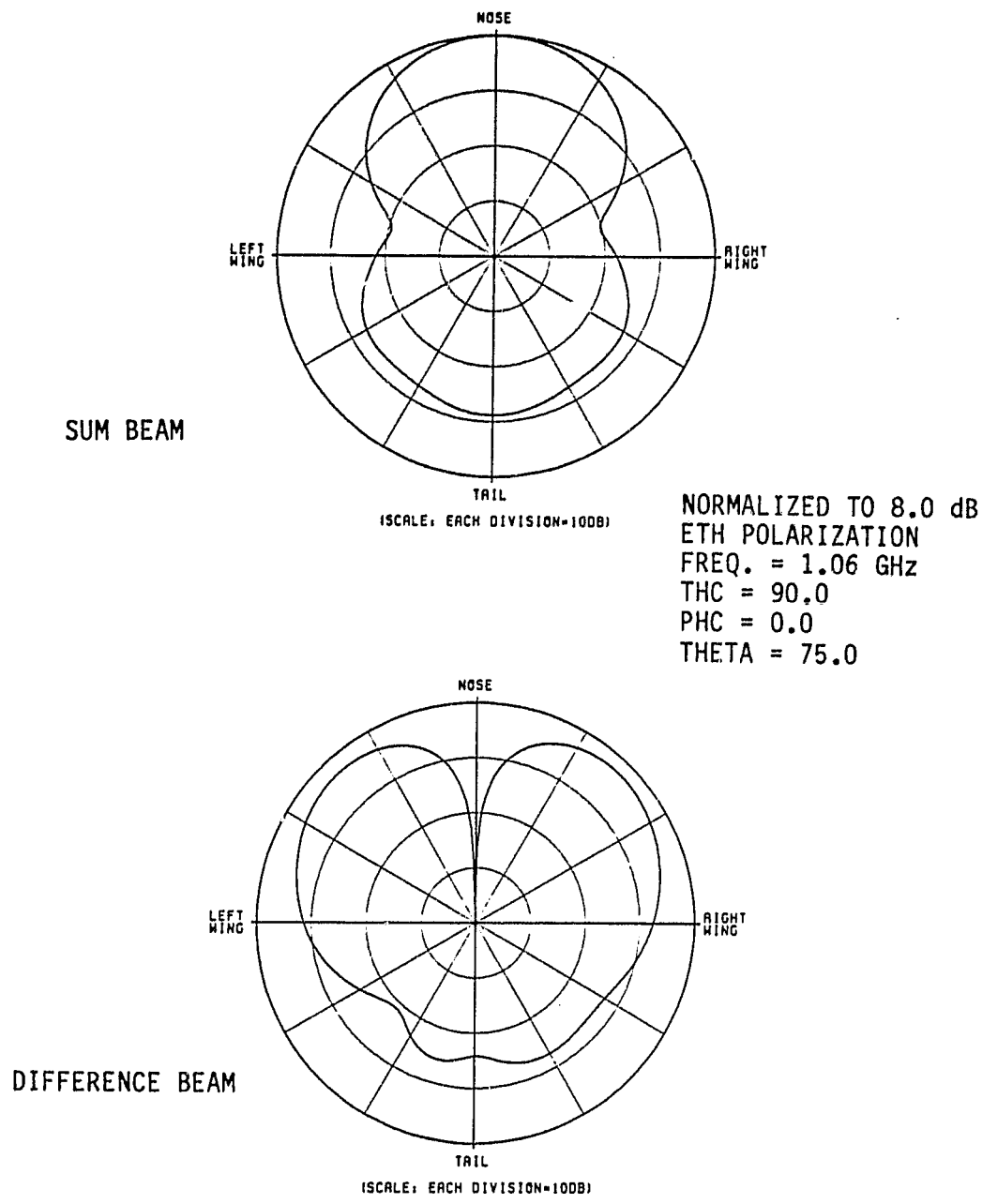Figure 3. Convention used to number the elements of the circular array.

SUM BEAM

NOSE

LEFT WING

RIGHT WING

TAIL

(SCALE: EACH DIVISION=10DB)

NORMALIZED TO 8.0 dB
ETH POLARIZATION
FREQ. = 1.06 GHz
THC = 90.0
PHC = 0.0
THETA = 75.0

DIFFERENCE BEAM

NOSE

LEFT WING

RIGHT WING

TAIL

(SCALE: EACH DIVISION=10DB)

Figure 4.   Sum and difference beams pointed in the nose direction.   The
aircraft is modeled by a fuselage only.

22
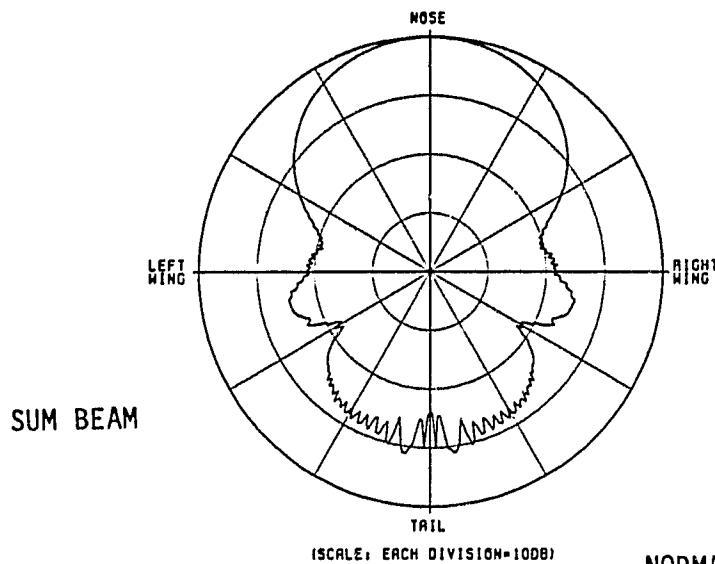
SUM BEAM

(SCALE: EACH DIVISION=10DB)

NORMALIZED TO 8.0 dB
ETH POLARIZATION
FREQ. = 1.06 GHz
THC = 90.0
PHC = 0.0
THETA = 75.0
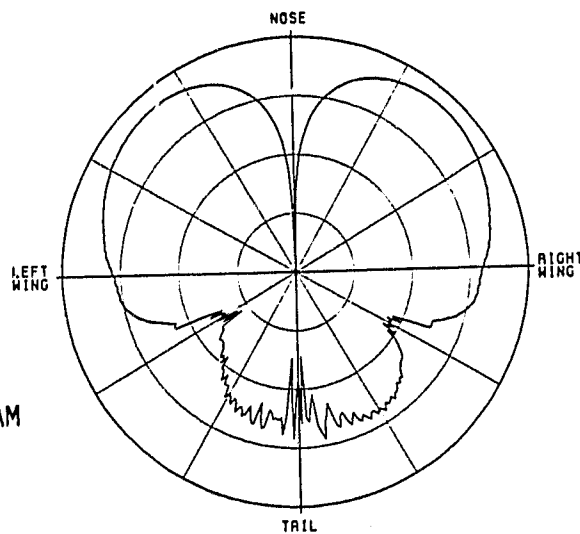
DIFFERENCE BEAM

(SCALE: EACH DIVISION=10DB)

Figure 5. Sum and difference beams pointed in the nose direction. The computer aircraft model includes the wings and tail.
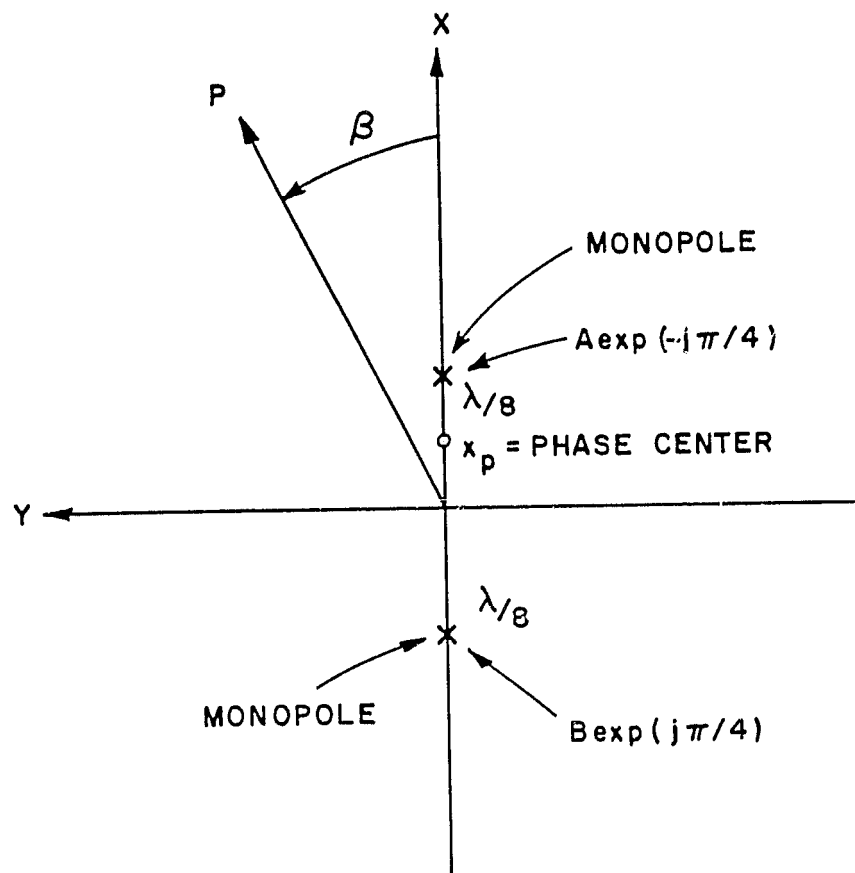
Figure 6. Geometry of monopole pair.

NOSE

TOP VIEW

FREQUENCY = 1.06 GHz

8

1

7

3.61"   6.39"

LEFT
WING   2   6   RIGHT
                                     WING

3

5

4   MONOPOLES

TAIL

SIDE VIEW
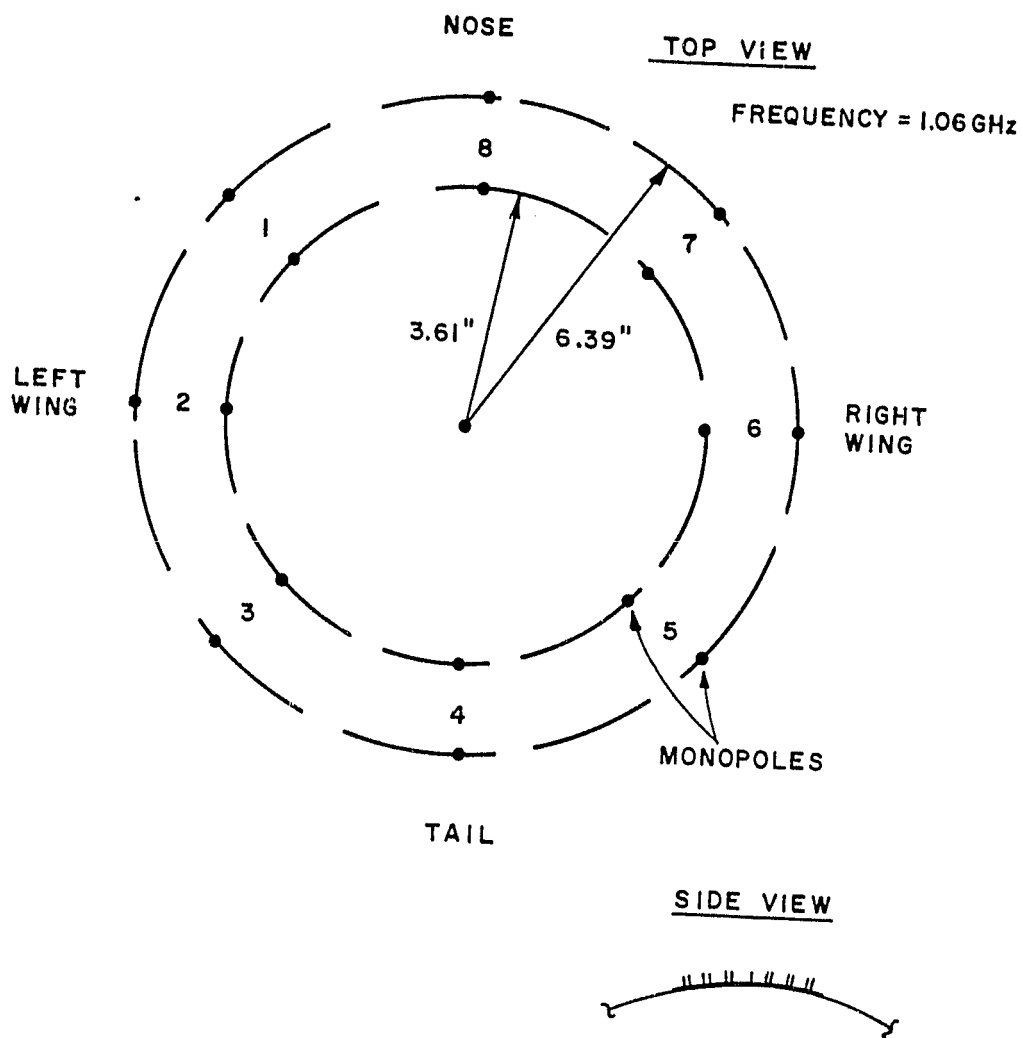
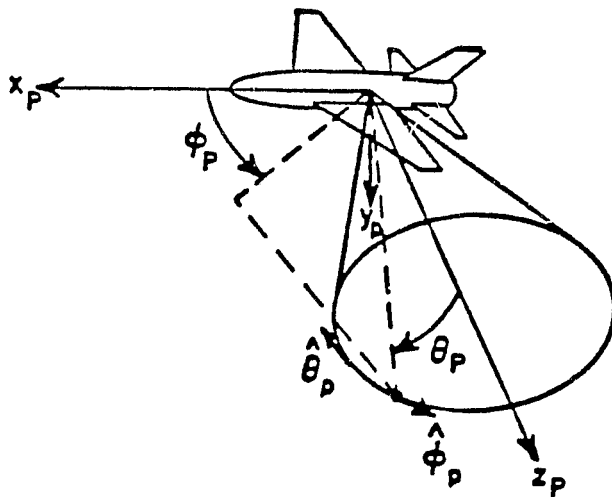Figure 7. Geometry of the computer model that was used to simulate the circular array.
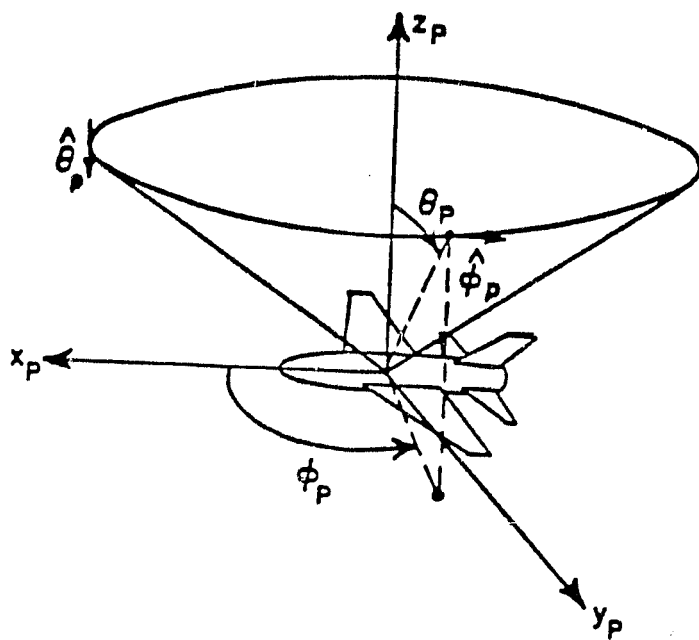
25
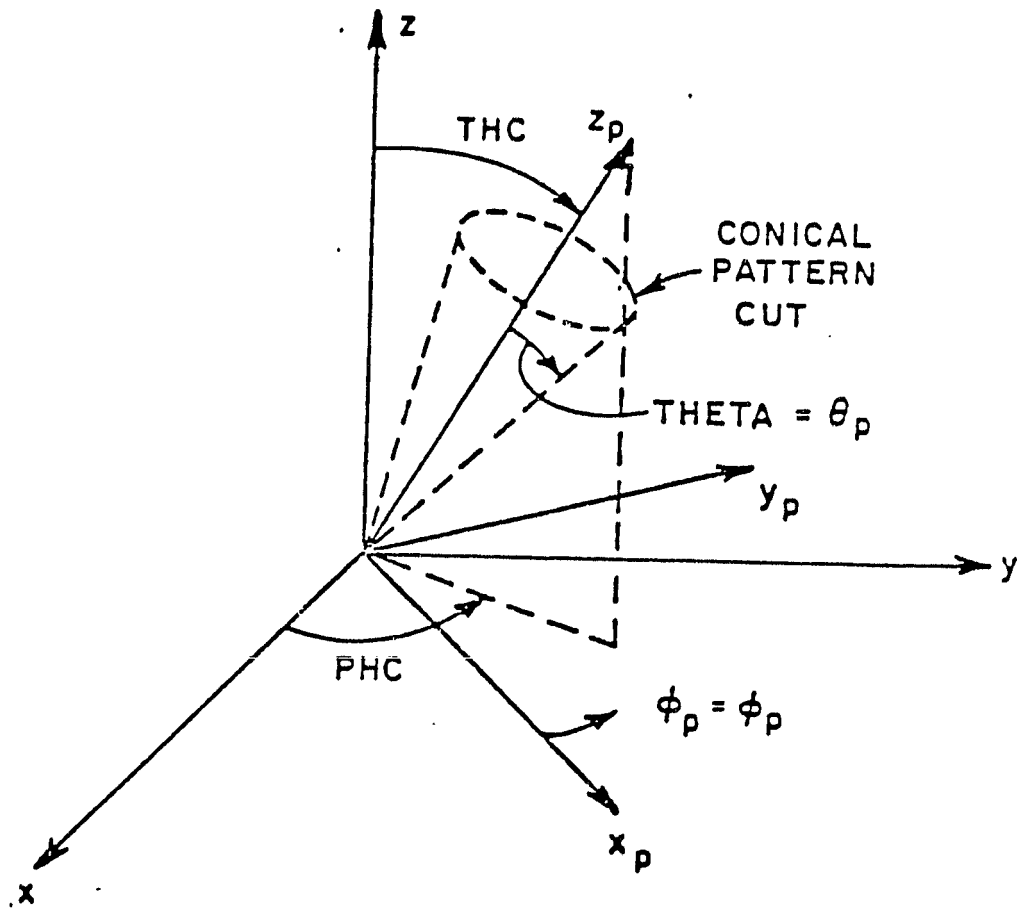
Figure 8. Definition of pattern axis.
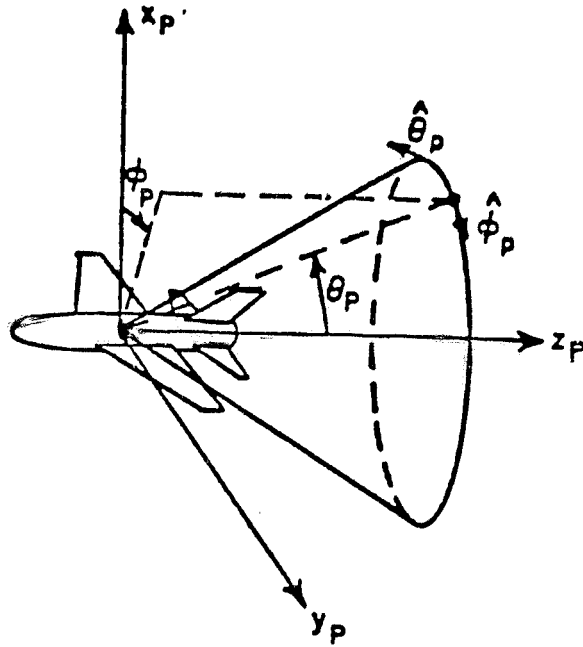
(a) ROLL PLANE COORDINATES (THC = 0°, PHC = 0°)

(b) ELEVATION PLANE COORDINATES (THC = 90°, PHC = 90°)

Figure 9. Transformed coordinate systems for the conical pattern cuts.

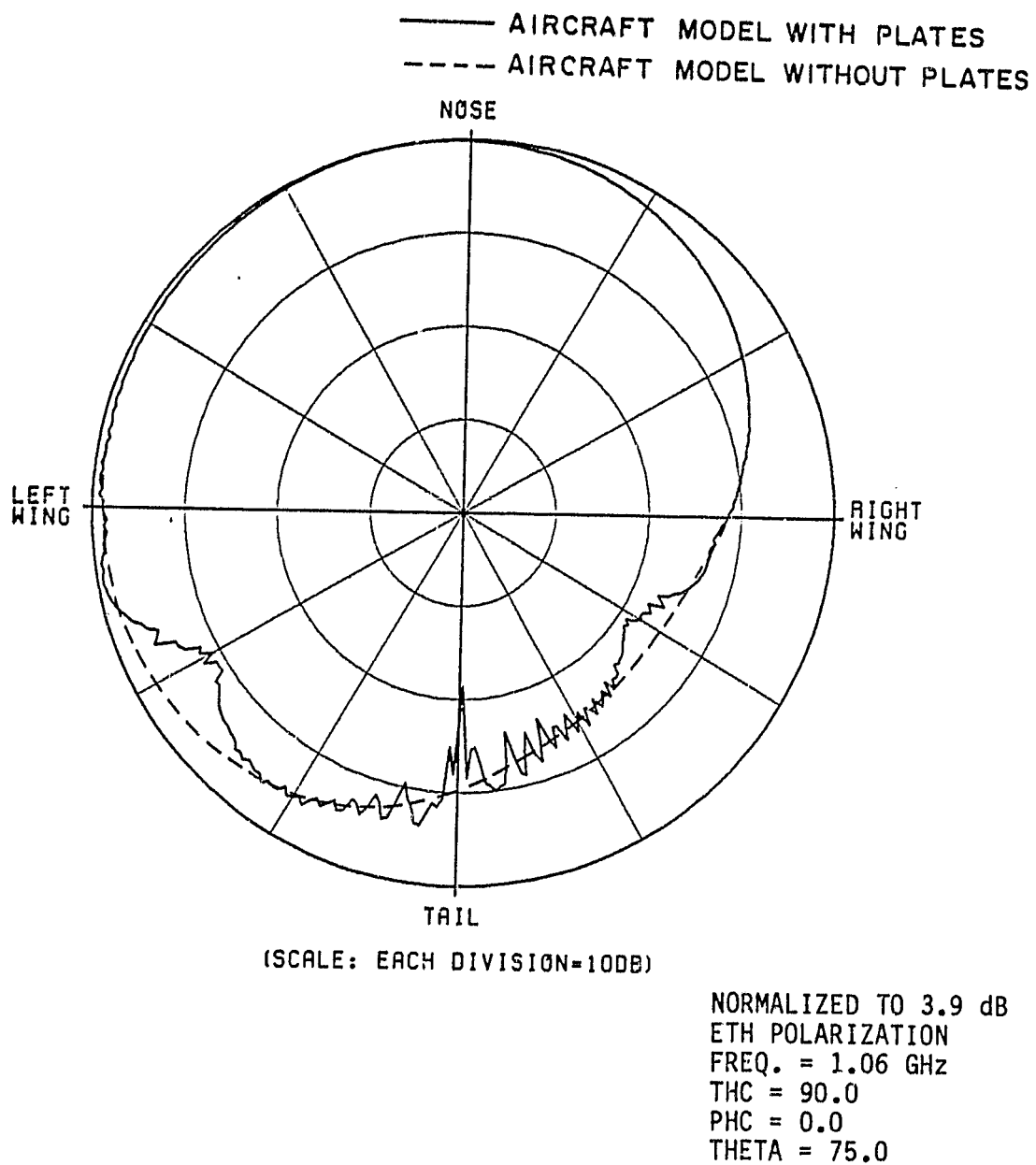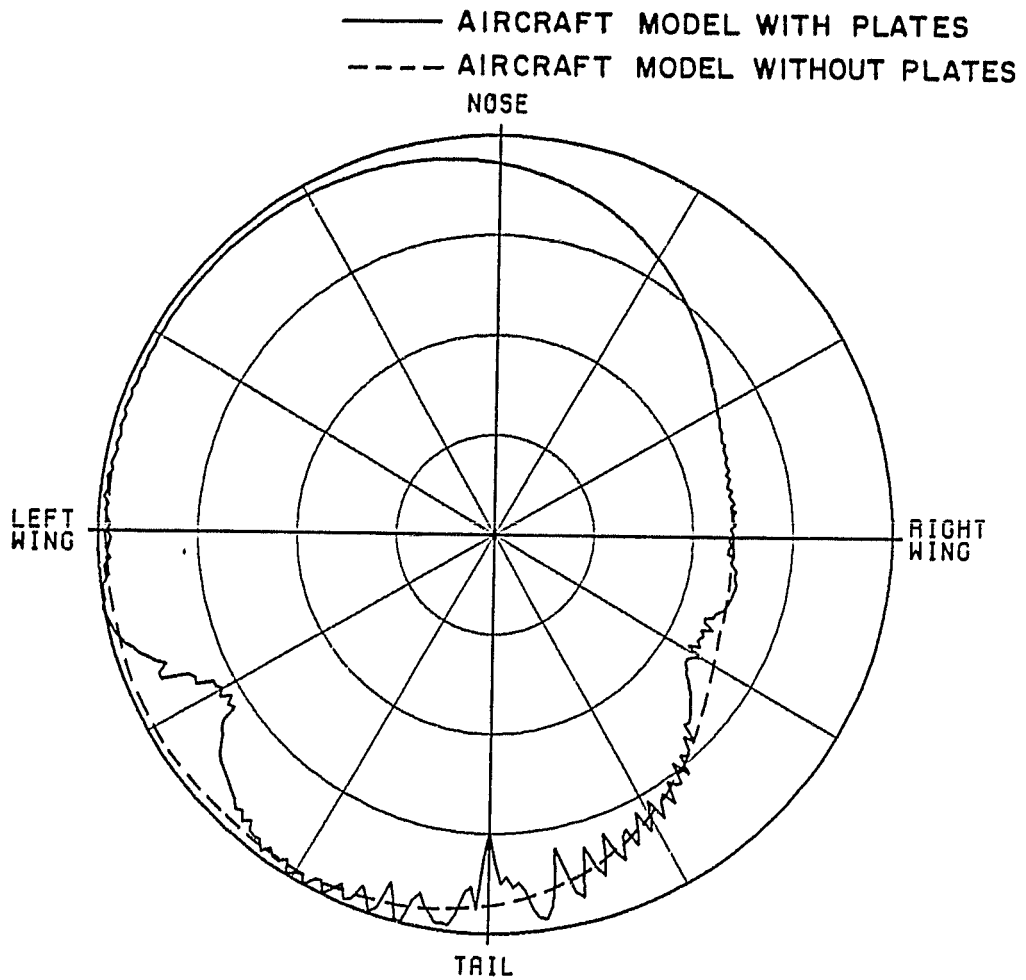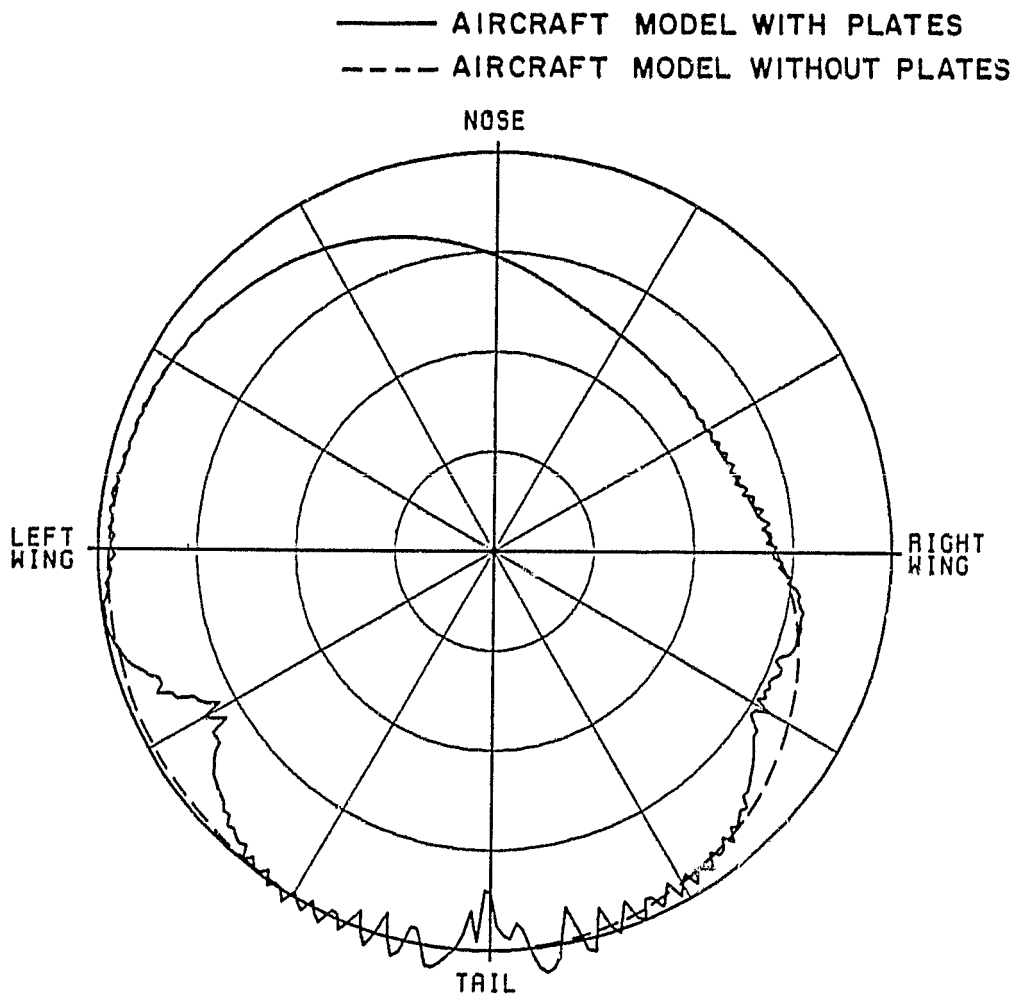(c) AZIMUTH PLANE COORDINATES (THC = 90°, PHC = 0°)

Figure 9. (continued).

——— AIRCRAFT MODEL WITH PLATES

– – – – AIRCRAFT MODEL WITHOUT PLATES

NOSE

LEFT WING

RIGHT WING

TAIL

(SCALE: EACH DIVISION=10DB)

NORMALIZED TO 3.9 dB
ETH POLARIZATION
FREQ. = 1.06 GHz
THC = 90.0
PHC = 0.0
THETA = 75.0

Figure 10. Radiation pattern of element number one (see Figure 7).

29

——— AIRCRAFT MODEL WITH PLATES

– – – – AIRCRAFT MODEL WITHOUT PLATES

NOSE

LEFT
WING

RIGHT
WING

TAIL

(SCALE: EACH DIVISION=10DB)

NORMALIZED TO 3.9 dB
ETH POLARIZATION
FREQ. = 1.06 GHz
THC = 90.0
PHC = 0.0
THETA = 75.0

Figure 11. Radiation pattern of element number two (see Figure 7).
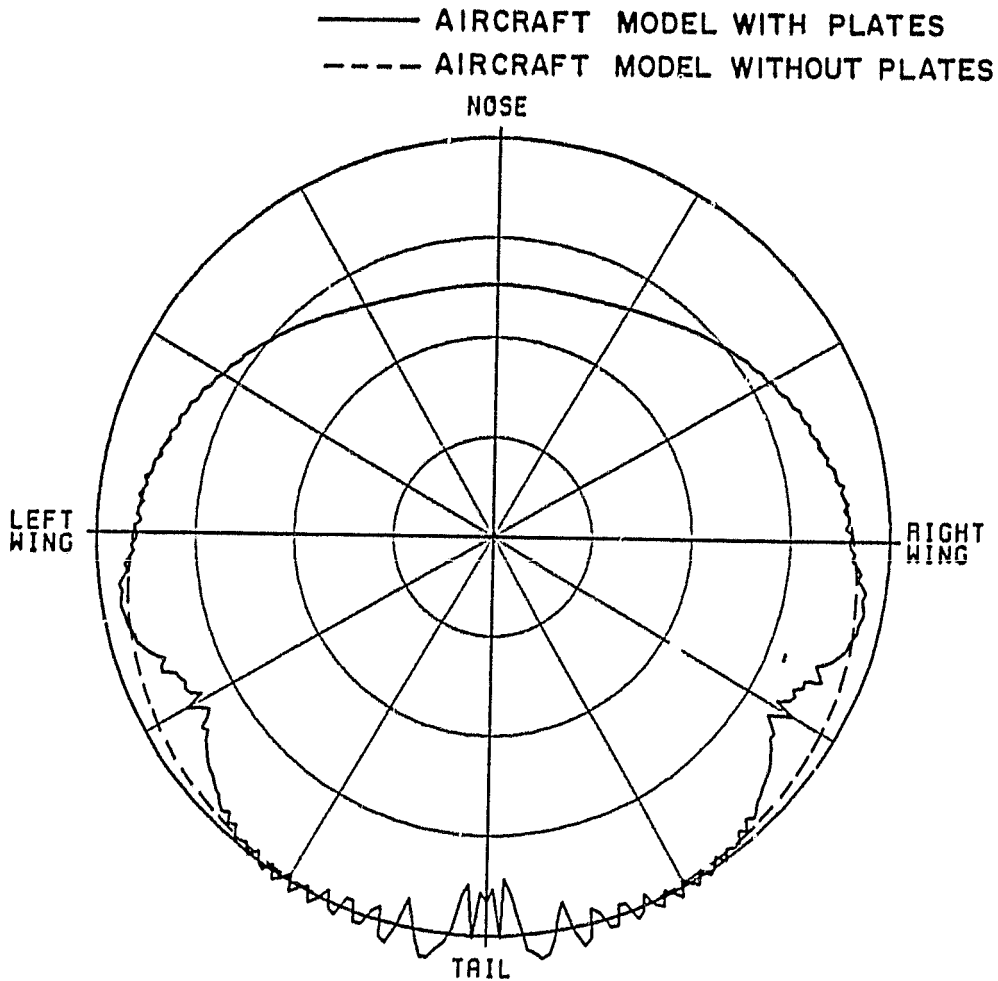
30

AIRCRAFT MODEL WITH PLATES

---- AIRCRAFT MODEL WITHOUT PLATES

NOSE

LEFT
WING

RIGHT
WING

TAIL

(SCALE: EACH DIVISION=10DB)

NORMALIZED TO 3.9 dB
ETH POLARIZATION
FREQ. = 1.06 GHz
THC = 90.0
PHC = 0.0
THETA = 75.0

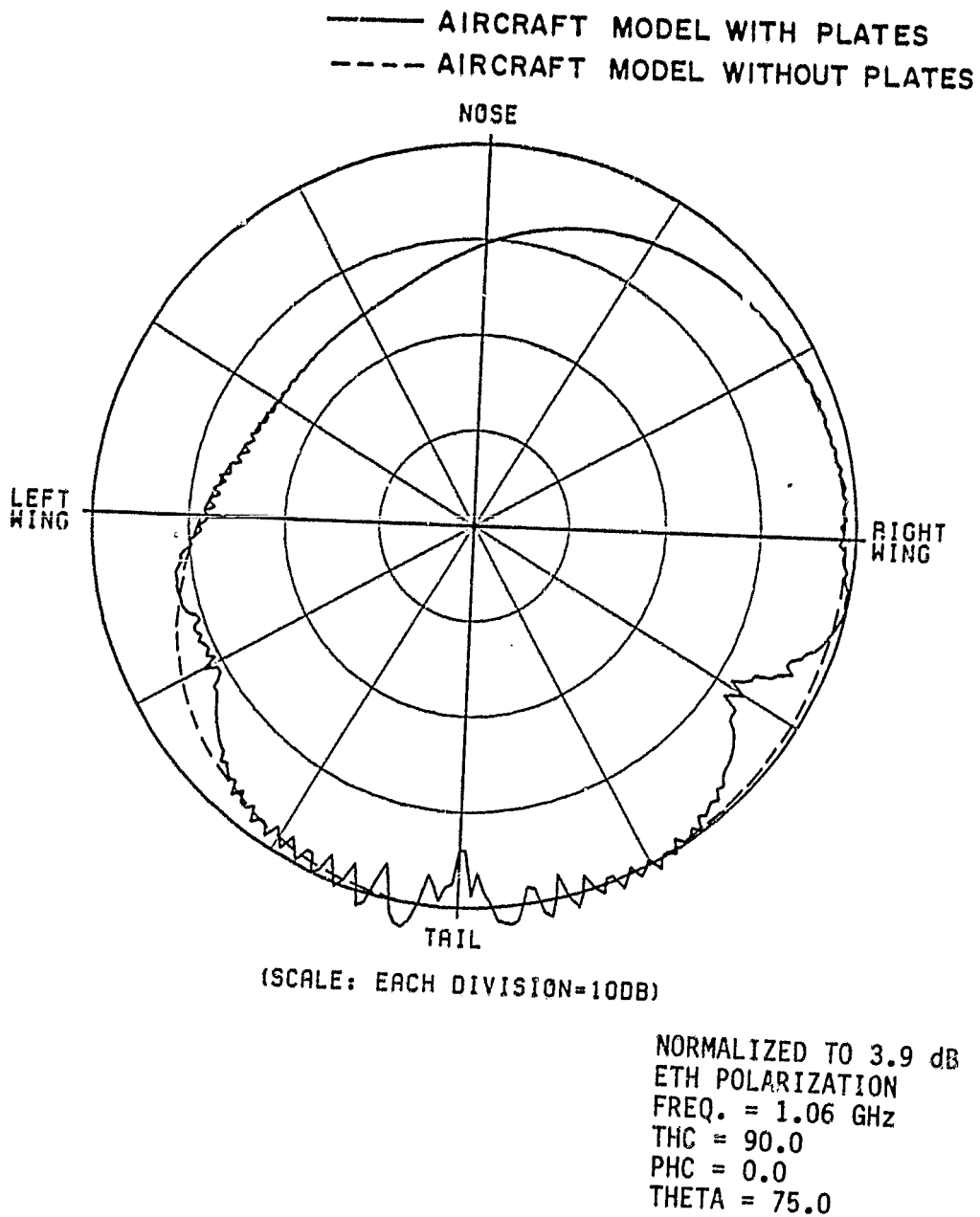Figure 12. Radiation pattern of element number four (see Figure 7).

31

AIRCRAFT MODEL WITH PLATES
- - - - AIRCRAFT MODEL WITHOUT PLATES

NOSE

LEFT
WING

RIGHT
WING

TAIL

(SCALE: EACH DIVISION=10DB)

NORMALIZED TO 3.9 dB
ETH POLARIZATION
FREQ. = 1.06 GHz
THC = 90.0
PHC = 0.0
THETA = 75.0

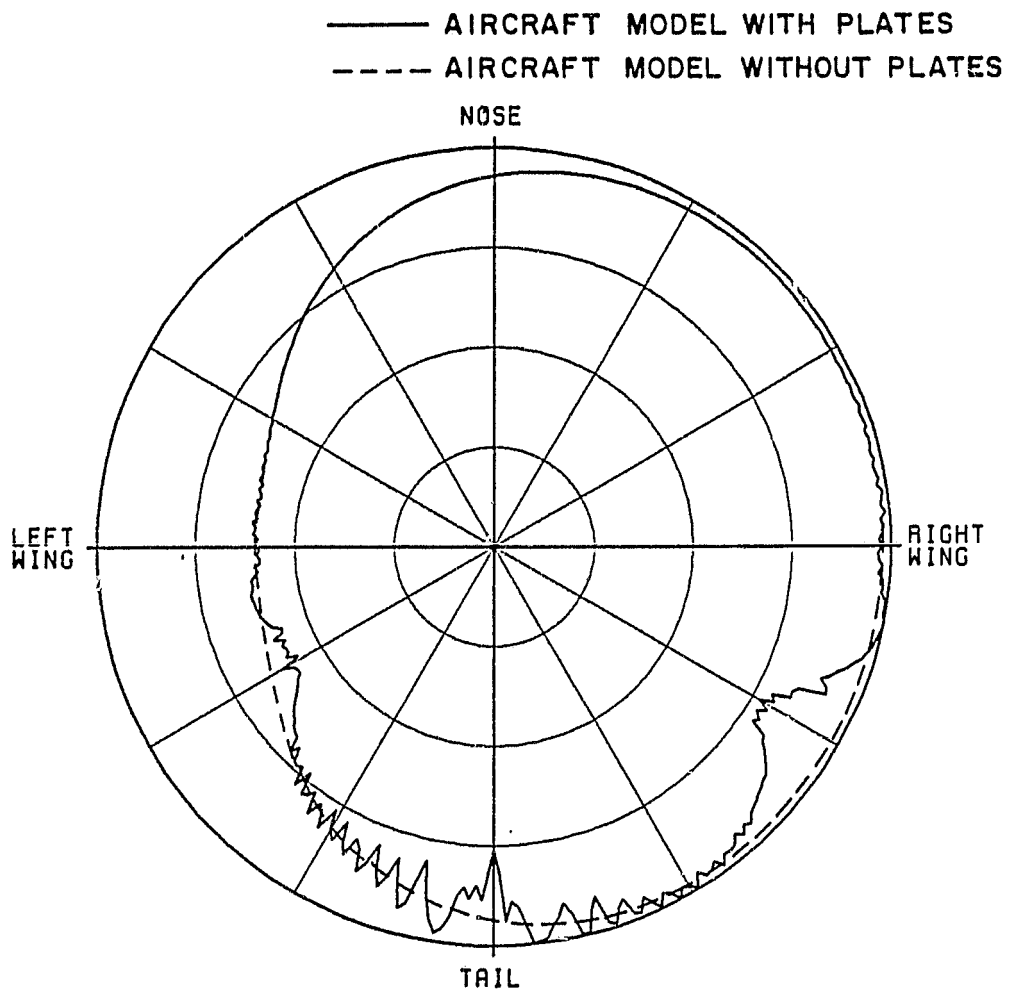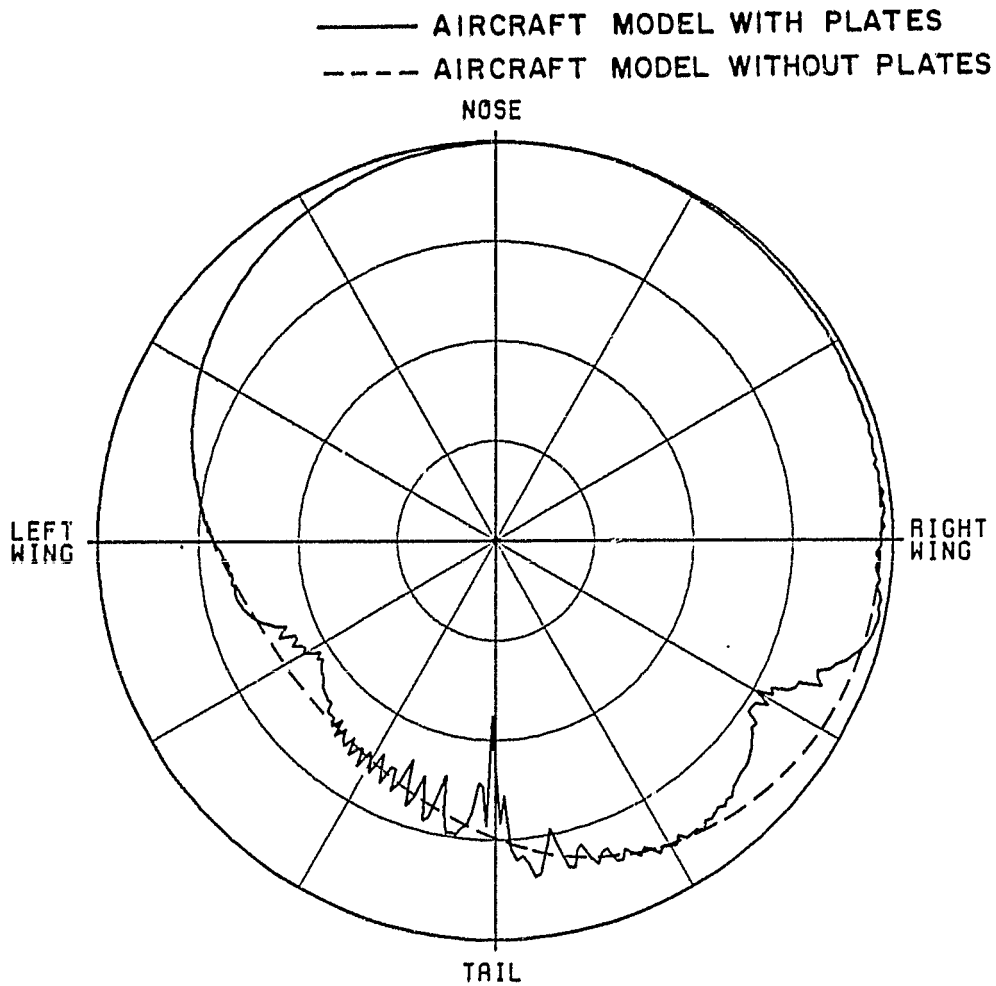Figure 13. Radiation pattern of element number four (see Figure 7).

32

——— AIRCRAFT MODEL WITH PLATES
———— AIRCRAFT MODEL WITHOUT PLATES

NOSE

LEFT
WING

RIGHT
WING

TAIL

(SCALE: EACH DIVISION=10DB)

NORMALIZED TO 3.9 dB
ETH POLARIZATION
FREQ. = 1.06 GHz
THC = 90.0
PHC = 0.0
THETA = 75.0

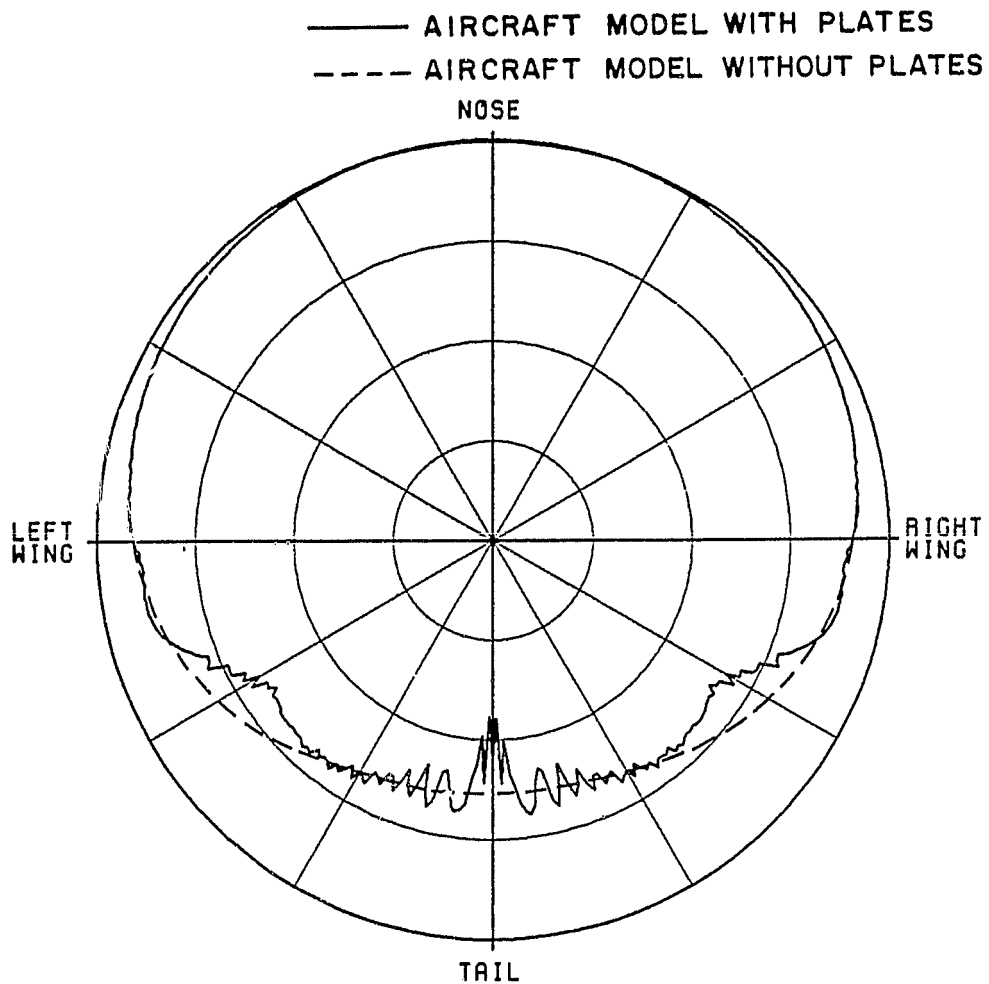Figure 14. Radiation pattern of element number five (see Figure 7).

33

―――――― AIRCRAFT MODEL WITH PLATES

―――― AIRCRAFT MODEL WITHOUT PLATES

NOSE

LEFT
WING

RIGHT
WING

TAIL

(SCALE: EACH DIVISION=1GDB)

NORMALIZED TO 3.9 dB
ETH POLARIZATION
FREQ. = 1.06 GHz
THC = 90.0
PHC = 0.0
THETA = 75.0

Figure 15. Radiation pattern of element number six (see Figure 7).

34

AIRCRAFT MODEL WITH PLATES
AIRCRAFT MODEL WITHOUT PLATES

NOSE

LEFT WING

RIGHT WING

TAIL

(SCALE: EACH DIVISION=10DB)

NORMALIZED TO 3.9 dB
ETH POLARIZATION
FREQ. = 1.06 GHz
THC = 90.0
PHC = 0.0
THETA = 75.0

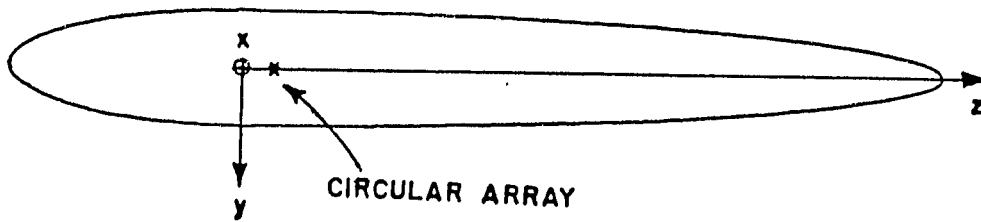Figure 16. Radiation pattern of element number seven (see Figure 7).

—— AIRCRAFT MODEL WITH PLATES

———— AIRCRAFT MODEL WITHOUT PLATES

(SCALE: EACH DIVISION=10DB)

NORMALIZED TO 3.9 dB
ETH POLARIZATION
FREQ. = 1.06 GHz
THC = 90.0
PHC = 0.0
THETA = 75.0

Figure 17. Radiation pattern of element number eight (see Figure 7).

36
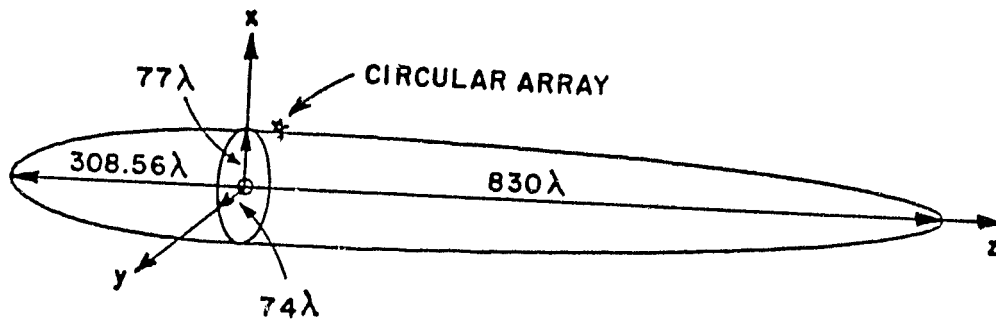
(a) SIDE VIEW

(b) TOP VIEW

Figure 18. Computer model of the fuselage of the Boeing 737 aircraft.
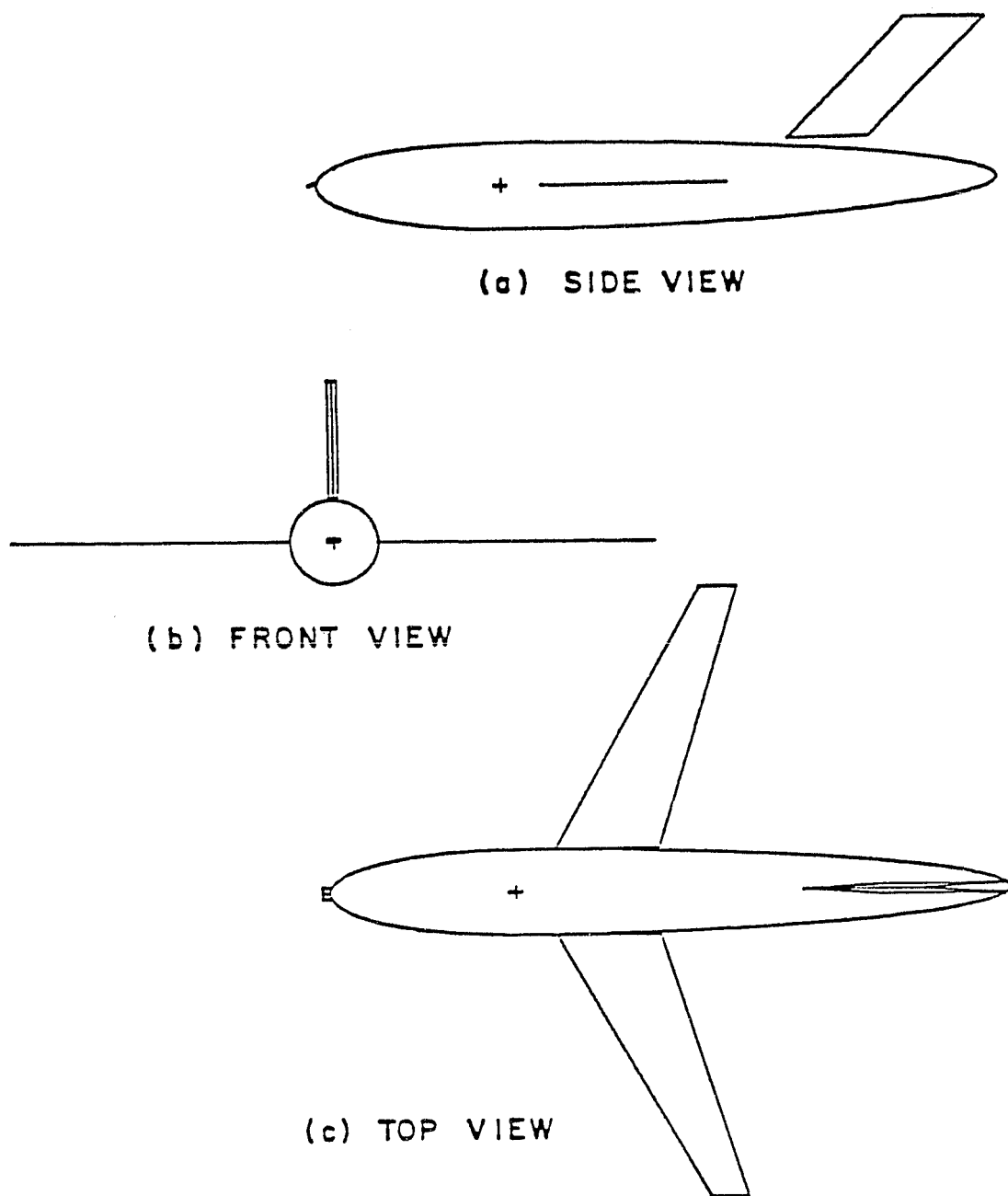
(a) SIDE VIEW

(b) FRONT VIEW

(c) TOP VIEW

Figure 19. Computer simulated model of a Boeing 737 aircraft. The wings and vertical stabilizer are modelled by perfectly conducting flat plates. The fuselage is modelled by a composite-ellipsoid.

SUM BEAM

NOSE

LEFT WING

RIGHT WING

TAIL

(SCALE: EACH DIVISION=10DB)

NORMALIZED TO 8.0 dB
ETH POLARIZATION
FREQ. = 1.06 GHz
THC = 90.0
PHC = 0.0
THETA = 90.0

NOSE

LEFT WING

RIGHT WING

TAIL
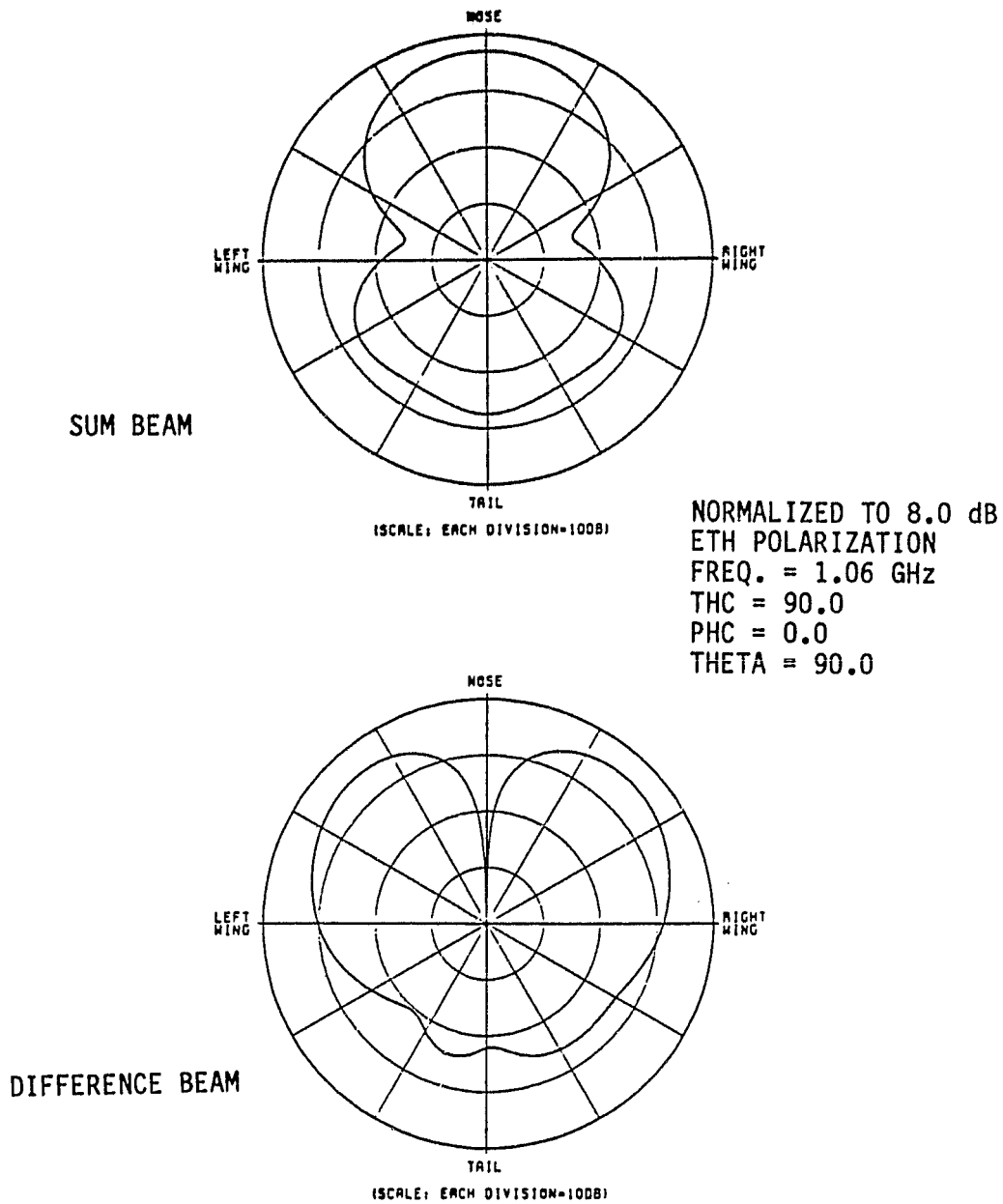
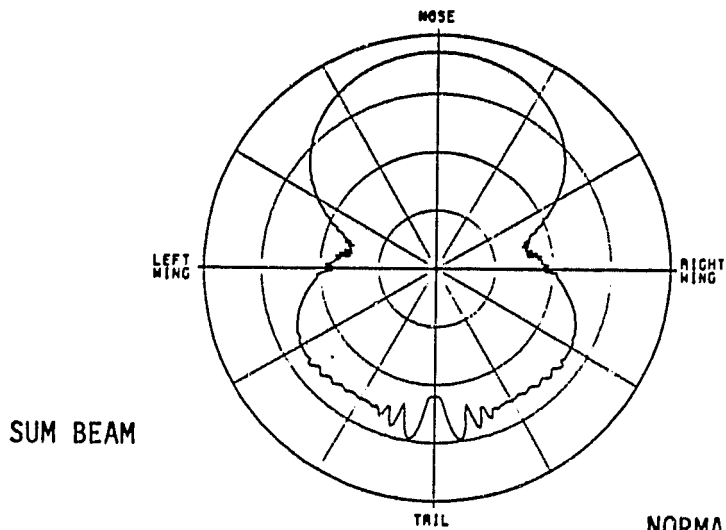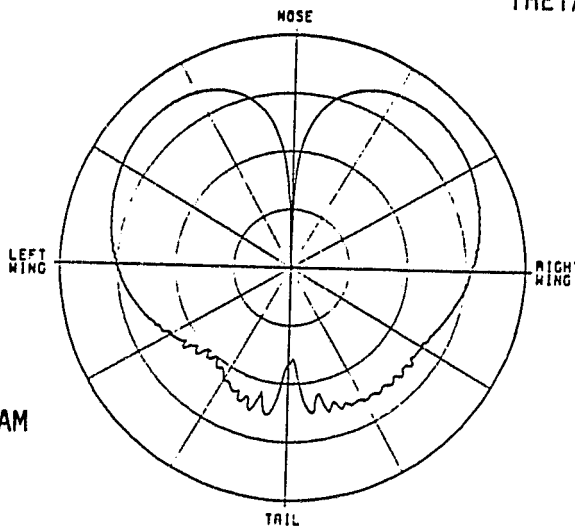(SCALE: EACH DIVISION=10DB)

DIFFERENCE BEAM

Figure 20. Sum and difference beams pointed in the nose direction.
The aircraft is modelled by a composite-ellipsoid only.
That is, the wings and tail are not included in the
computer simulation.

39

SUM BEAM

NOSE

LEFT WING

RIGHT WING

TAIL

(SCALE: EACH DIVISION=10DB)

NORMALIZED TO 8.0 dB
ETH POLARIZATION
FREQ. = 1.06 GHz
THC = 90.0
PHC = 0.0
THETA = 90.0

NOSE

LEFT WING

RIGHT WING

DIFFERENCE BEAM

TAIL

(SCALE: EACH DIVISION=10DB)

Figure 21.   Sum and difference beams pointed in the nose direction.
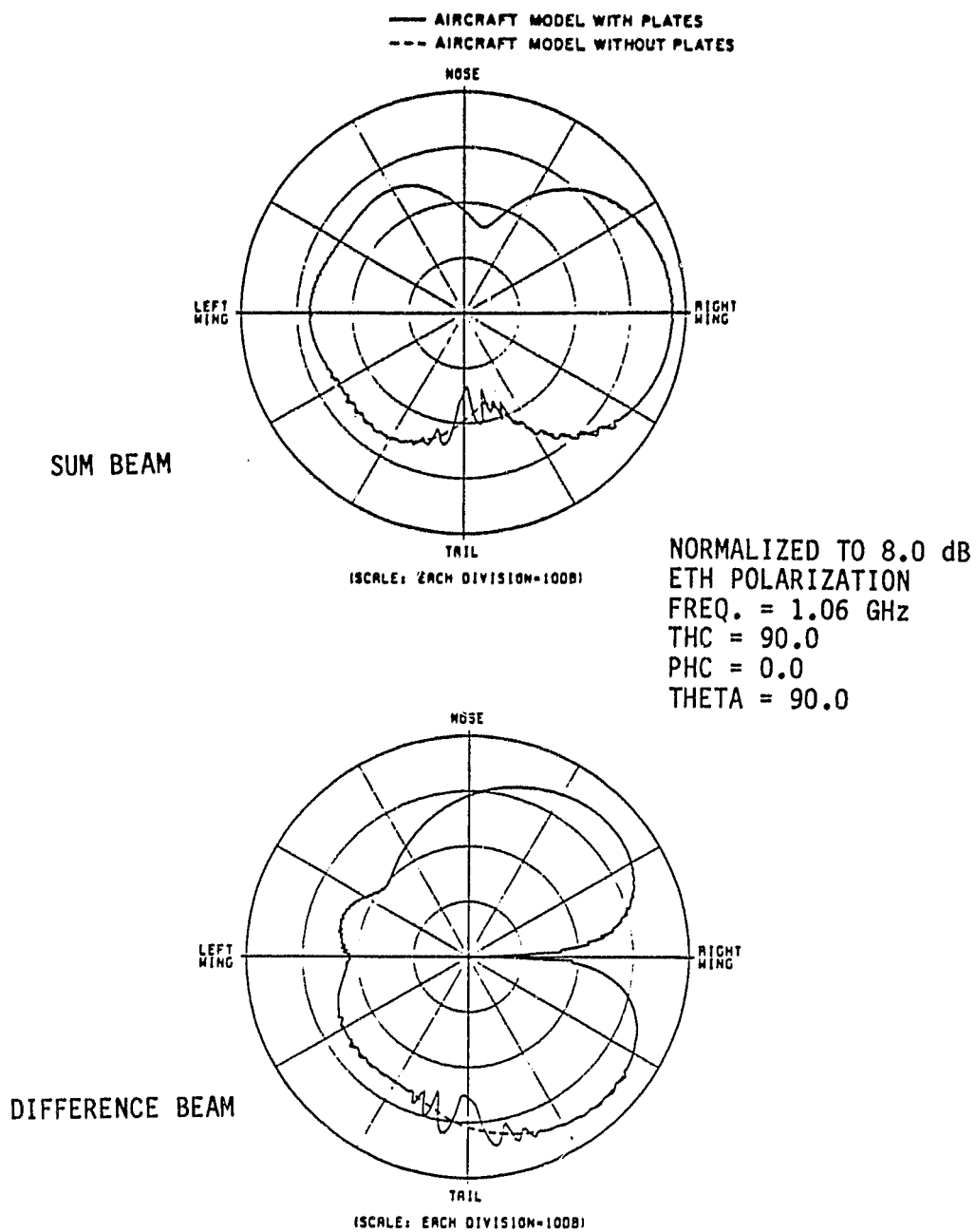   The computer model of the aircraft is shown in Figure 19.

40

SUM BEAM

TRIL
(SCALE: EACH DIVISION=10DB)

NORMALIZED TO 8.0 dB
ETH POLARIZATION
FREQ. = 1.06 GHz
THC = 90.0
PHC = 0.0
THETA = 90.0

DIFFERENCE BEAM

TRIL
(SCALE: EACH DIVISION=10DB)

Figure 22.   Sum and difference beams pointed in the right wing
             direction.

41

— AIRCRAFT MODEL WITH PLATES
--- AIRCRAFT MODEL WITHOUT PLATES

NOSE

LEFT
WING

RIGHT
WING

SUM BEAM

TAIL

(SCALE: EACH DIVISION=10DB)

NORMALIZED TO 8.0 dB
ETH POLARIZATION
FREQ. = 1.06 GHz
THC = 90.0
PHC = 0.0
THETA = 90.0

NOSE

LEFT
WING

RIGHT
WING

DIFFERENCE BEAM

TAIL

(SCALE: EACH DIVISION=10DB)
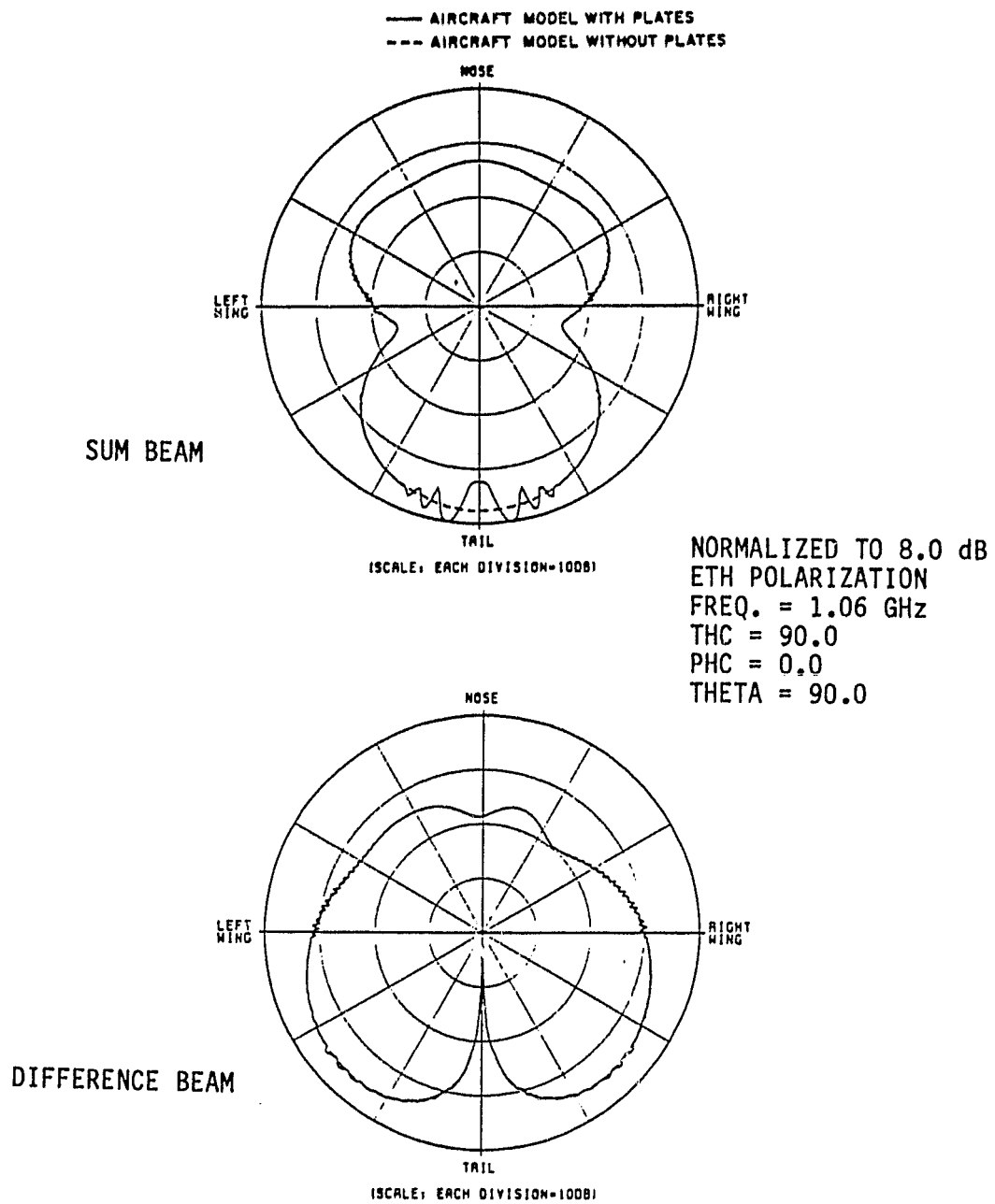
Figure 23. Sum and difference beams pointed toward the tail of the
            aircraft.

42

CONICAL PATTERN ANGLE   90

BEAM POSITION   0

—— AIRCRAFT MODEL WITH PLATES
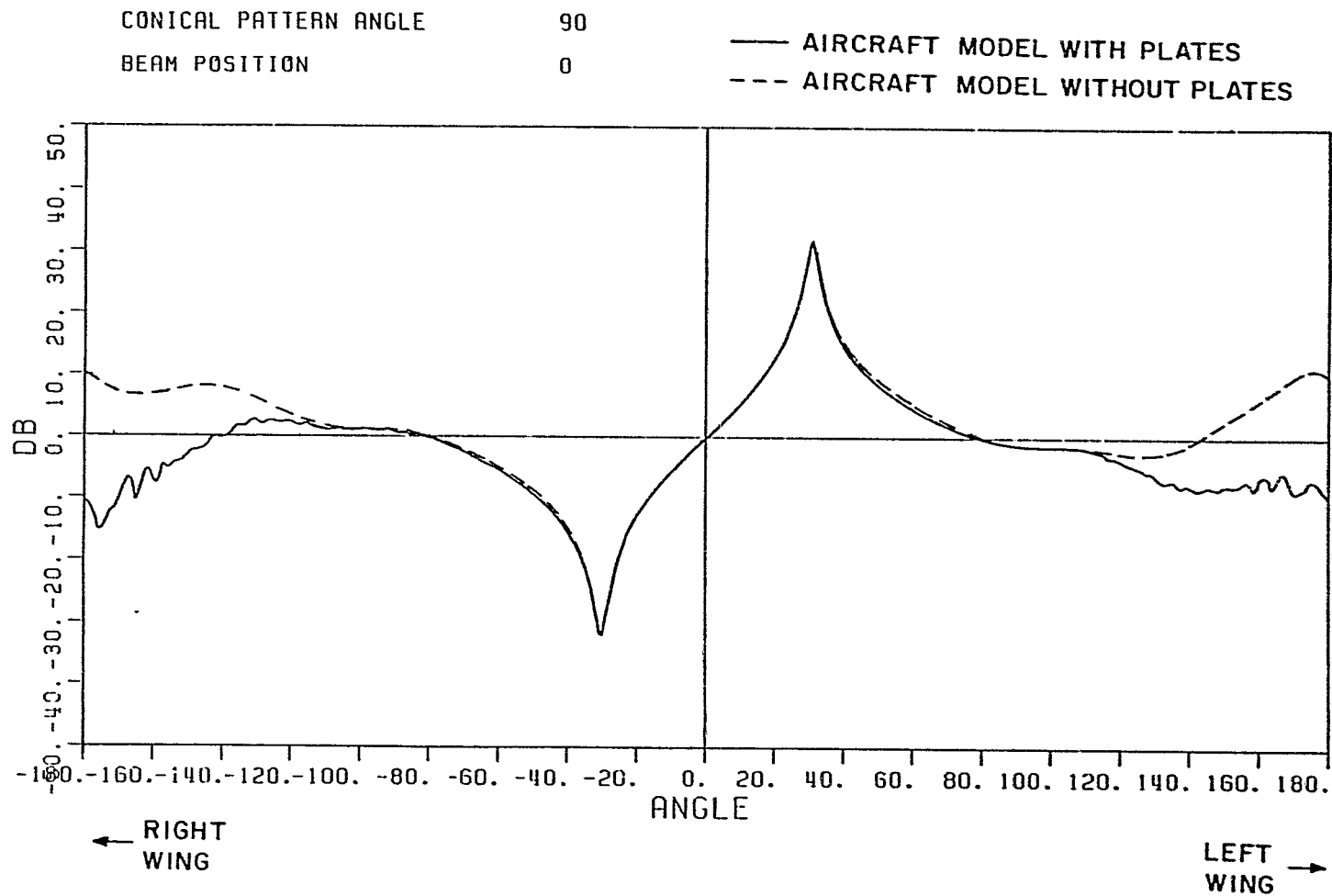
– – – AIRCRAFT MODEL WITHOUT PLATES

RIGHT
WING

LEFT
WING

Figure 24.   Monopulse curves corresponding to Figures 20 and 21.
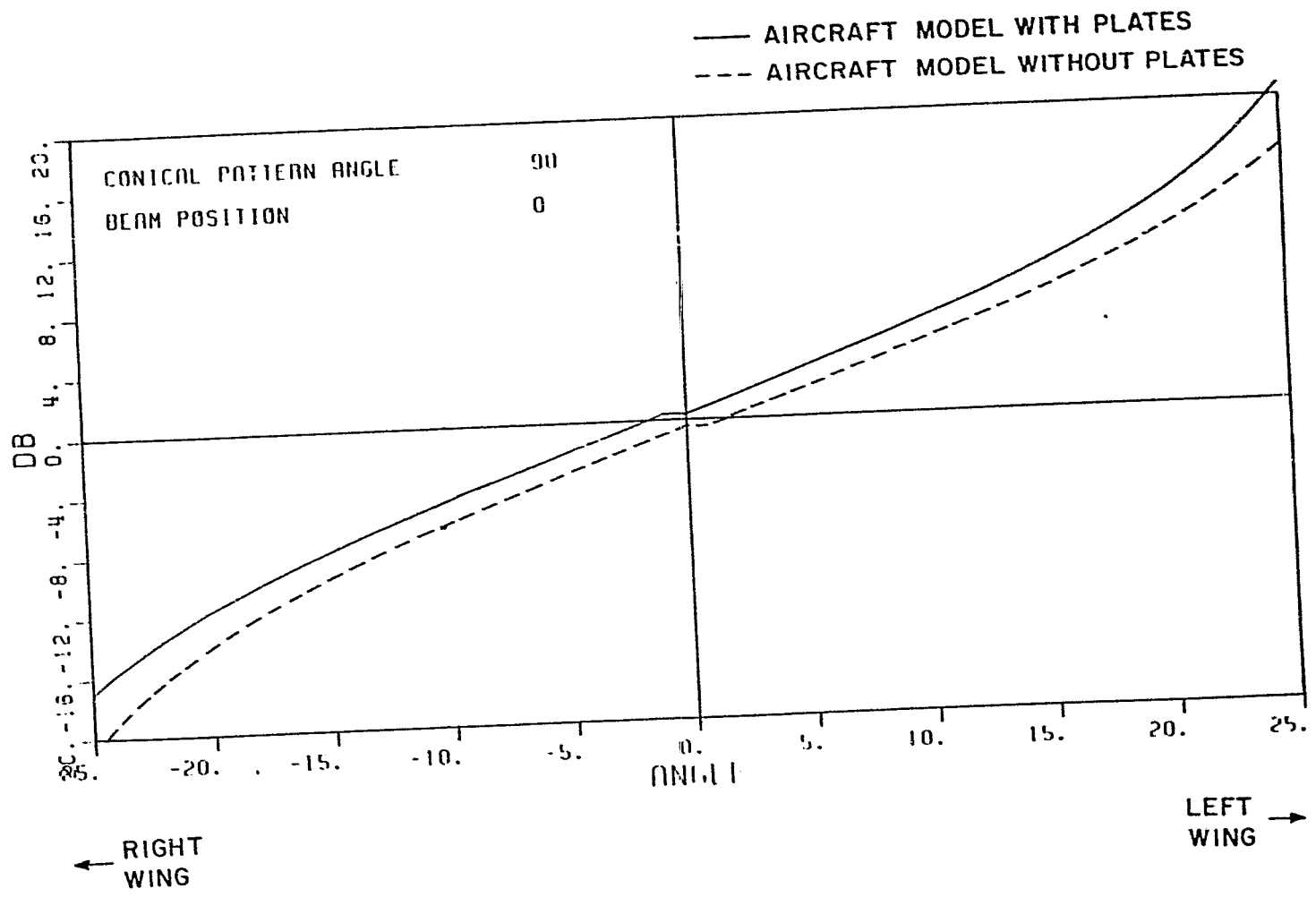
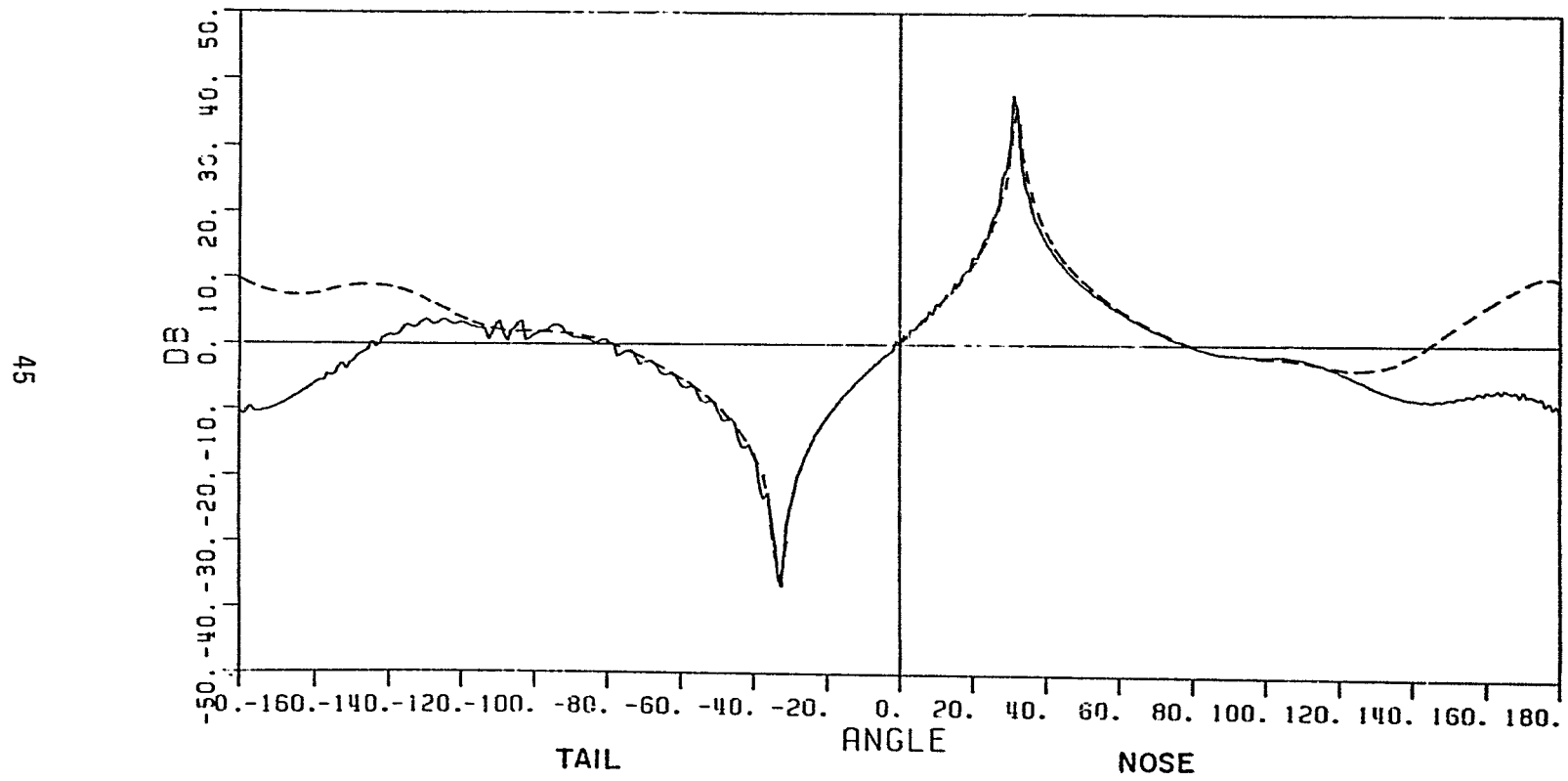Figure 25. Monopulse curves corresponding to Figures 20 and 21.

44

Figure 26. Monopulse curve corresponding to Figure 22.
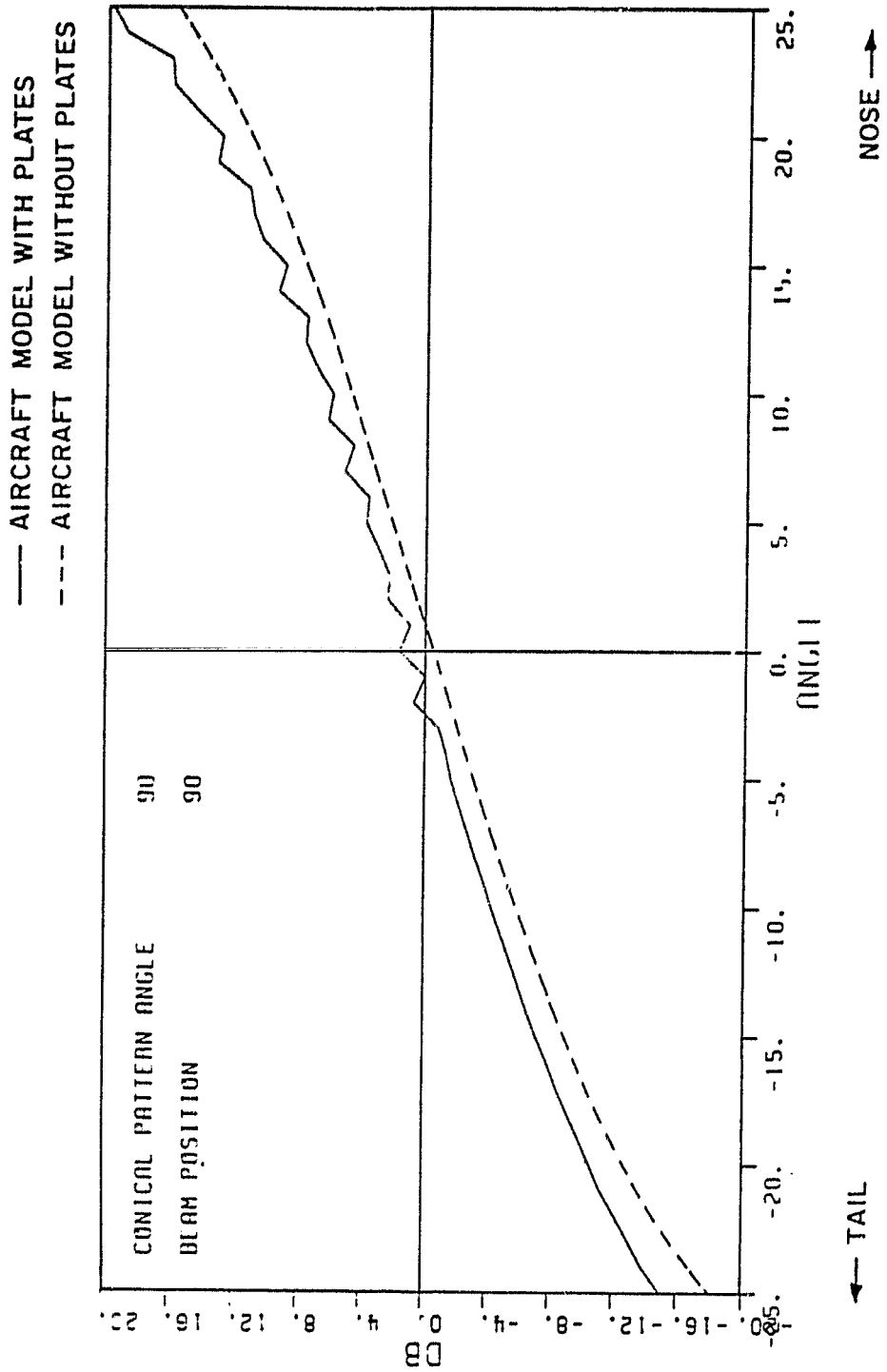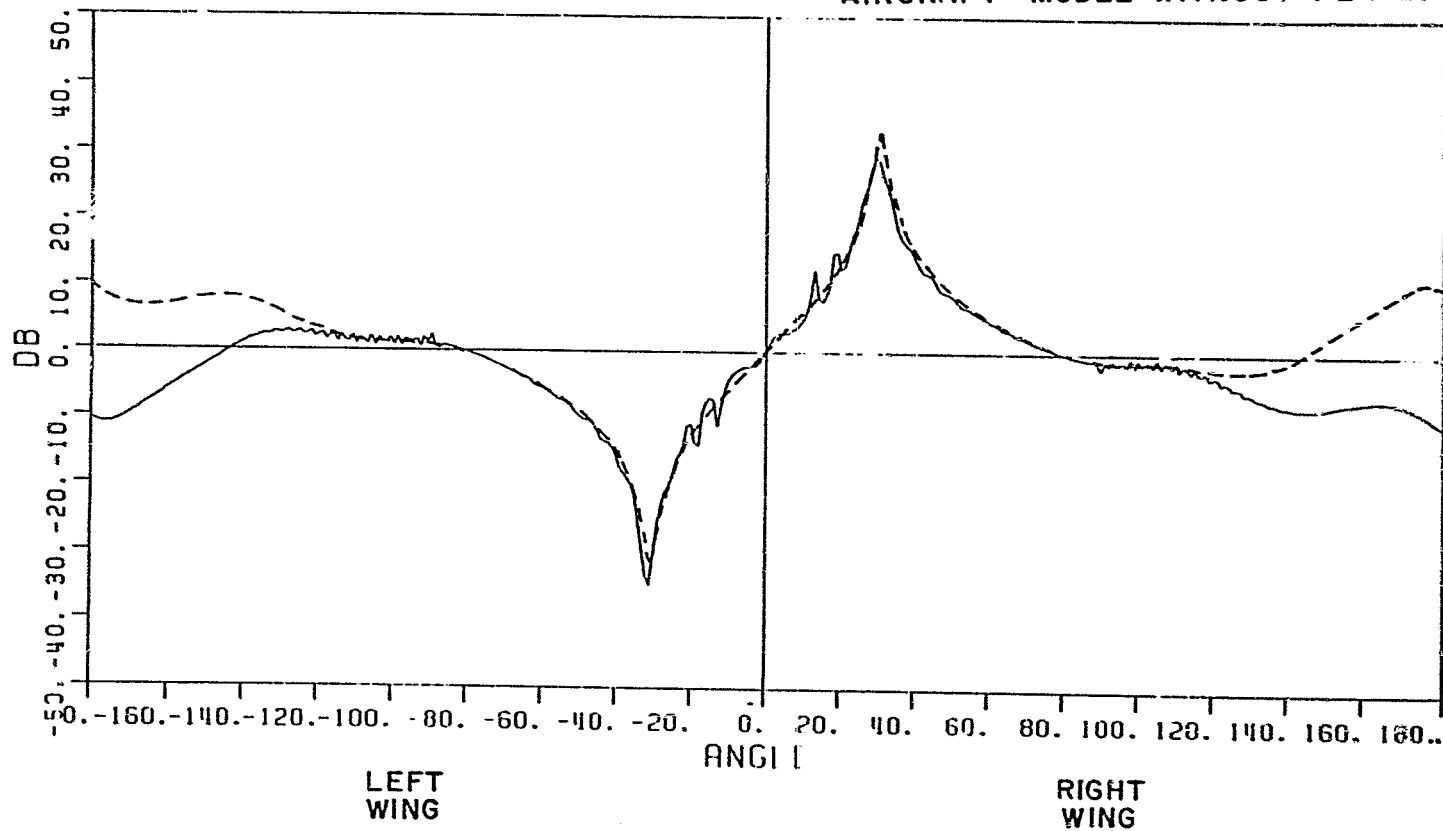
Figure 27. Monopulse curves corresponding to Figure 22.

46

CONICAL PATTERN ANGLE   90

BEAM POSITION   180   ———— AIRCRAFT MODEL WITH PLATES

                                       ———— AIRCRAFT MODEL WITHOUT PLATES

LEFT
WING

RIGHT
WING

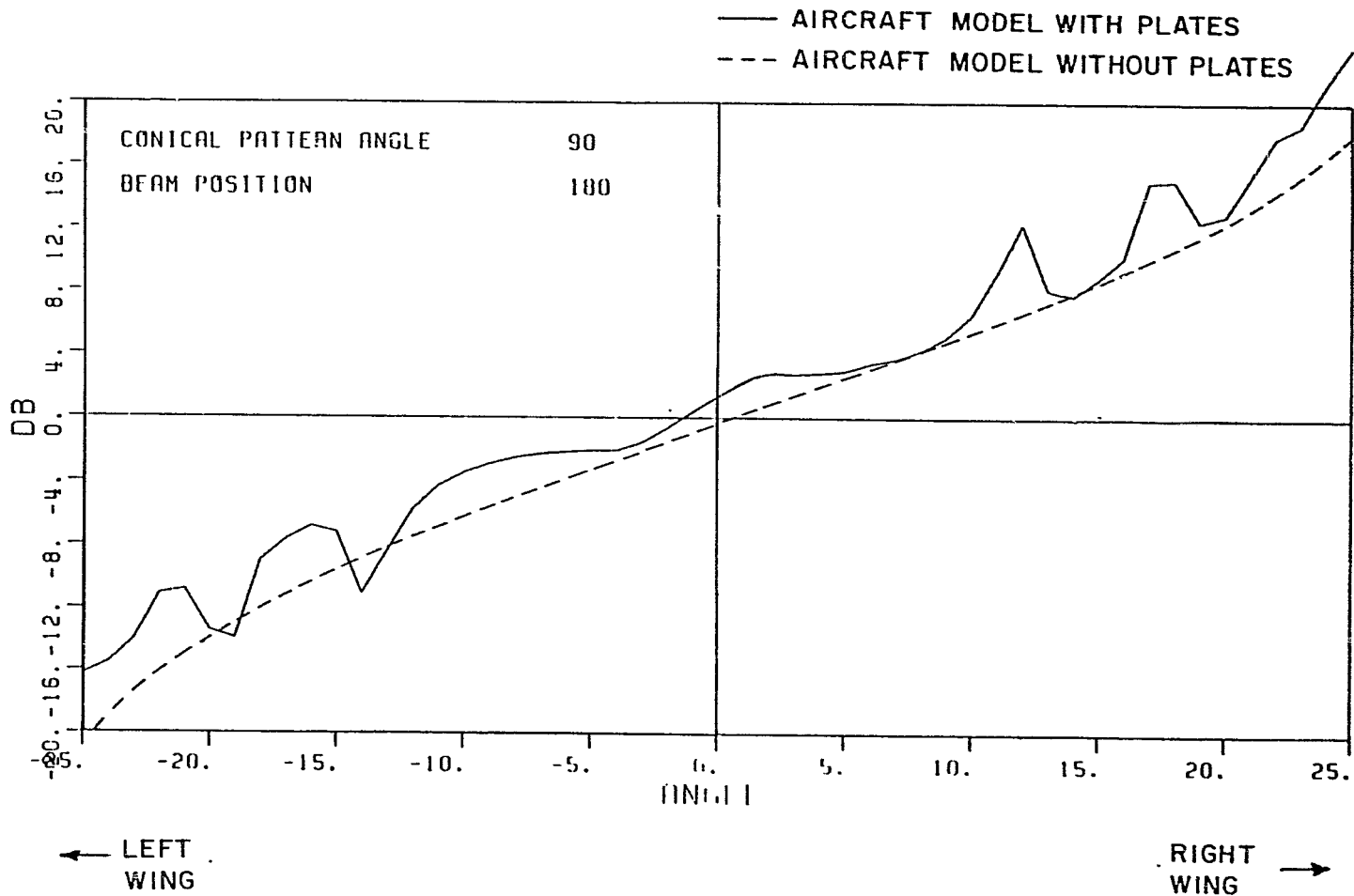Figure 28. Monopulse curve corresponding to Figure 23.

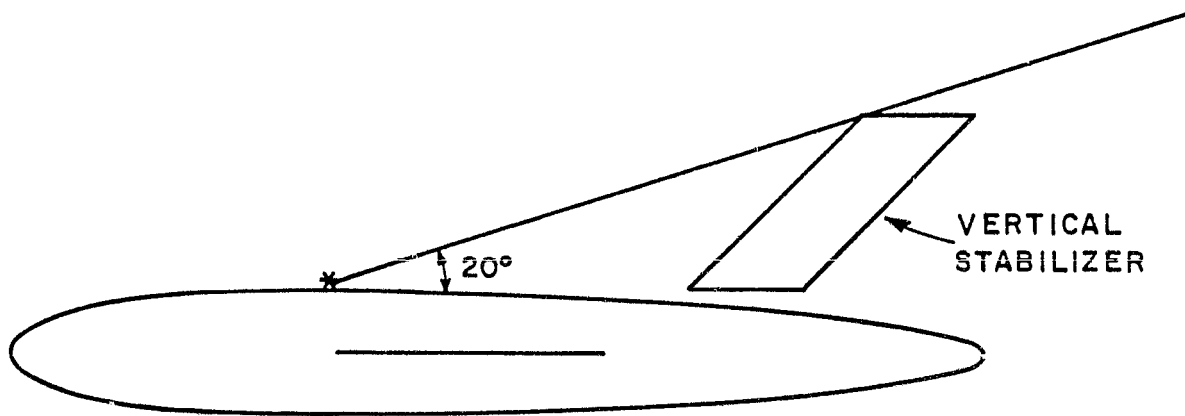Figure 29. Monopulse curves corresponding to Figure 23.

48

Figure 30. Geometry that illustrates the shadowing of the circular array by the vertical stabilizer.

NOSE

LEFT WING — RIGHT WING

SUM BEAM   NORMALIZED TO 7.2 dB

TAIL

(SCALE: EACH DIVISION=10DB)   ETH POLARIZATION
FREQ. = 1.06 GHz
THC = 90.0
PHC = 0.0
THETA = 60.0

NOSE

LEFT WING — RIGHT WING

DIFFERENCE BEAM   NORMALIZED TO 7.0 dB

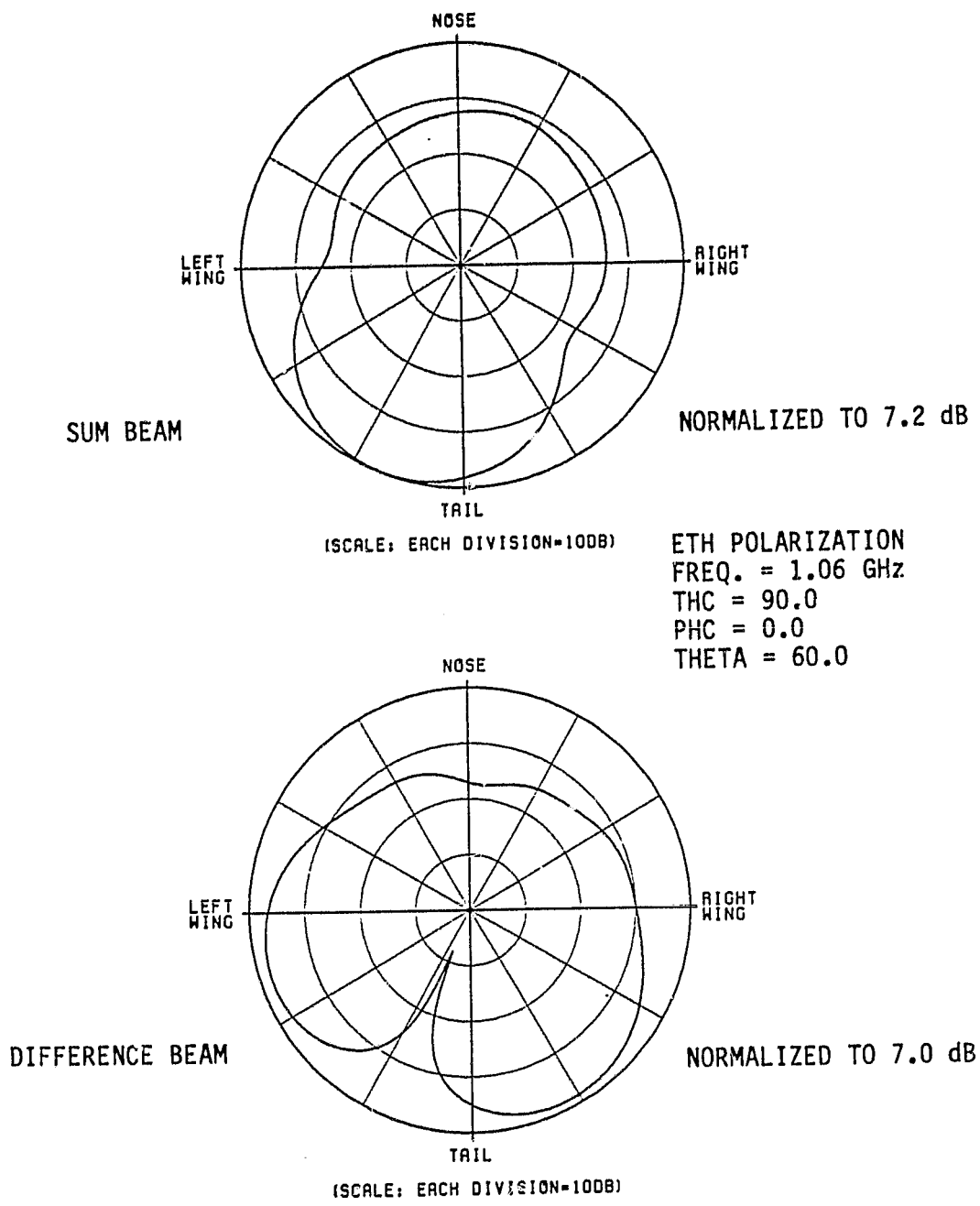TAIL

(SCALE: EACH DIVISION=10DB)

Figure 31.   Radiation patterns of circular array where only the source
field is included. That is, no reflected or diffracted
fields are included. The beams are pointed in the direction
23° to the left of the tail.

50

NOSE

LEFT
WING

RIGHT
WING

SUM BEAM

NORMALIZED TO 1.0 dB

TAIL

(SCALE: EACH DIVISION=10DB)

EPH POLARIZATION
FREQ. = 1.06 GHz
THC = 90.0
PHC = 0.0
THETA = 60.0

NOSE

LEFT
WING

RIGHT
WING

DIFFERENCE BEAM

NORMALIZED TO 7.0 dB
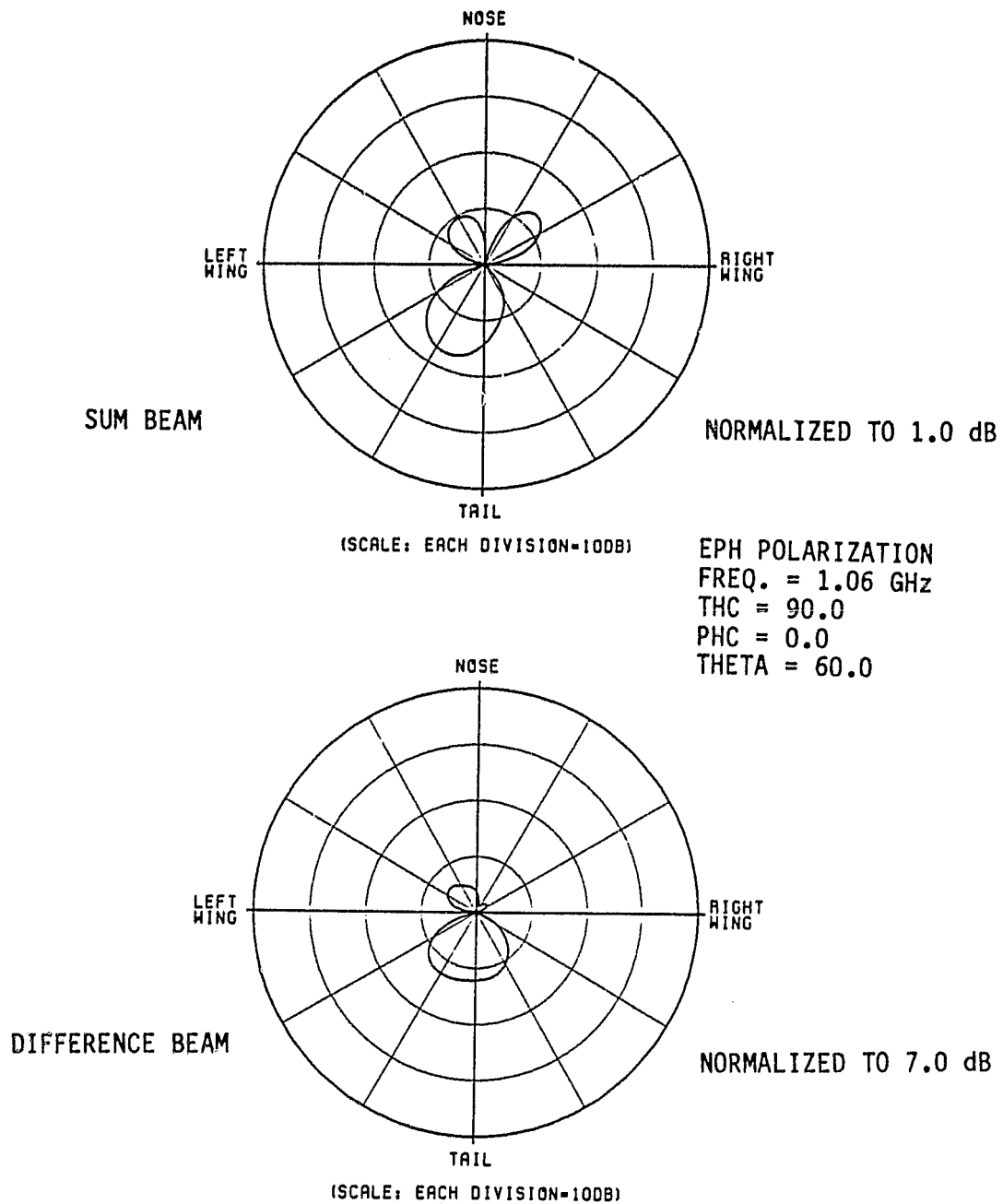
TAIL

(SCALE: EACH DIVISION=10DB)

Figure 32. E_{ϕ_D} component of radiation pattern of circular array. Note
that only the source field is included. That is, no
reflected or diffracted fields are included. The beams are
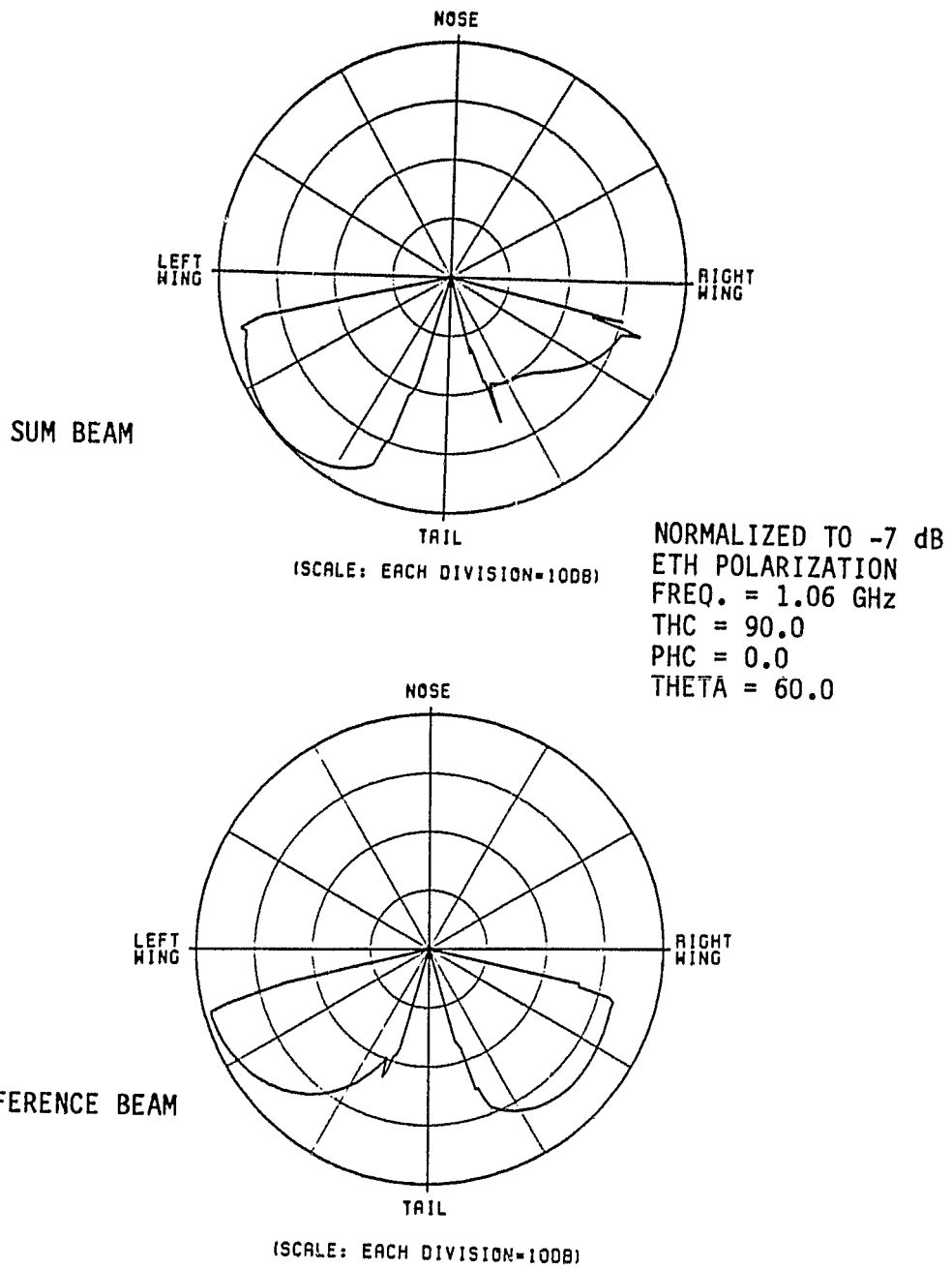pointed 23° to the left of the tail.

51

NOSE

SUM BEAM

TAIL

(SCALE: EACH DIVISION=10DB)

NORMALIZED TO -7 dB
ETH POLARIZATION
FREQ. = 1.06 GHz
THC = 90.0
PHC = 0.0
THETA = 60.0

NOSE

DIFFERENCE BEAM

TAIL

(SCALE: EACH DIVISION=10DB)

Figure 33. Reflected field only.

52

SUM BEAM

(SCALE: EACH DIVISION=10DB)

NORMALIZED TO 7.0 dB
ETH POLARIZATION
FREQ. = 1.06 GHz
THC = 90.0
PHC = 0.0
THETA = 60.0

DIFFERENCE BEAM

(SCALE: EACH DIVISION=10DB)
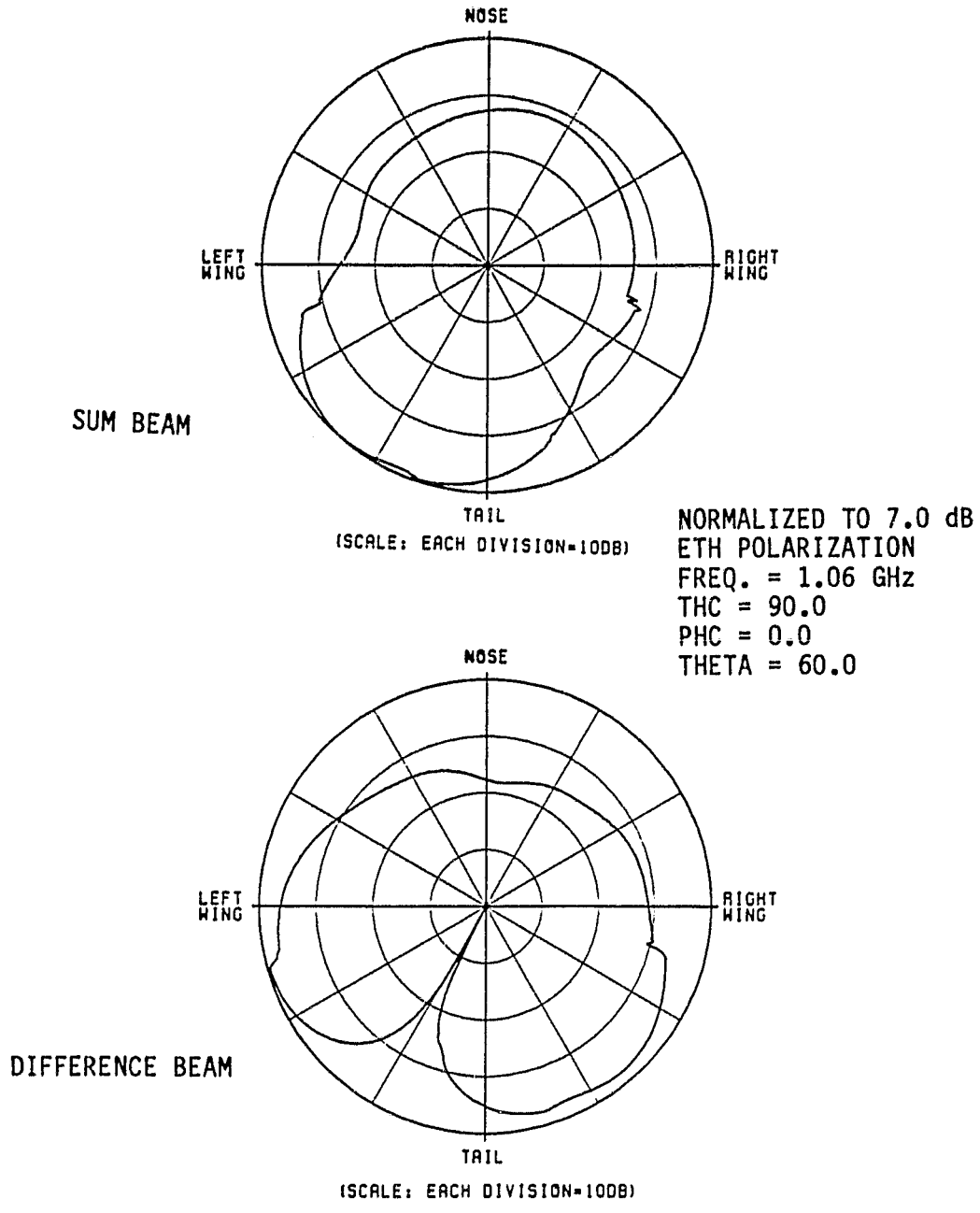
Figure 34. Superposition of the source and reflected fields.

NOSE

LEFT
WING

RIGHT
WING

SUM BEAM

TAIL

(SCALE: EACH DIVISION=10DB)

NORMALIZED TO -7 dB
ETH POLARIZATION
FREQ. = 1.06 GHz
THC = 90.0
PHC = 0.0
THETA = 60.0

NOSE

LEFT
WING

RIGHT
WING

DIFFERENCE BEAM

TAIL

(SCALE: EACH DIVISION=10DB)
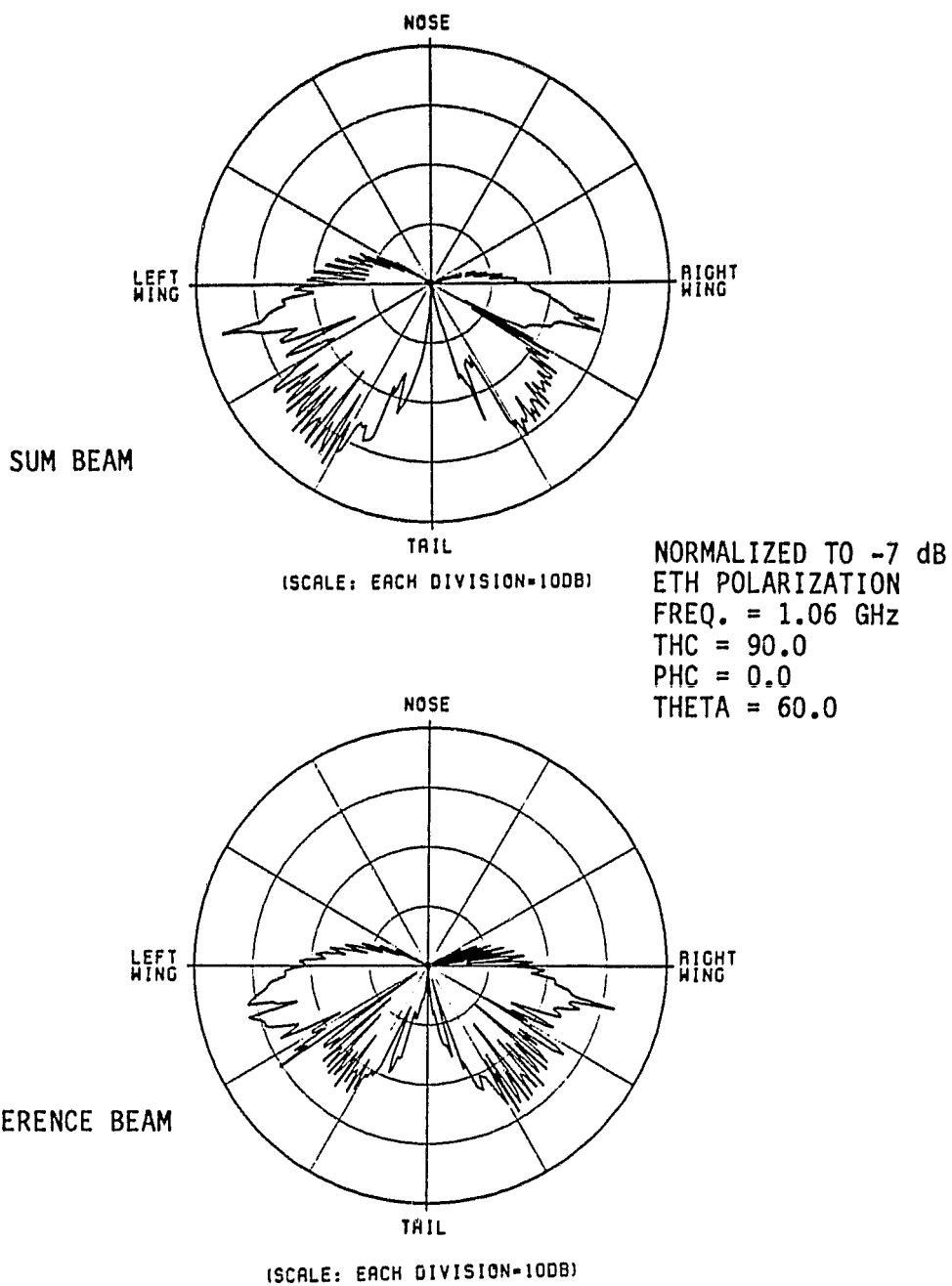
Figure 35. Edge diffracted field only.

54

NOSE

LEFT WING

RIGHT WING

SUM BEAM

TAIL

(SCALE: EACH DIVISION=10DB)

NORMALIZED TO 7.0 dB
ETH POLARIZATION
FREQ. = 1.06 GHz
THC = 90.0
PHC = 0.0
THETA = 60.0

NOSE

LEFT WING

RIGHT WING

DIFFERENCE BEAM

TAIL

(SCALE: EACH DIVISION=10DB)
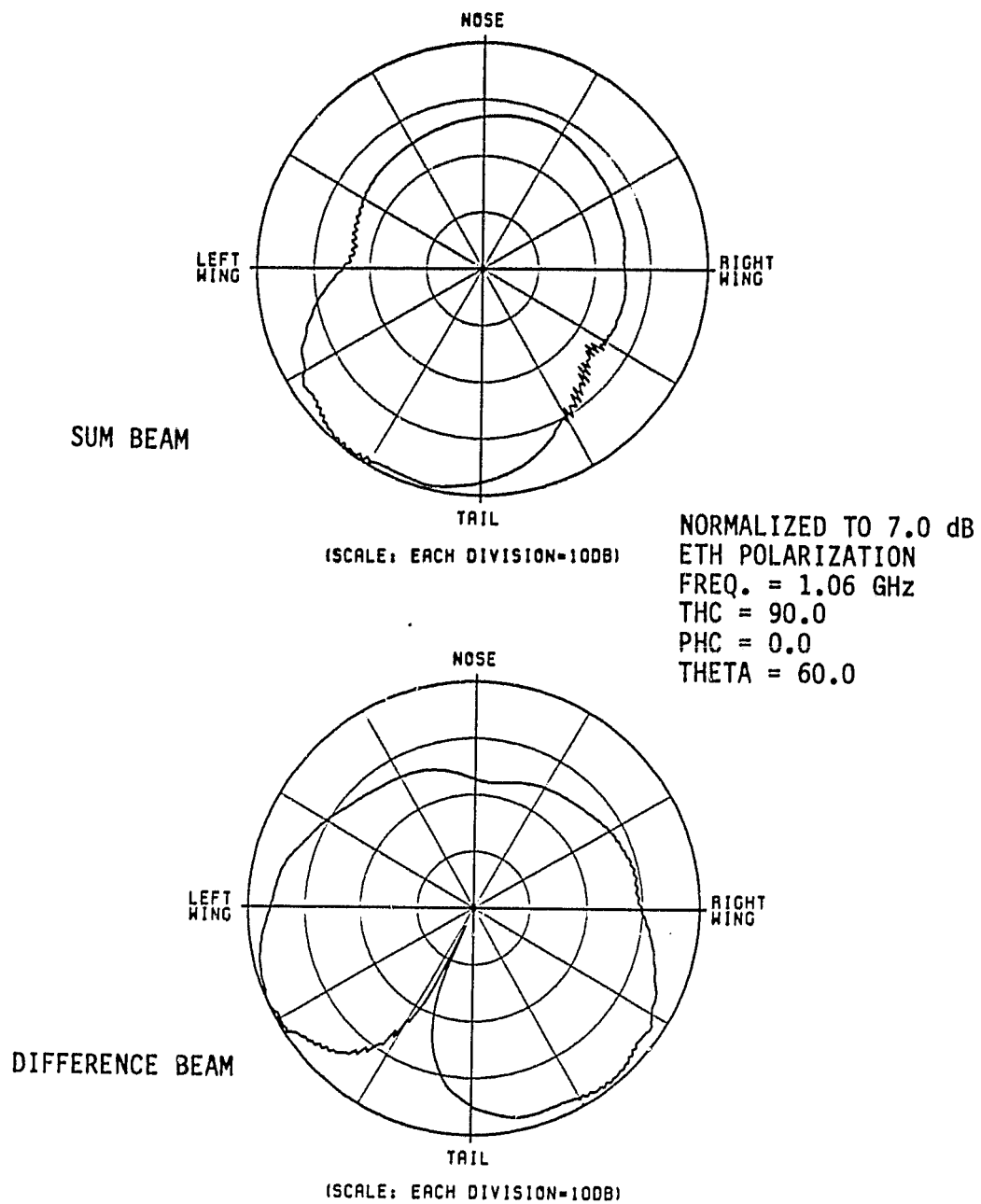
Figure 36. Superposition of the source (Figure 31), reflected (Figure 33) and diffracted (Figure 35) fields. The beams are pointed 23° to the left of the tail.

55

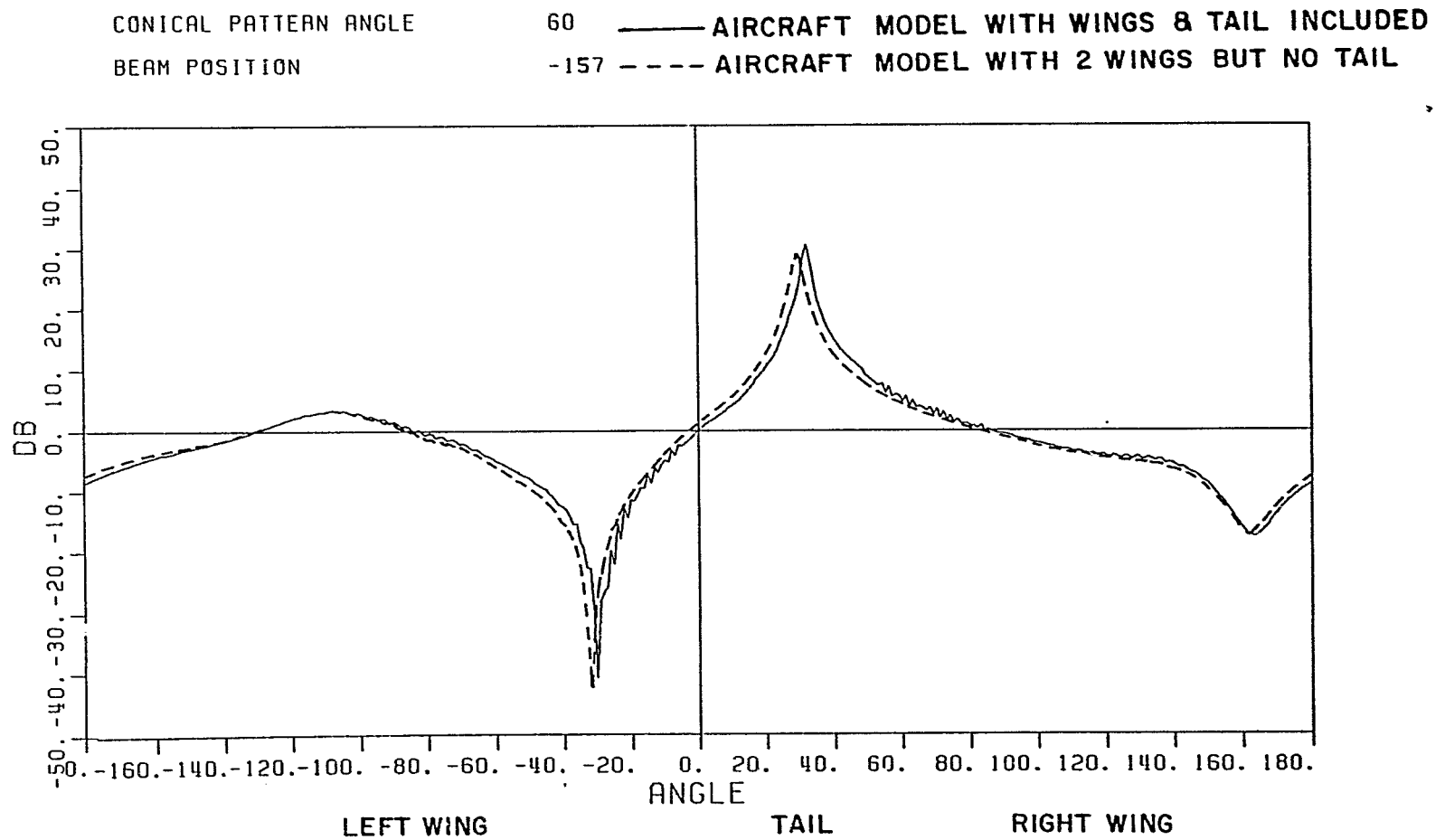CONICAL PATTERN ANGLE   60   ────── AIRCRAFT MODEL WITH WINGS & TAIL INCLUDED

BEAM POSITION   -157 ─ ─ ─ ─ AIRCRAFT MODEL WITH 2 WINGS BUT NO TAIL

LEFT WING   TAIL   RIGHT WING

Figure 37.   Monopulse curve corresponding to Figure 36.
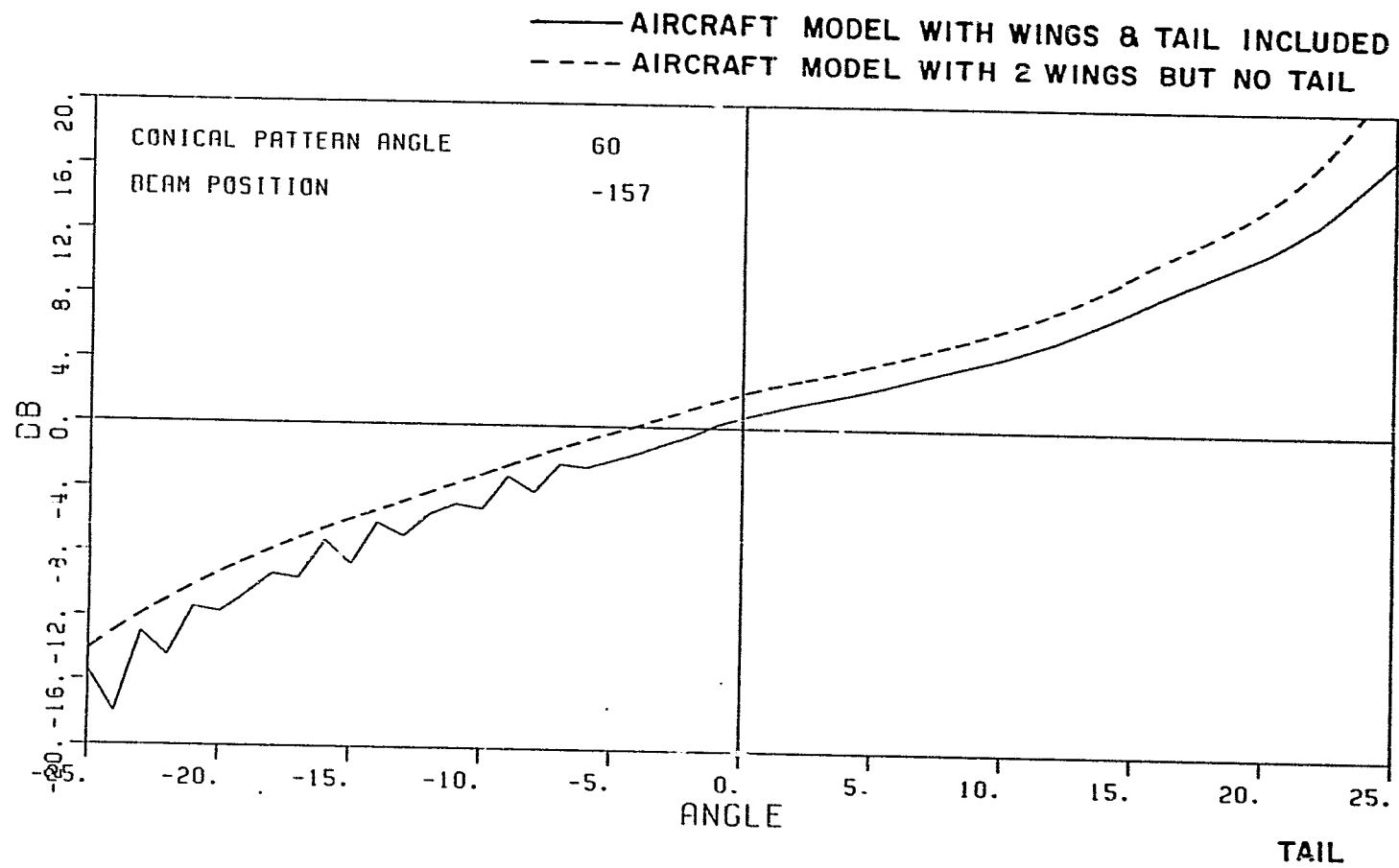
Figure 38. Monopulse curve corresponding to Figure 36.

57

NOSE

SUM BEAM   NORMALIZED TO 8.95 dB

TAIL

(SCALE: EACH DIVISION=10DB)

EPH POLARIZATION
FREQ. = 1.06 GHz
THC = 90.0
PHC = 0.0
THETA = 65.0

NOSE

DIFFERENCE BEAM   NORMALIZED TO 8.1 dB

TAIL

(SCALE: EACH DIVISION=10DB)
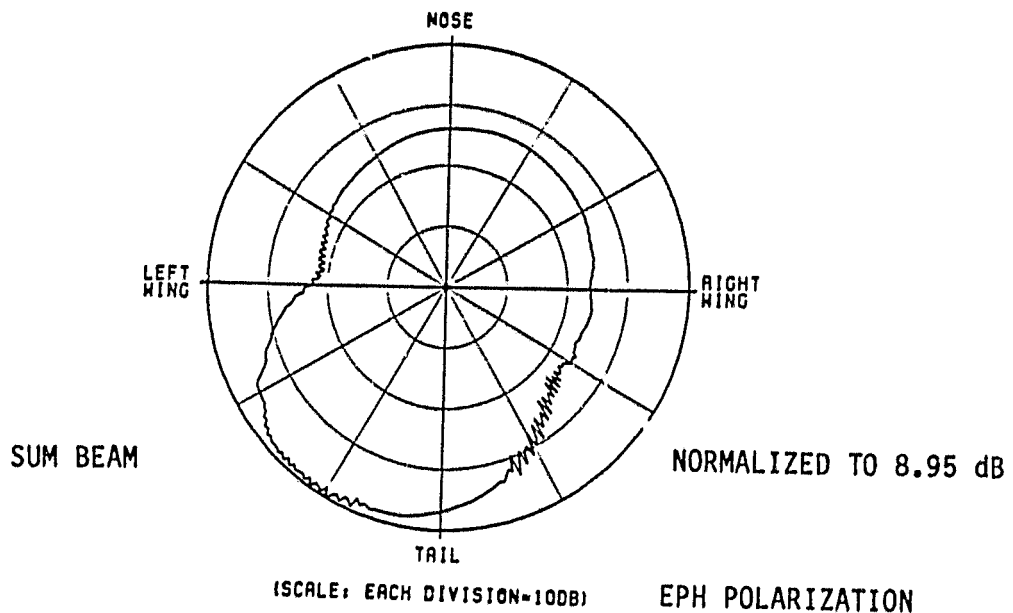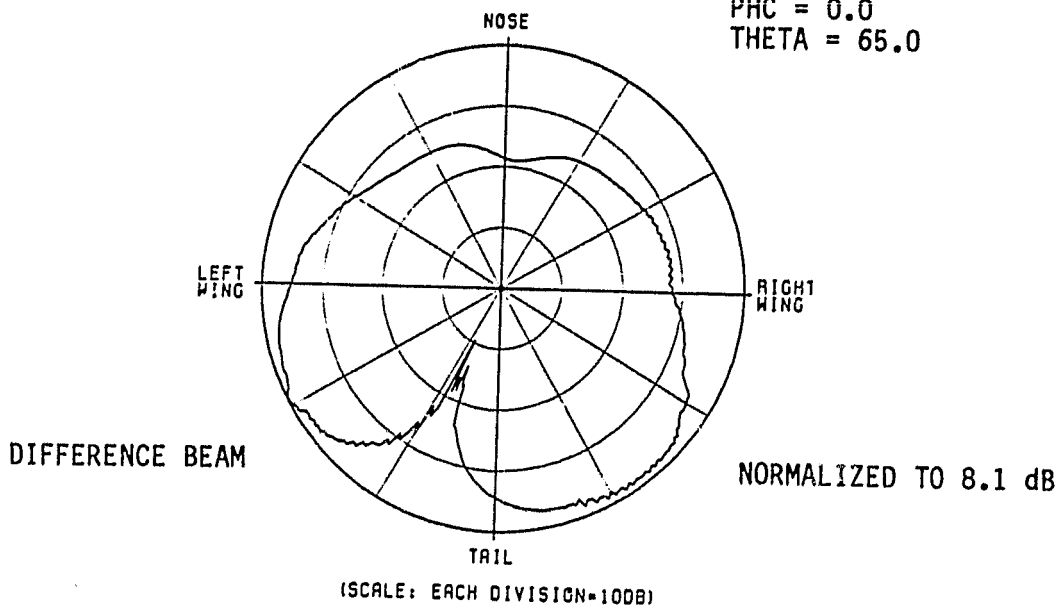
Figure 39.   Sum and difference beams pointed in the direction 23° to the
             left of the tail.

58

CONICAL PATTERN ANGLE   65

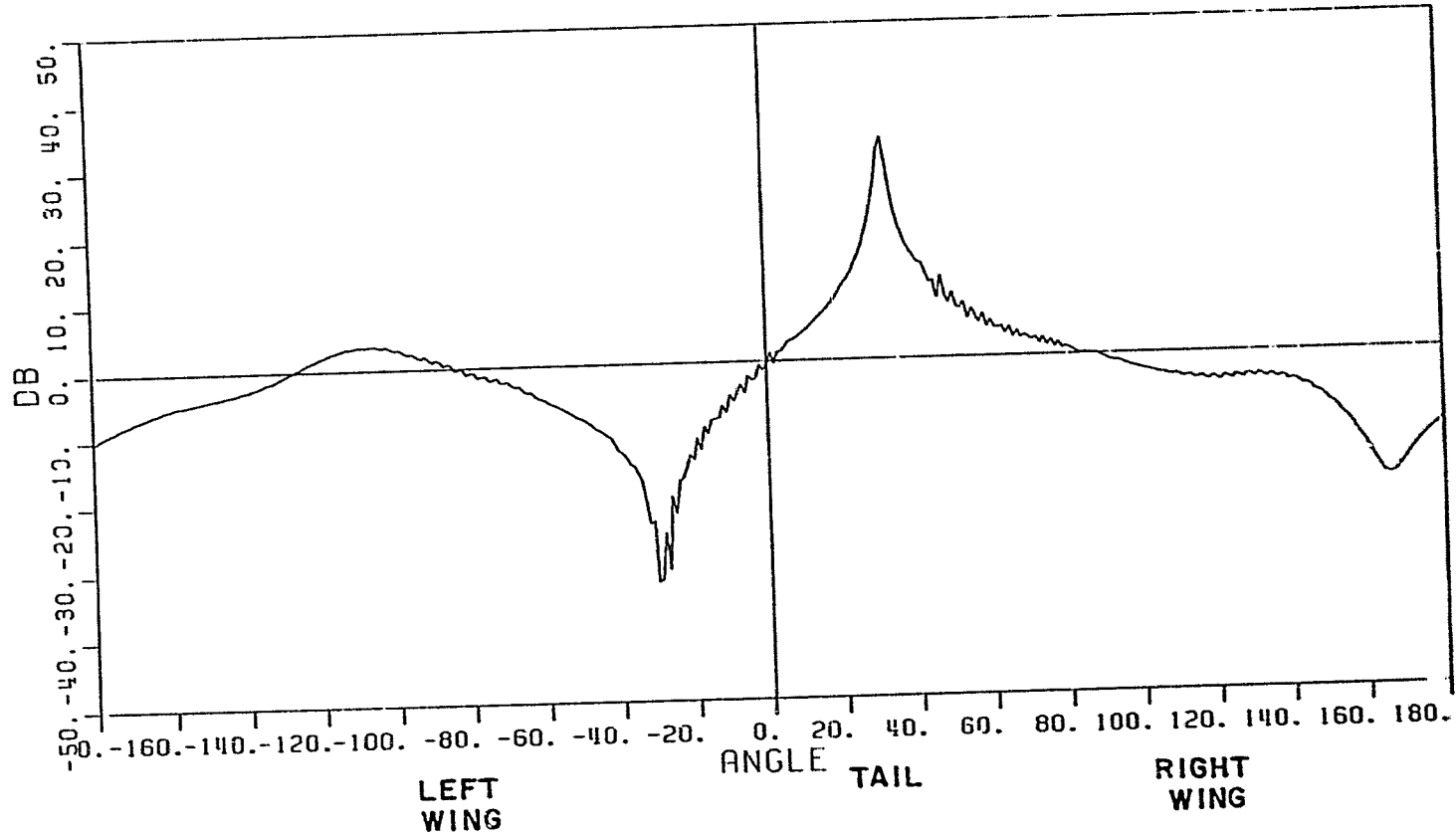BEAM POSITION   -157   AIRCRAFT MODEL WITH PLATES

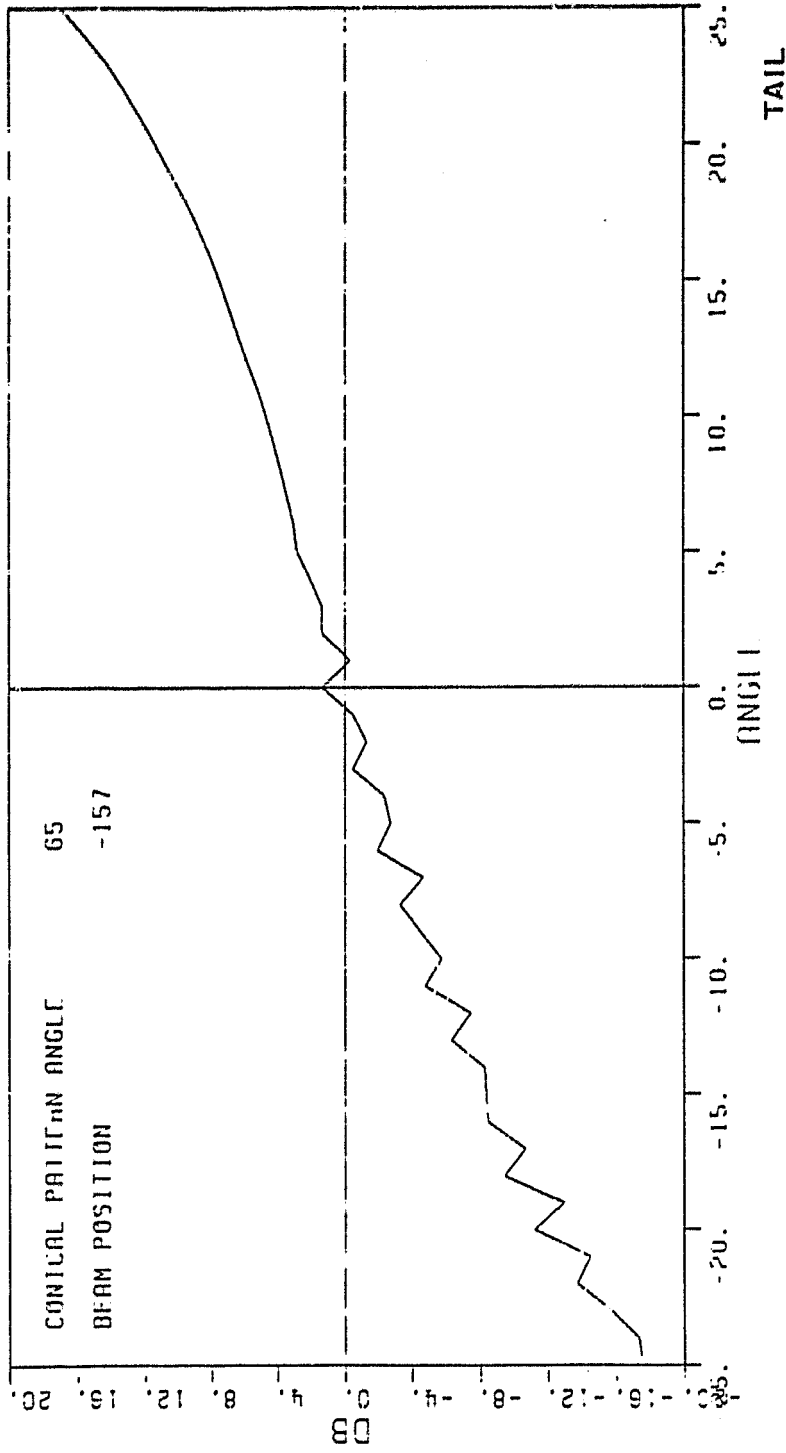Figure 40. Monopulse curve corresponding to Figure 39.

AIRCRAFT MODEL WITH PLATES

Figure 41. Monopulse curve corresponding to Figure 39.
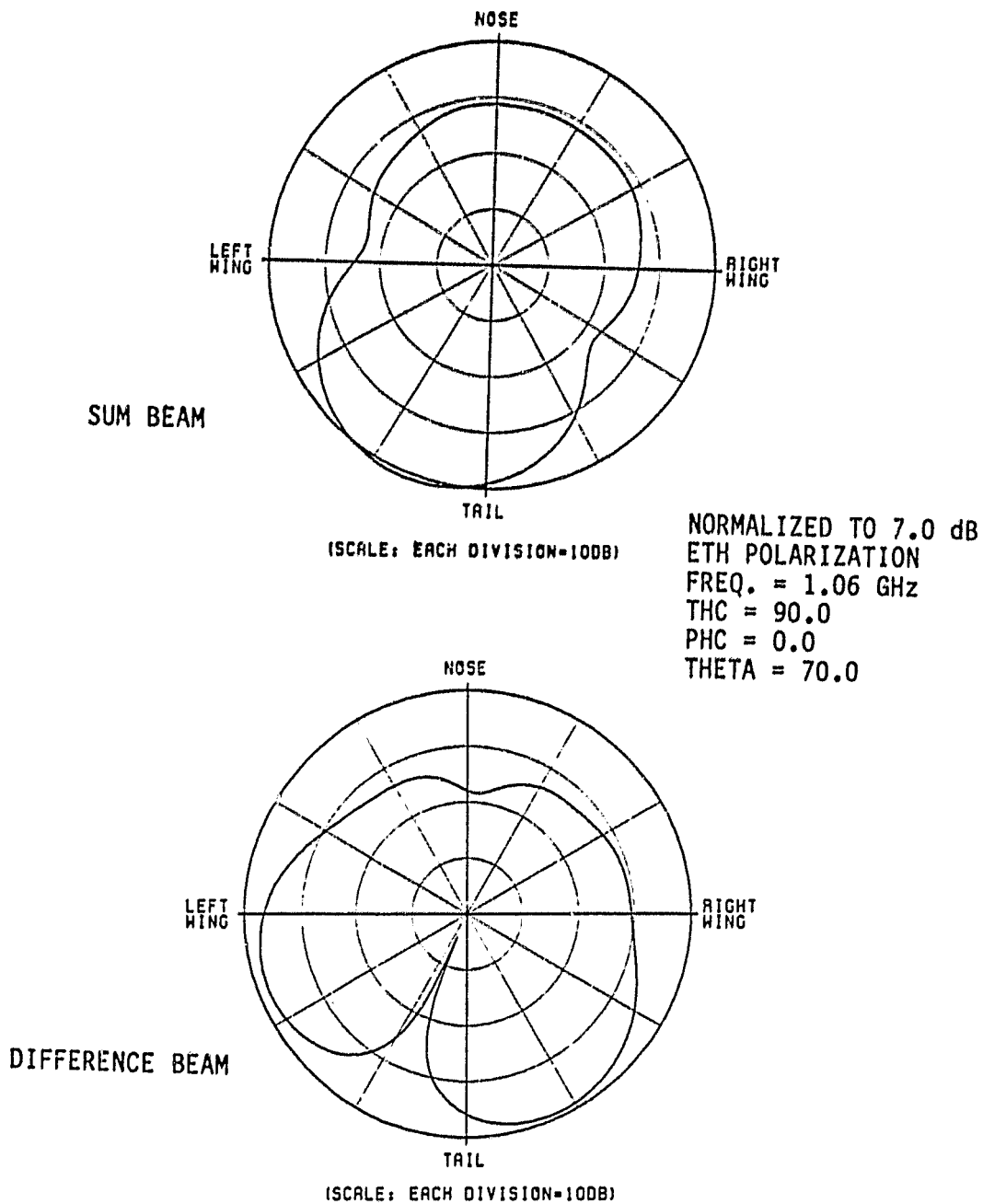
NOSE

LEFT
WING

RIGHT
WING

SUM BEAM

TAIL

(SCALE: EACH DIVISION=10DB)

NORMALIZED TO 7.0 dB
ETH POLARIZATION
FREQ. = 1.06 GHz
THC = 90.0
PHC = 0.0
THETA = 70.0

NOSE

LEFT
WING

RIGHT
WING

DIFFERENCE BEAM

TAIL

(SCALE: EACH DIVISION=10DB)

Figure 42.   Radiation patterns of circular array where only the source
field is included. The beams are pointed in the direction
23° to the left of the tail.

NOSE
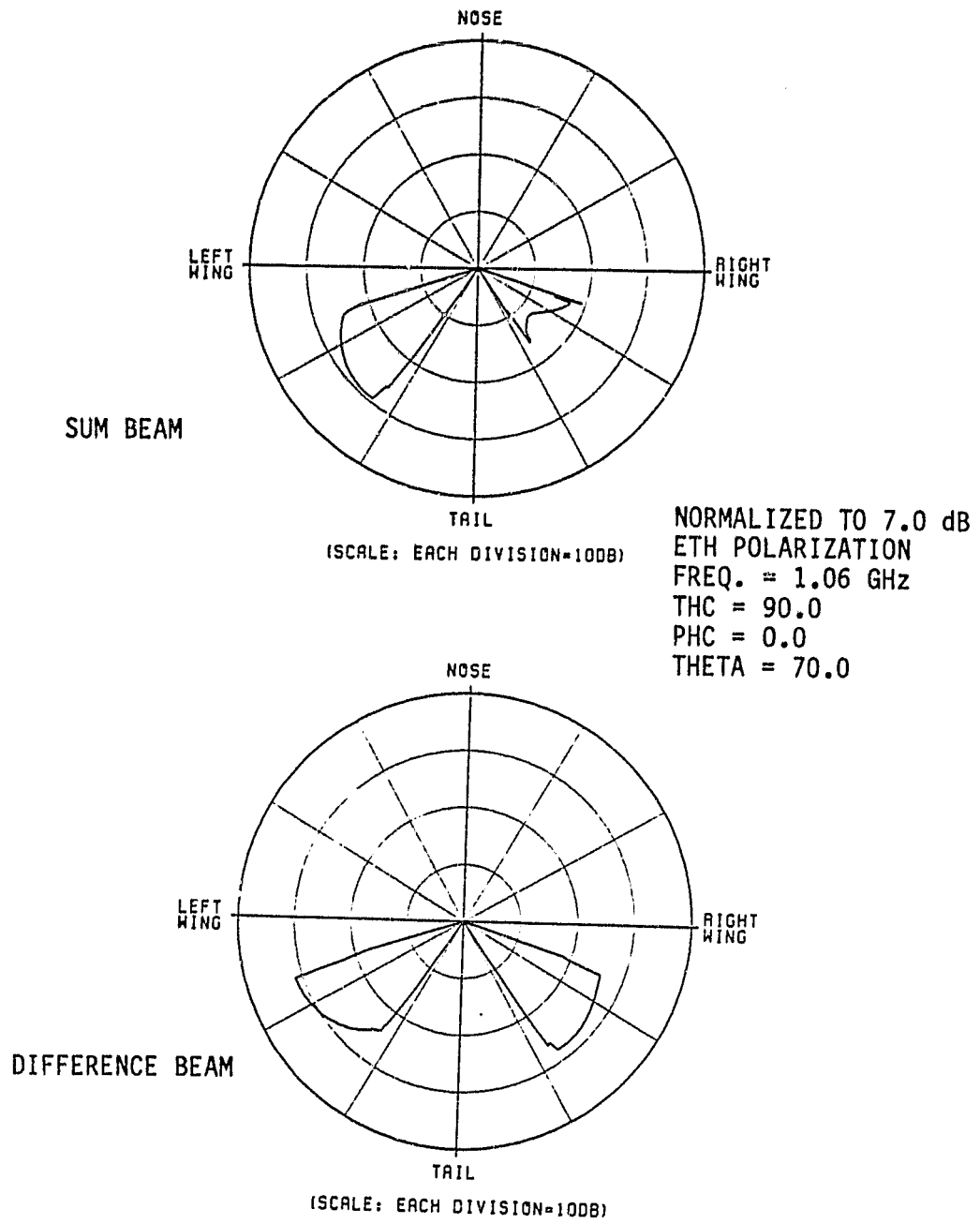
LEFT
WING

RIGHT
WING

SUM BEAM

TAIL

(SCALE: EACH DIVISION=10DB)

NORMALIZED TO 7.0 dB
ETH POLARIZATION
FREQ. = 1.06 GHz
THC = 90.0
PHC = 0.0
THETA = 70.0

NOSE

LEFT
WING

RIGHT
WING

DIFFERENCE BEAM

TAIL

(SCALE: EACH DIVISION=10DB)

Figure 43.   Reflected field only.

SUM BEAM   NORMALIZED TO 7.1 dB

(SCALE: EACH DIVISION=10DB)   ETH POLARIZATION
                              FREQ. = 1.06 GHz
                              THC = 90.0
                              PHC = 0.0
                              THETA = 70.0
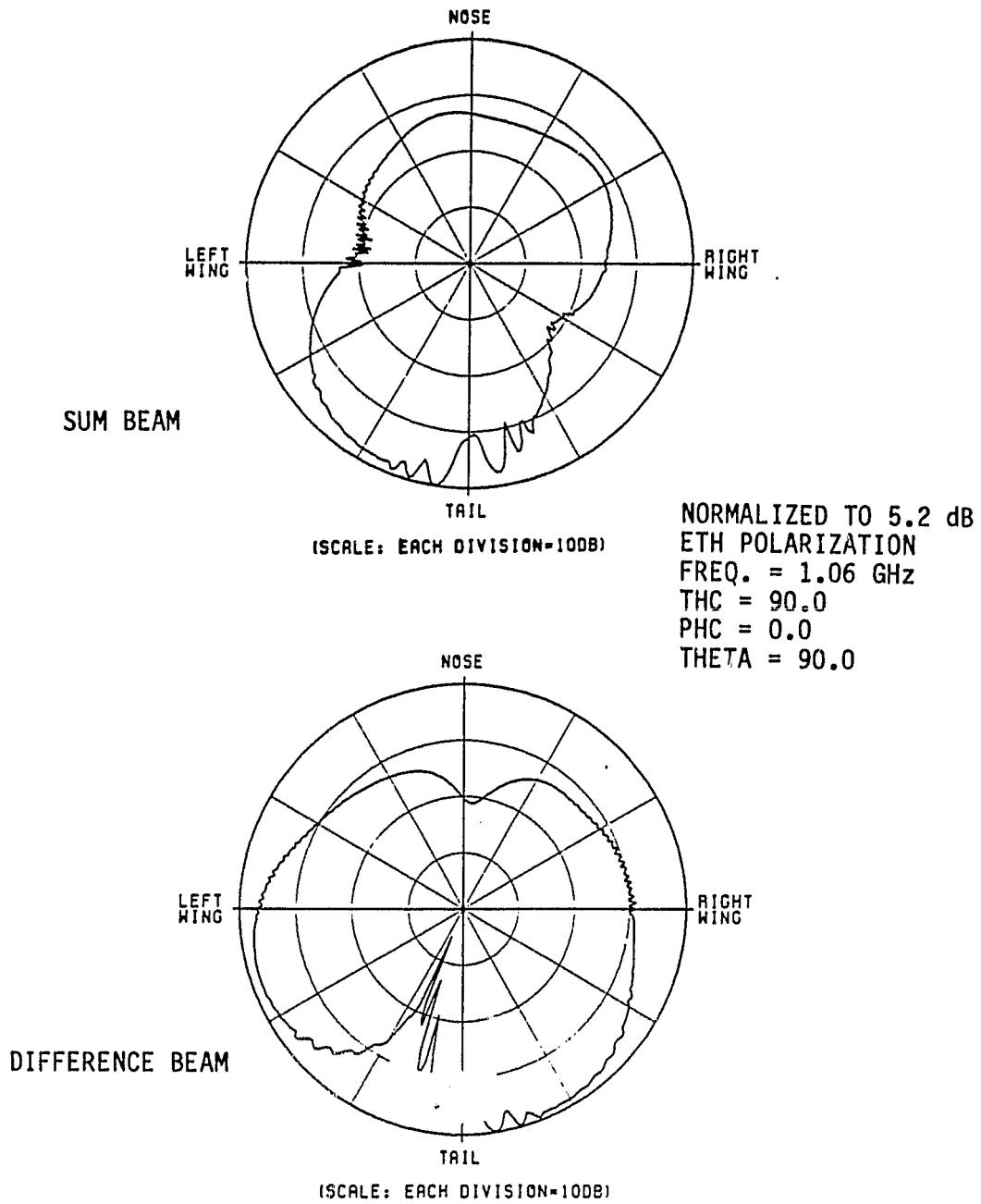

DIFFERENCE BEAM   NORMALIZED TO 9.1 dB

(SCALE: EACH DIVISION=10DB)
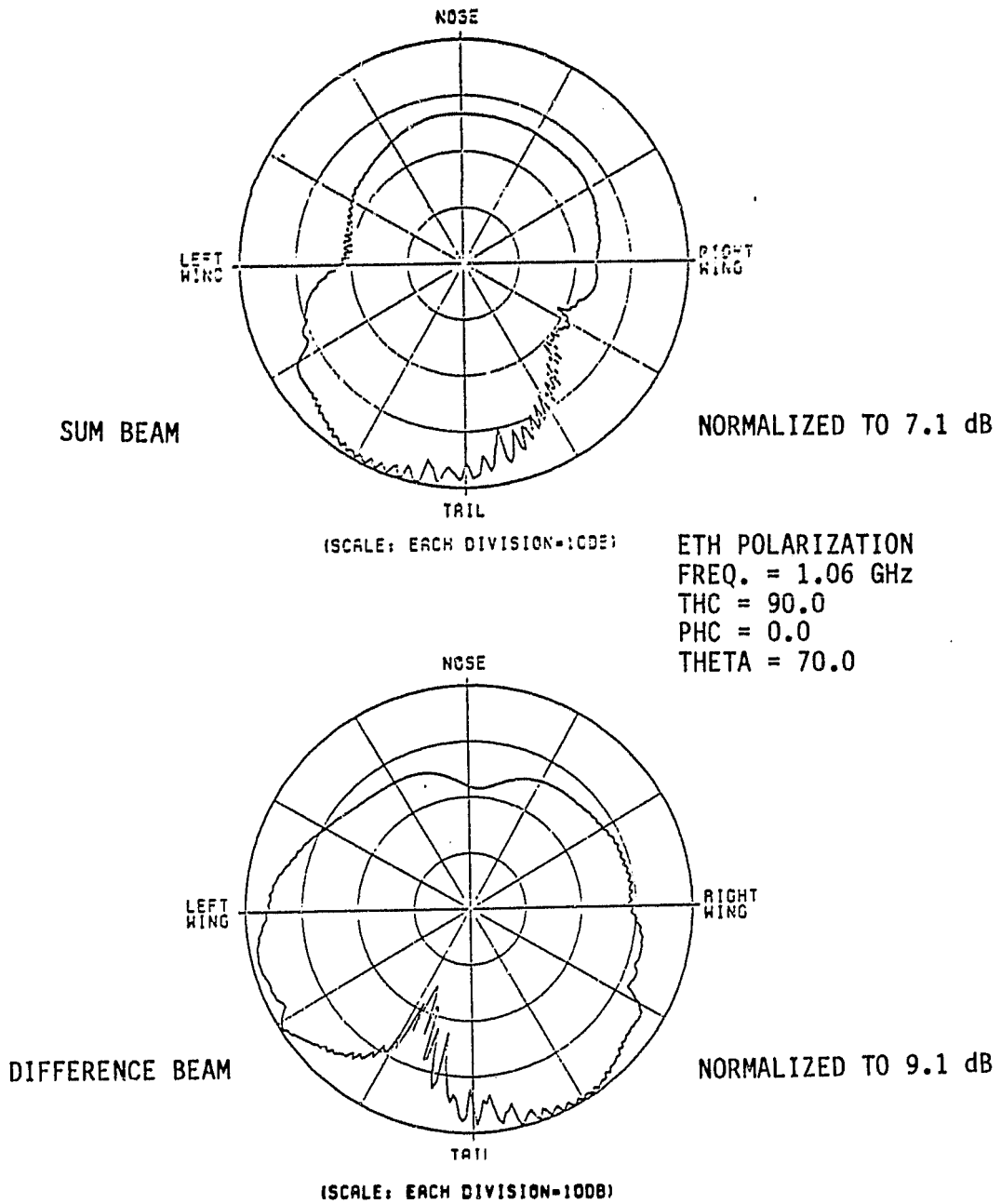
Figure 44. Superposition of the source (Figure 42), reflected (Figure 43) and diffracted fields.

63

AIRCRAFT MODEL WITH PLATES

CONICAL PATTERN ANGLE   70

BEAM POSITION   -157

DB

HNOSE
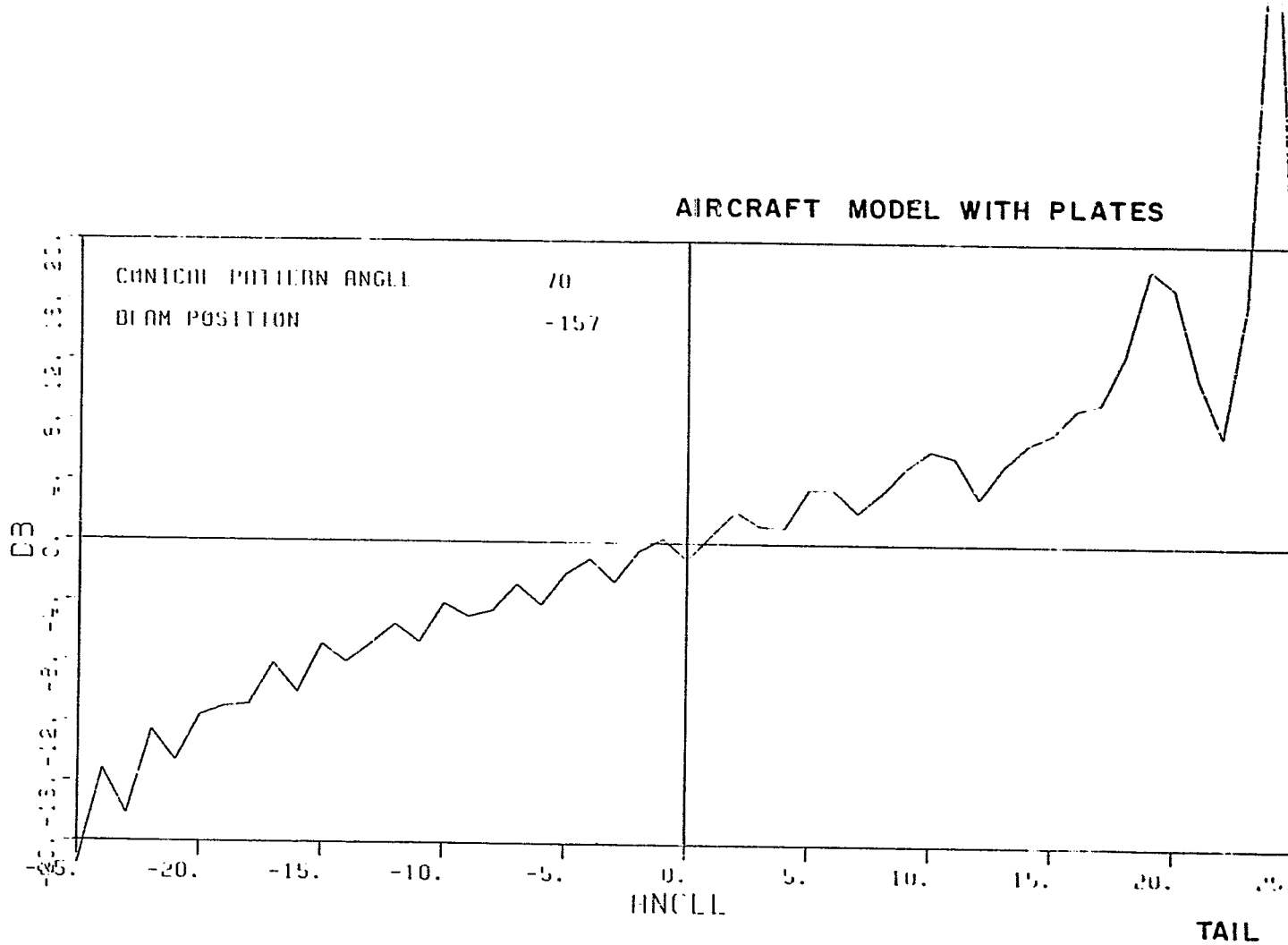
TAIL

Figure 45. Monopulse curve corresponding to Figure 44.

SUM BEAM

(SCALE: EACH DIVISION=10DB)

NORMALIZED TO 7.0 dB
ETH POLARIZATION
FREQ. = 1.06 GHz
THC = 90.0
PHC = 0.0
THETA = 90.0

DIFFERENCE BEAM

(SCALE: EACH DIVISION=10DB)
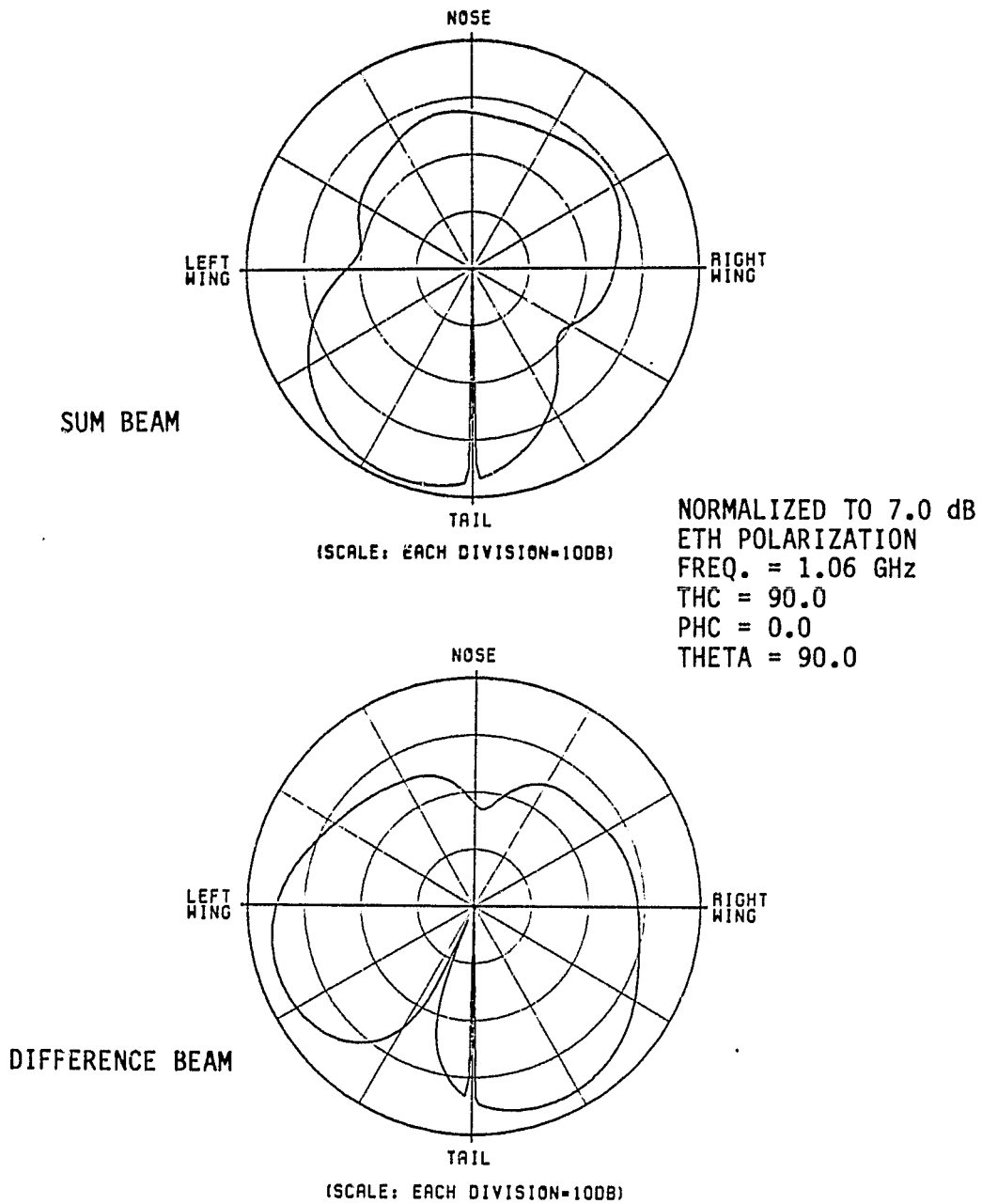
Figure 46. Radiation patterns of circular array where only the source field is included. The beams are pointed in the direction 23° to the left of the tail.
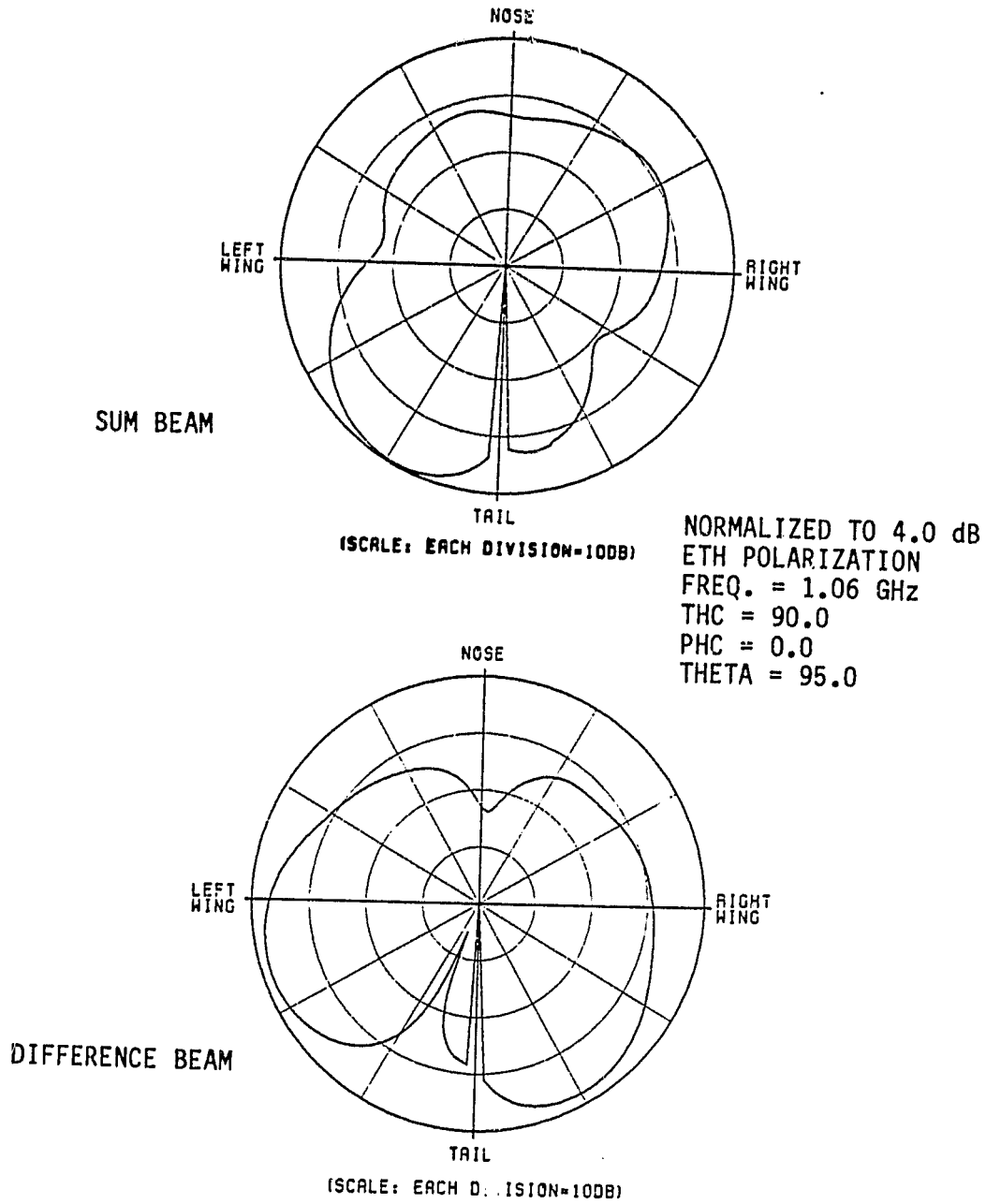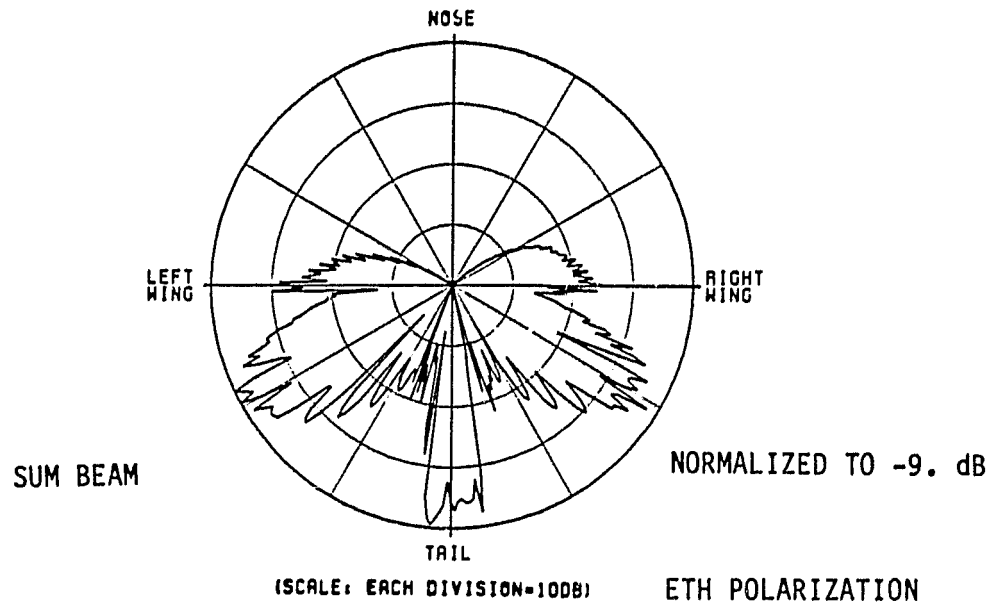
65

NOSE

LEFT WING

RIGHT WING

SUM BEAM

TAIL

(SCALE: EACH DIVISION=10DB)

NORMALIZED TO 5.2 dB
ETH POLARIZATION
FREQ. = 1.06 GHz
THC = 90.0
PHC = 0.0
THETA = 90.0

NOSE

LEFT WING

RIGHT WING

DIFFERENCE BEAM

TAIL

(SCALE: EACH DIVISION=10DB)

Figure 47.   Superposition of the source, reflected and diffracted
             fields.

66

CONICAL PATTERN ANGLE   90

BEAM POSITION   -157

AIRCRAFT MODEL WITH PLATES

67

ANGLE

TAIL
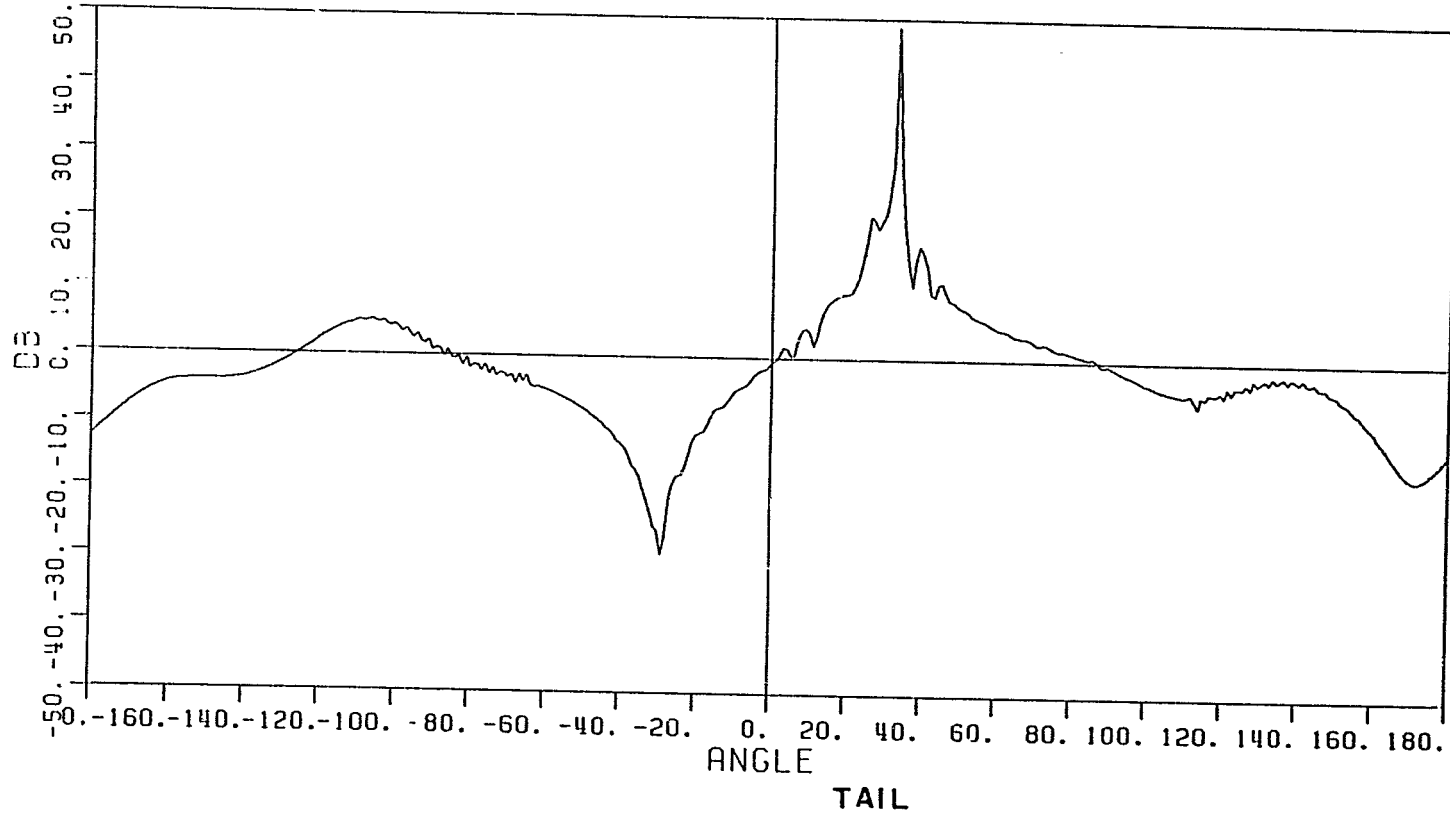
Figure 48.   Monopulse curve corresponding to Figure 47.

AIRCRAFT MODEL WITH PLATES

CONICAL PATTERN ANGLE   90

BEAM POSITION   -157

ANGLE
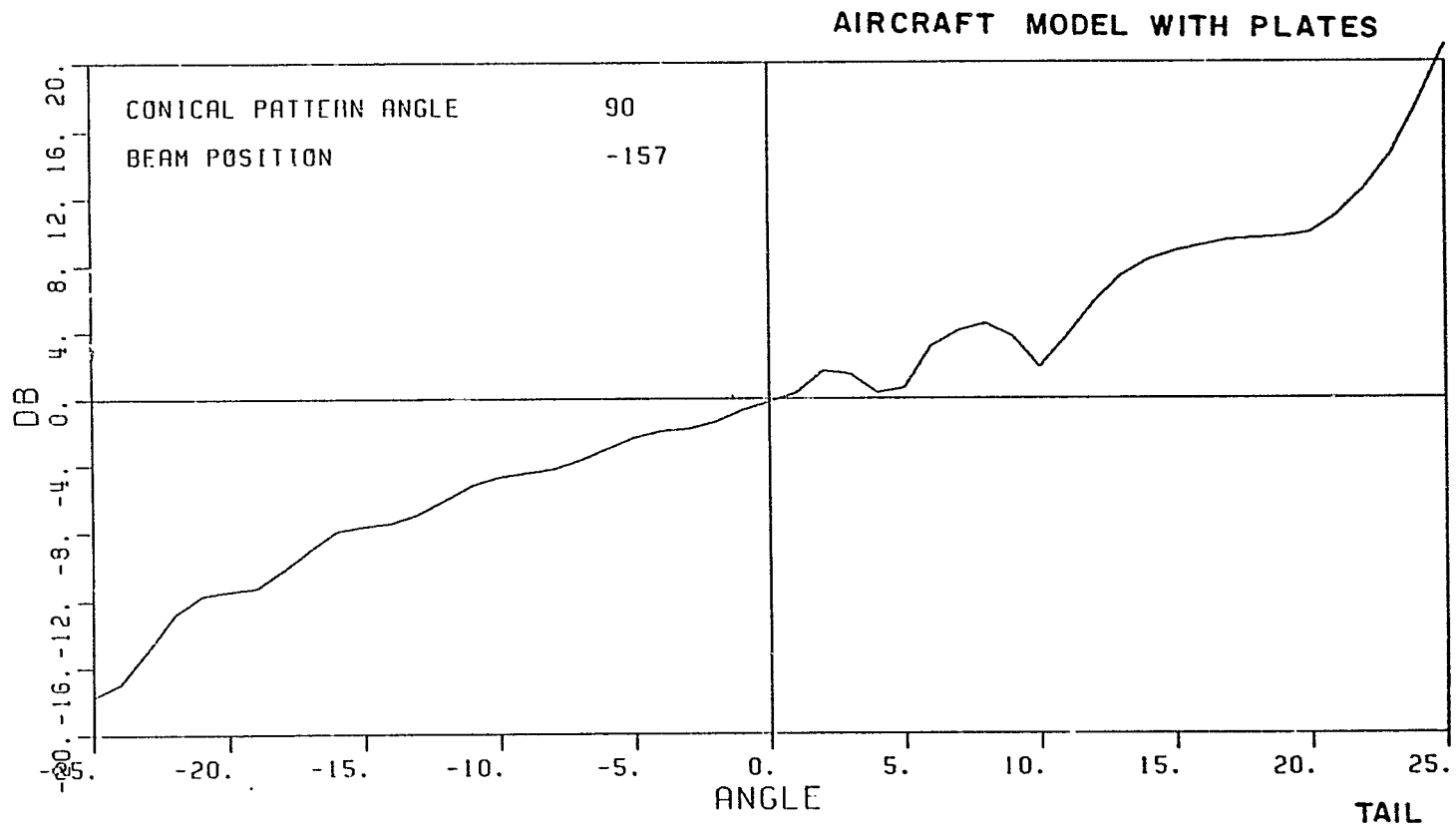
TAIL

Figure 49. Monopulse curve corresponding to Figure 47.

NOSE

LEFT
WING

RIGHT
WING

SUM BEAM

TAIL

(SCALE: EACH DIVISION=10DB)

NORMALIZED TO 4.0 dB
ETH POLARIZATION
FREQ. = 1.06 GHz
THC = 90.0
PHC = 0.0
THETA = 95.0

NOSE

LEFT
WING

RIGHT
WING

DIFFERENCE BEAM

TAIL

(SCALE: EACH DIVISION=10DB)

Figure 50. Radiation patterns of the circular array where only the
source field is included. The beams are pointed in the
direction 23° to the left of the tail.

NOSE

LEFT
WING

RIGHT
WING

SUM BEAM

NORMALIZED TO -9. dB

TAIL

(SCALE: EACH DIVISION=10DB)

ETH POLARIZATION
FREQ. = 1.06 GHz
THC = 90.0
PHC = 0.0
THETA = 95.0

NOSE

LEFT
WING

RIGHT
WING

DIFFERENCE BEAM

NORMALIZED TO -5. dB

TAIL

(SCALE: EACH DIVISION=10DB)
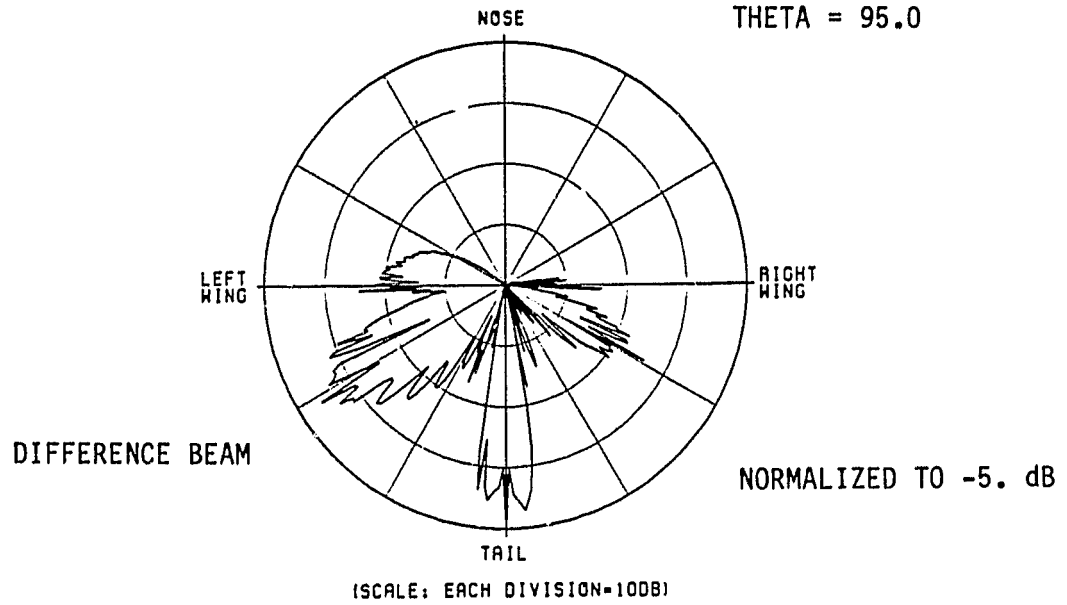
Figure 51. Diffracted fields only.

70

NOSE

SUM BEAM

NORMALIZED TO 3.7 dB

TAIL

(SCALE: EACH DIVISION=10DB)

ETH POLARIZATION
FREQ. = 1.06 GHz
THC = 90.0
PHC = 0.0
THETA = 95.0

NOSE

DIFFERENCE BEAM

NORMALIZED TO 3.5 dB

TAIL

(SCALE: EACH DIVISION=10DB)
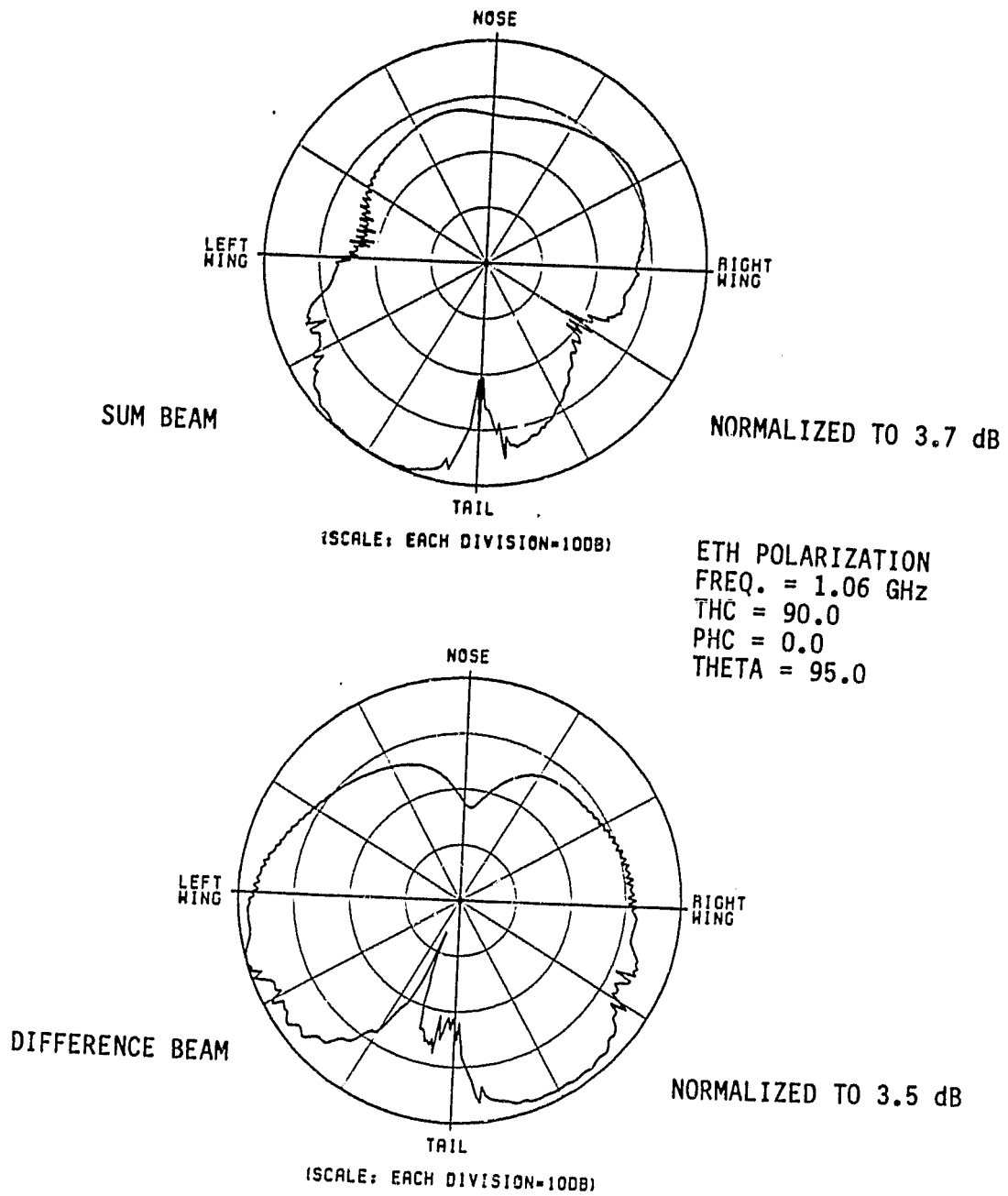
Figure 52.   Superposition of the source (Figure 50), reflected and diffracted (Figure 51) fields. Note that the beams are pointed in the direction 23° to the left of the tail.

71

CONICAL PATTERN ANGLE   95

BEAM POSITION   -157   **AIRCRAFT MODEL WITH PLATES**
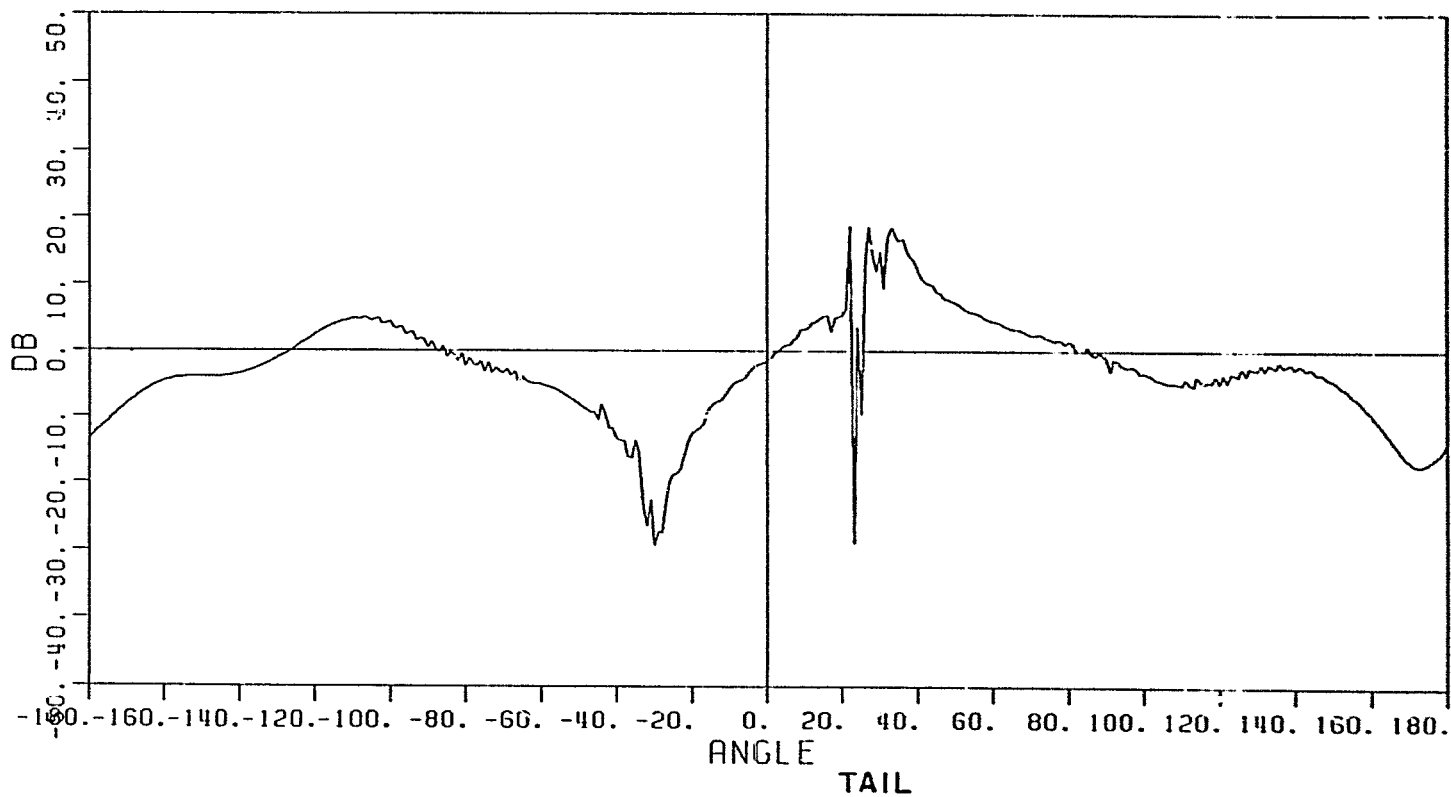
Figure 53. Monopulse curve corresponding to Figure 52.

AIRCRAFT MODEL WITH PLATES

CONICAL PATTERN ANGLE 95

BEAM POSITION -157

DB

ANGLE

TAIL
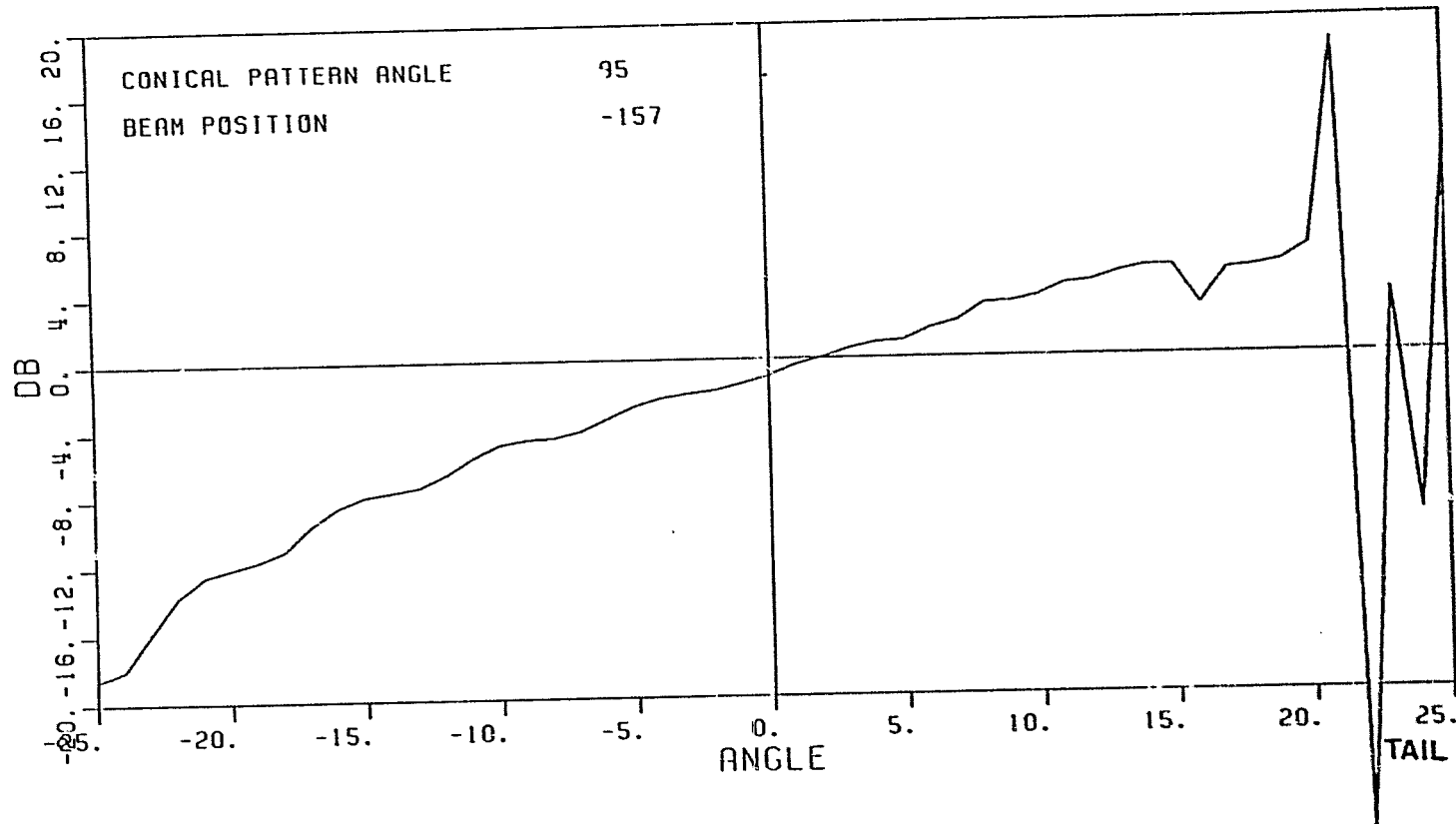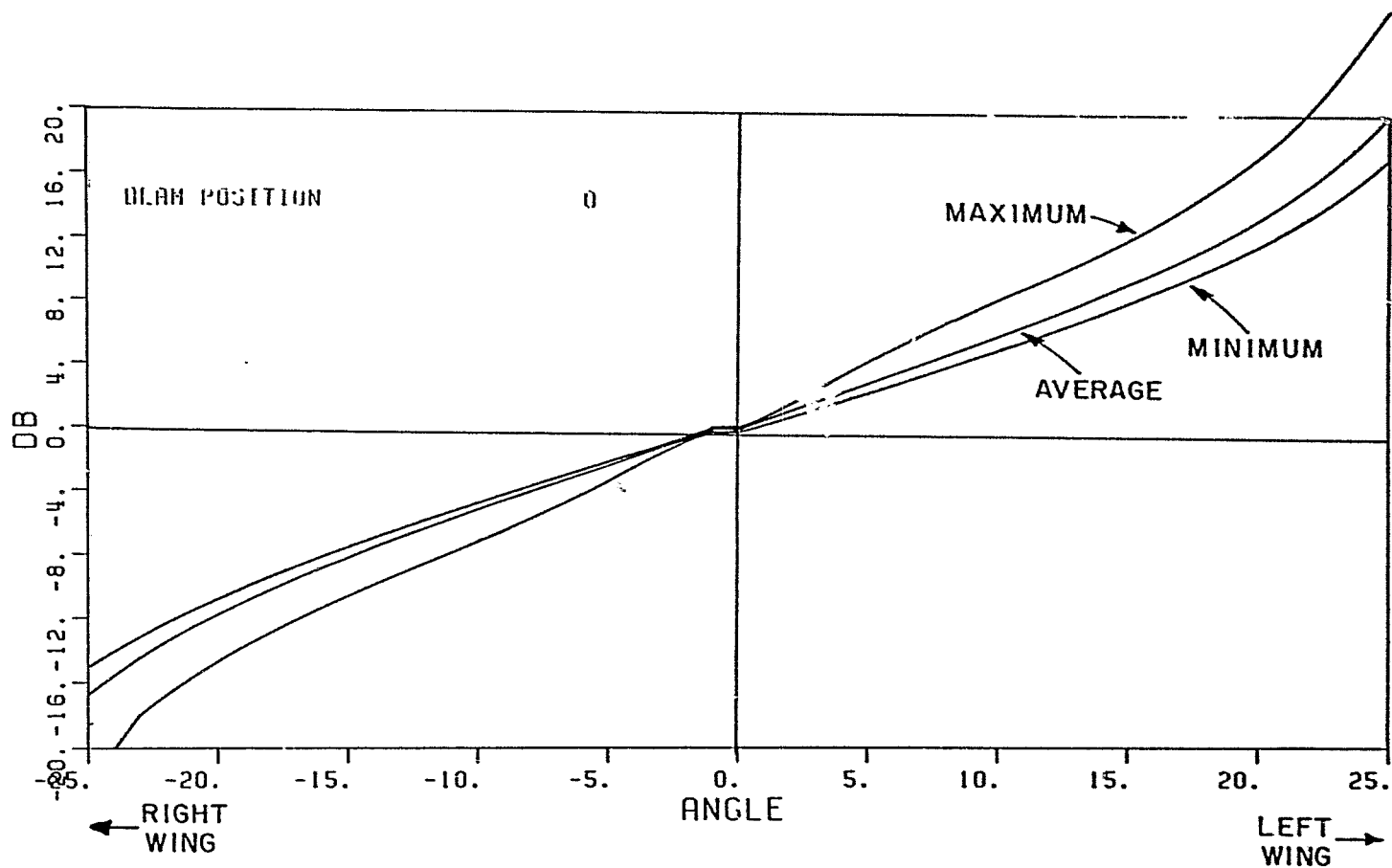
Figure 54. Monopulse curve corresponding to Figure 52.

Figure 55. Average, maximum and minimum values of the monopulse curves taken over the following values of THETA: 60, 65, 70, 75, 80, 85, 90, 95, and 100 degrees.
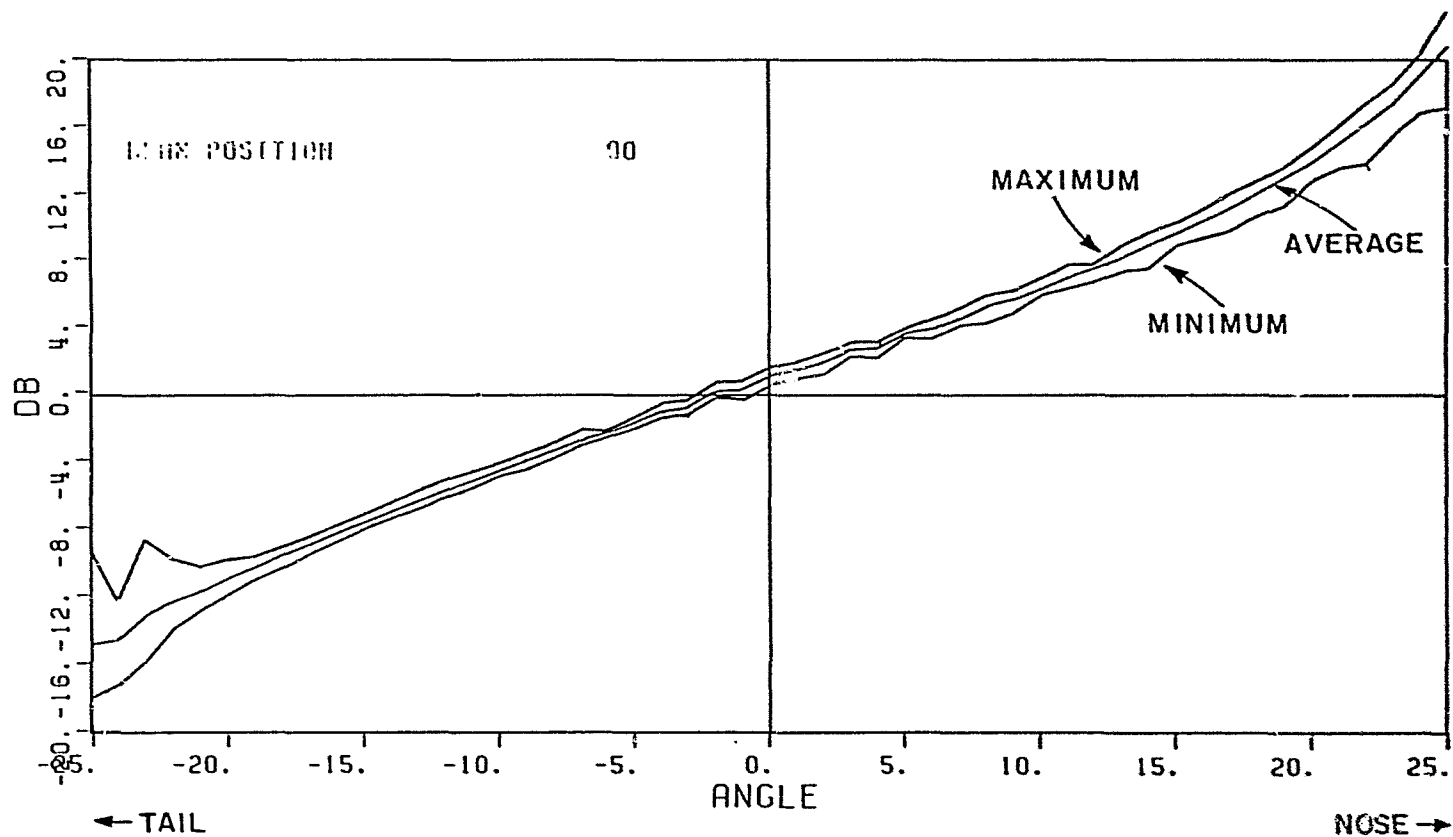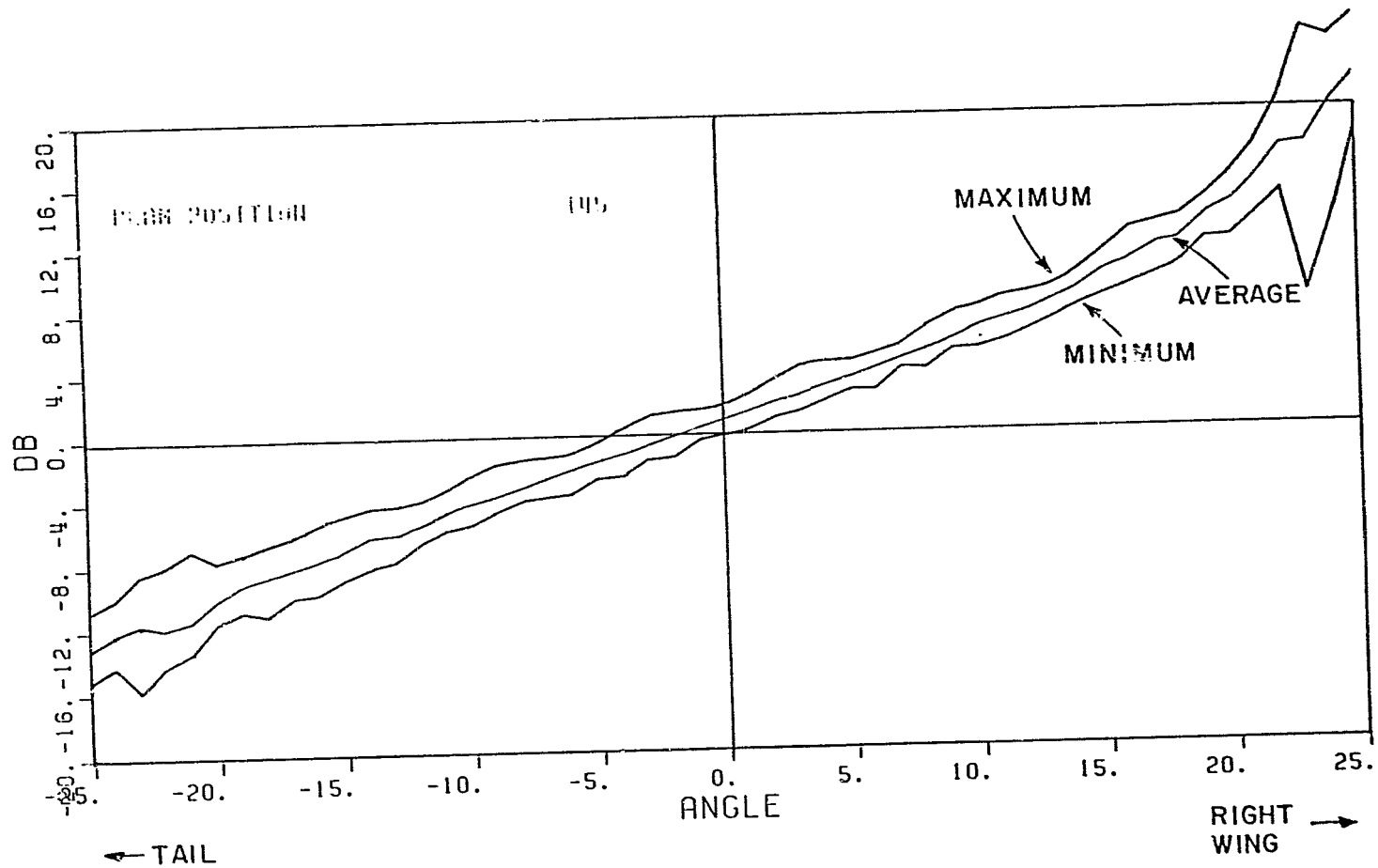
74

Figure 56. Average, maximum and minimum values of the monopulse curves taken over the following values of THETA: 60, 65, 70, 75, 80, 85, 90, 95, and 100 degrees.

Figure 57. Average, maximum and minimum values of the monopulse curves taken over the following values of THETA: 60, 65, 70, 75, 80, 85, 90, 95, and 100 degrees.
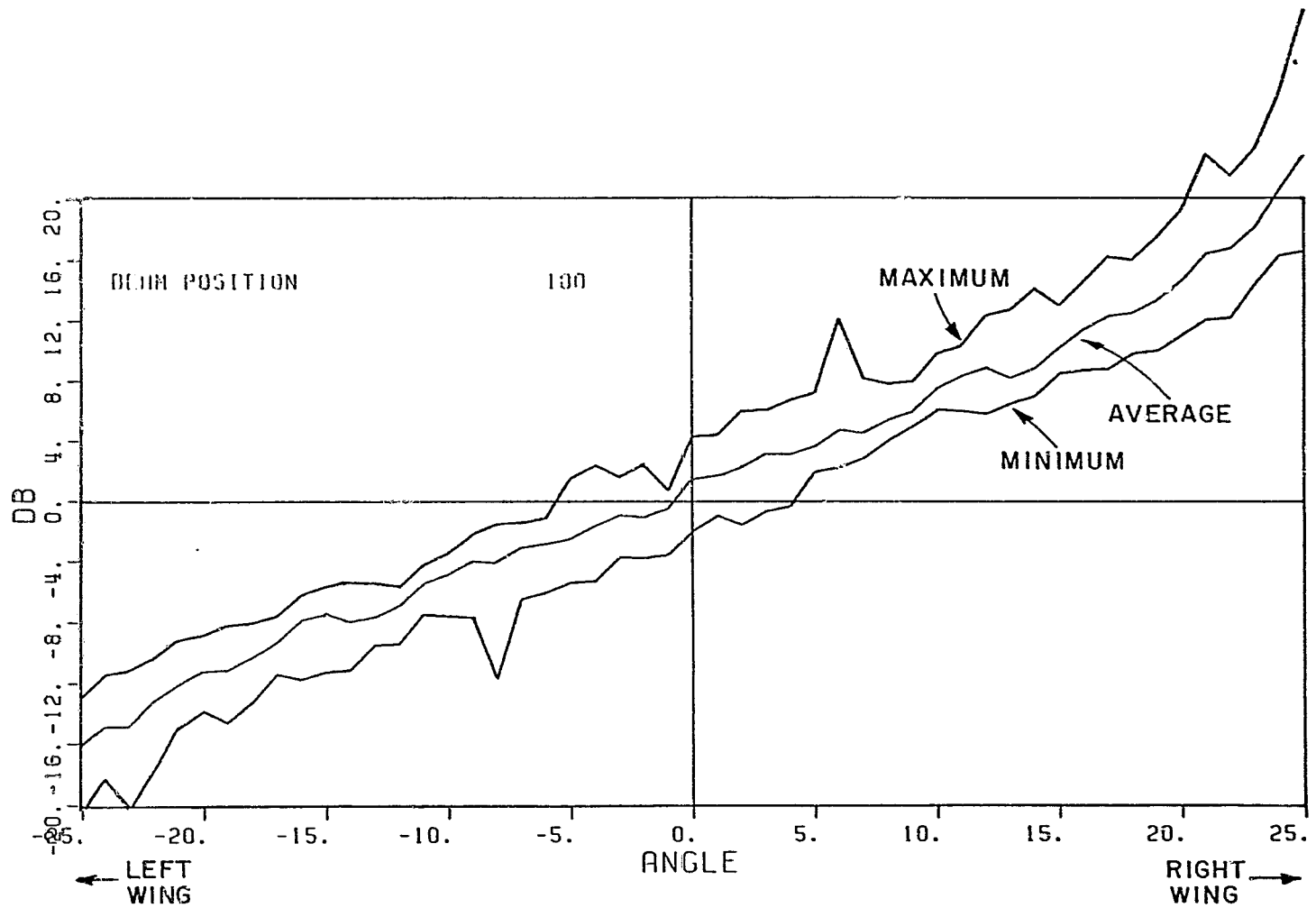
Figure 58. Average, maximum and minimum values of the monopulse curves taken over the following values of THETA: 60, 65, 70, 75, 80, 85, 90, 95, and 100 degrees.
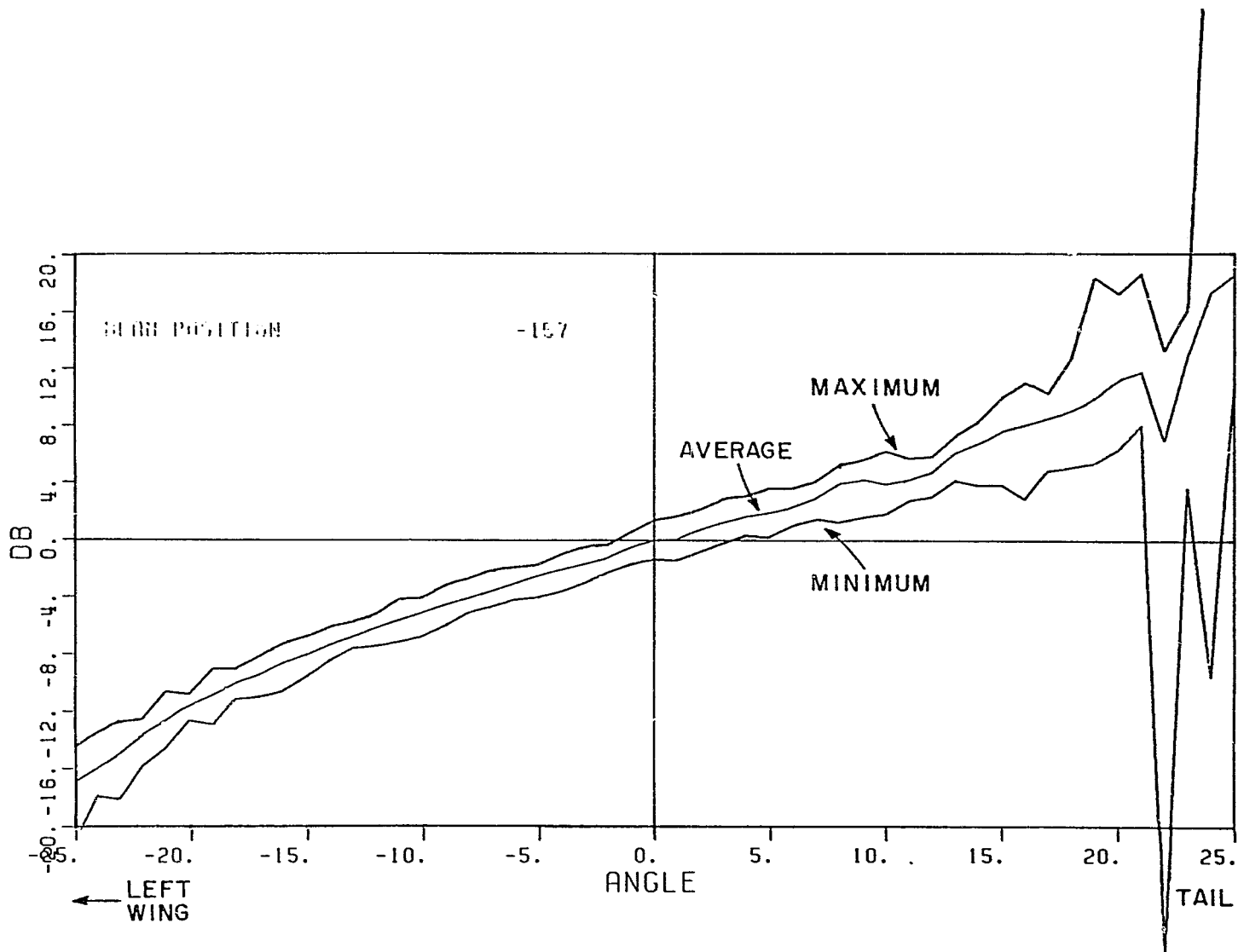
Figure 59. Average, maximum and minimum values of the monopulse curves
taken over the following values of THETA: 60, 65, 70, 75,
80, 85, 90, 95, and 100 degrees.

78